MOLECULAR BASIS FOR NUCLEOTIDE-DEPENDENT CONFORMATIONAL CHANGES OF THE LARGE GTPASE ATLASTIN

A Dissertation

Presented to the Faculty of the Graduate School

of Cornell University

In Partial Fulfillment of the Requirements for the Degree of

Doctor of Philosophy

by

Laura Jean Byrnes

August 2013

MOLECULAR BASIS FOR NUCLEOTIDE-DEPENDENT CONFORMATIONAL CHANGES OF THE LARGE GTPASE ATLASTIN

Laura Jean Byrnes, Ph. D.

Cornell University 2013

The membrane of the endoplasmic reticulum (ER) is the site of numerous complex activities essential to the survival of eukaryotic cells. In the membrane sheets of the rough ER (rER), integral membrane proteins are synthesized, folded, modified, and transported throughout the cell. In the smooth ER (sER) tubules, lipids are synthesized and processed with a variety of functionalities, and trafficked to specific membrane compartments. The sER is also the site of calcium storage and controlled release, an important function for several cell types including neurons and muscle.

The sER requires energy and the action of numerous proteins to maintain its highly curved, tubular shape and its reticular, interconnected structure. The recent discovery of a family of proteins called atlastins has helped answer some of the questions surrounding the tubular, reticular nature of the sER. Atlastins comprise a group of ER resident proteins that have been shown to facilitate the fusion of membrane tubules within this organelle. They are part of the dynamin superfamily of proteins, which use the energy stored in GTP to sculpt membranes throughout the cell. However, the exact molecular mechanism for how atlastin mediates membrane fusion remained mysterious. In this study, we have taken apart and analyzed atlastin-1, one of three isoforms of atlastin in humans. This isoform is found primarily in the central nervous system and is mutated in the neurodegenerative disorders Hereditary Spastic Paraplegia and Hereditary Sensory Neuropathy.

This study has resulted in a collection of three-dimensional, high-resolution structures of atlastin-1's catalytic core fragment, comprising its GTPase and middle domains bound to various forms of the guanine nucleotide. These structures revealed key information about the catalytic mechanism of atlastin-1, as well as interesting and important conformational changes that occur within the structure. Using these structures, as well as information from small-angle X-ray scattering (SAXS), size-exclusion chromatography coupled to multi-angle light scattering (SEC-MALS), Förster resonance energy transfer (FRET), and enzymatic activity assays, we have put together a general working model for atlastin membrane fusion and have gathered important information about its mechanism that may be used to target the protein for the treatment of disease.

BIOGRAPHICAL SKETCH

The author was born in Rochester, New York, USA on October 28, 1985 to parents Joseph and Carol Byrnes. She grew up in the town of Gates (a Rochester suburb) with two older sisters, Megan Byrnes Plank and Jennifer Byrnes, and a younger brother, Matthew Byrnes. In 2004 she graduated high school first in her class from Nazareth Academy in Rochester, New York and matriculated at Rensselaer Polytechnic Institute in Troy, New York. Here, she pursued research in several laboratories including a summer internship with Dr. Clyde Smith at the Stanford Linear Accelerator Center where she first learned crystallography. Working for Dr. Blanca Barquera at RPI, she wrote her senior research thesis entitled "Crystallization of *Vibrio cholerae* Transmembrane Protein, Sodium-Translocating NADH: Quinone Oxidoreductase, and the Role of nqrA". In 2008 she graduated *summa cum laude* from Rensselaer Polytechnic Institute with a Bachelor of Science in Biochemistry and Biophysics. She was subsequently admitted into Cornell University as a graduate student in the department of Molecular Biology and Genetics in the field of Biophysics. After two semesters of course work and research rotations, she joined Dr. Holger Sondermann's laboratory to complete her Doctoral training.

For everyone, ever...

Especially: Kylan and my family

and

FOR SCIENCE!

ACKNOWLEDGMENTS

I must first acknowledge my Doctoral advisor, Dr. Holger Sondermann; without his guidance, patience, and knowledge I would not be at this point in my career. I came to Cornell with no real idea as to what a good advisor should be, but now I know they must have many, if not all, of the attributes that Holger has exhibited while I've been his student. He has helped me to grow stronger as a person and to learn what it is to be an independent scientist, and I am extremely grateful for all that he has done for me throughout these years.

In my time leading up to this moment, it is astounding to me the number of people who have touched my life and have been instrumental in getting me here. First and foremost is my family. My parents, Joe and Carol Byrnes, have always been a guiding light in my journey towards the publishing of this dissertation. Their undying love and encouragement has given me the strength to pursue science and higher learning, one of the toughest paths I could have chosen for my life. They have nurtured my love for the natural world from the very beginning, and have made me into the inquisitive, motivated person that I am today. My siblings (Megan, Jenny, and Matt Byrnes) have always been a huge influence in my life, and have also encouraged my pursuit of science. They have taught me patience, fairness, and kindness. They have been great friends to me when I needed them, have provided distraction when I just wanted a break, and gave a listening ear for all of my endless complaints, without asking for anything in return. Their visits to Ithaca have always been a welcome diversion from the stress of graduate school, and I've loved every minute of our times together. Last, I'd like to mention Liz McKinley who has always been like family to me has been there through many important events in my life, including the hiking of the 46 High Peaks in NY that we accomplished with my mom and Carolyn Roorda. We've accomplished amazing things together, and this is part of the reason I never

gave up on my educational journey! Thank you to all of my family for never giving up on me, always believing in me, and for loving me despite all of my faults.

In addition to my family, I could not have done this without my soon-to-be husband, Kylan Szeto who came to Cornell with me and has traveled on the same difficult road to his Ph.D. in Applied and Engineering Physics. When we met in undergraduate college at Rensselaer Polytechnic Institute, it was immediately clear to me that he would be a great friend who was a very attentive listener, full of good advice, and helpful in all things academic. Soon I realized he would also be the love of my life, as well as an endlessly encouraging and supportive partner. It is partly because of him that I ended up at Cornell, with our good luck in both being accepted here for graduate school and our desire to stay together during a time in our lives that we both knew would be difficult. There's no better choice I could have made for my career and for my life. He has been my shoulder to cry on when I felt overwhelmed, my alarm clock in the mornings I can't get out of bed, my walking partner, my bird watching assistant, and my source of infinite encouragement and love. Besides all of his support for me personally, he has also contributed concretely to my studies here and we've become quite an effective scientific team. I hope this continues well into the future, whatever careers we find ourselves in. I am forever grateful for his patience, love, kindness, understanding, and support. I will love your bam forever.

Next, I would like to thank the members of the Sondermann lab group for all of their support and help during my time there. I would especially like to thank Dr. Qi Wang, a fellow biophysics graduate student who trained me when I first came to Holger's lab. He taught me a lot of practical skills that I am very grateful for, but was also a great friend and advisor to me when I really wasn't sure about what I was doing. I admire him for his intellect, and am extremely appreciative of all that he taught me about crystallography and many other skills necessary for my success in the lab.

Along with Qi, I am thankful for Dr. Shih Lin (Lynda) Goh, Dr. Petya Krasteva, Dr. Marcos Navarro (especially for giving me his lucky desk!), Dr. Debashree Chatterjee, Dr. Krista Giglio, Dr. Richard Cooley, and (future Dr.) John O'Donnell for their friendship and guidance throughout my Ph. D. Additionally, I had the privilege of working with several undergraduate students during my studies, including Yekaterina Rokhlenko, Gary Peng, Nicole Benvin, Micah Lerner, and Cassady Rupert. All of these students have been a joy to work with, and I consider myself very lucky to have been a part of their scientific training. In turn, they have also taught me a lot about what it means to be a teacher and a mentor and have contributed their hard work and dedication to parts of this thesis and other projects. In particular, Nicole was an author on my second atlastin paper (covered in Chapter 3) by helping to get atlastin crystallized with GTP analogs. Micah also was a part of a crystallization effort, and contributed to an ongoing project using computer simulations to find small molecule that could bind to and affect atlastin. Cassady contributed a large amount of time and effort to crystallizing new atlastin states, and has contributed one of her successful structures to Chapter 4. To all of the students I have helped advise, thank you for your efforts and I wish you all the best in your future careers.

I have met many great people during my life, several of whom I am proud to call good friends. While many friends have come and gone, there are a few that have stayed around and for whom I am extremely thankful to have in my life. First, I want to thank my best friend and maid of honor in my upcoming wedding, Katie Zynda. Where would I be today if you hadn't invited me to join you and your friends on that fateful day during lunch? I dare not speculate, but I think my life would be very different than it is now. You are and always have been a true and loyal friend to me, and I am eternally grateful that you chose to share your kind heart with the likes of me, the mostly awkward and ever-uncertain girl who found herself without a friend in

7th grade homeroom. You showed me the confidence I never thought I had. I've shared with you many of my most cherished memories, silliest jokes, and my deepest secrets. Olive you so very much; thank you for always being there.

In addition to old friends, I've made some great new friends while here at Cornell. In particular, I'd like to mention my dear friends Dr. Shih Lin (Lynda) Goh and Dr. David Lee. Lynda and I started out as just lab mates, but soon we figured out we had a lot in common outside of lab too and have been acting silly together ever since! She and her husband David have not only been a wonderful source of endless amusement for Kylan and I, but also have been dependable and loyal friends when we've needed them. I'd also like to mention some friends we've made more recently at Cornell, David Ackerman and Huimin Chen. Even though we haven't known them for as long, they've been wonderful to be around and have taken part in many recent adventures with Kylan, Lynda, David, and I. They've also helped me in this process of thesis writing and defending and I'm grateful for their encouragement and advice.

Some other important people that have helped me on my way here include those who were a part of my research training in undergraduate school. The very first lab I ever worked in was with Dr. Russell Ferland at RPI. I have never forgotten the skills I learned there, and am grateful to him for that initial training. I also did an internship at the Stanford Linear Accelerator Center (SLAC) with Dr. Clyde Smith doing crystallography. This internship forever changed my research interests, and it is where I fell in love with crystallography. My last undergraduate lab position was with Dr. Blanca Barquera, where I first learned how to grow and purify recombinant proteins.

I also want to thank all of the staff at CHESS for their time and expertise while I used the various beamlines for my research. In particular, I'd like to thank Dr. Richard Gillilan, Dr. Sören Neilson, Kathy Dedrick, Dr. Chae Un Kim, Dr. Irina

Kriksunov, Dr. Bill Miller, and Dr. David Schuller. Thank you also to everyone at CHESS who work tirelessly to keep everything up and running for its users.

Several other Professors and people from other labs have also been very generous with their time and equipment, including Dr. Ruth Collins' lab, Dr. Harold Craighead's lab, and the protein core facility run by Dr. Cythia Kinsland. Additionally, my committee members Dr. Bill Brown and Dr. Joe Fetcho have always been amazing mentors and sources of encouragement. Thank you for all of the time you've given to me for committee meetings, seminars, and exams and for always believing in me!

Lastly, there is quite a number of staff and faculty that also played a part in my success by making sure all the administrative issues are organized and worked out, and I want to thank them for giving their time, knowledge, and encouragement. Thank you to Debra Crane, Valerie Moore, Vicki Schaff, Cindy Westmiller, Diane Colf, and Greg Mitchell for making graduate school run so smoothly!

This work was funded by several sources for which I am very thankful to have had access to, including the Presidential Life Science Fellowship through Cornell University, NIH Awards T32 GM008267 and 1F31 NS077650, and the PEW Scholar Award to Holger Sondermann.

TABLE OF CONTENTS

LIST OF FIGURES

LIST OF TABLES

LIST OF ABBREVIATIONS

EM	Electron microscopy
ER	Endoplasmic Reticulum
FRET	Förster resonance energy transfer
GAP	GTPase activating protein
GDP	Guanidine di-phosphate
GED	GTPase effector domain
GEF	Guanine-nucleotide exchange factor
GTP	Guanidine tri-phosphate
HR	Heptad repeat
HSN	Hereditary Sensory Neuropathy
HSP	Hereditary Spastic Paraplegia
MIS	Mitochondrial import sequence
PH	Pleckstrin homology
PM	Plasma membrane
PRD	Proline-rich domain
rER	Rough endoplasmic reticulum
SAXS	Small angle X-ray scattering
SEC-MALS	Size-exclusion chromatography coupled to multi-angle light scattering
sER	Smooth endoplasmic reticulum
TEM	Transmission electron microscopy

CHAPTER 1

INTRODUCTION

MEMBRANE FUNCTION AND DYNAMICS

In the world of the cell, the membrane is the supreme mediator of organization. It provides structure, a means of separation, and a platform for reactions that would otherwise be impossible in the environment of the cytoplasm. In some ways even more so than DNA, a lipid membrane is a universal component in all forms of life, including viruses.

In eukaryotes the membrane is an essential tool in a variety of tasks that allow for the cell's intense complexity. Billions of years ago the simple prokaryotic cell evolved from a single plasma membrane enclosing the entire cell to an organism with several membrane-bound organelles within it (1). Importantly, the nucleus was cordoned off from the cytoplasm and an organelle called the mitochondria appeared that revolutionized the way cells produce energy. With the mitochondria, cells could use aerobic respiration to metabolize the same amount of their carbon-based energy sources (sugar) to make almost twenty-times as much energy for cellular activities as they could before using anaerobic respiration (1). This newfound energy would allow eukaryotes to develop more complex ways to take advantage of their environment and compete with other organisms. Eventually this would lead to the emergence of multi-cellular life, including the metazoans to which human beings belong.

Modern eukaryotes not only contain a nuclear membrane and mitochondria, but have also developed a highly coordinated and intricate system for transportation, modification, and metabolism of nutrients, proteins, lipids, ions, and other signals the cell uses to survive and interact with the environment. This system includes a collection of membranous compartments that have specific jobs, but are all

interrelated in their activities. These include the endoplasmic reticulum (ER), the Golgi complex, and the endosomal membrane system. These organelles are involved in the synthesis, modification, targeting, and recycling of membrane proteins throughout the cell. Additionally, they orchestrate the production and organized shuffling of lipids.

Clearly, cellular membranes cannot be static, unchanging structures. Many years of research has revealed that membranes are anything but simple. The lipids that make up membranes are structurally and functionally diverse, with phosopholipids constituting the main components of biological membranes (Figure 1.1.). These types

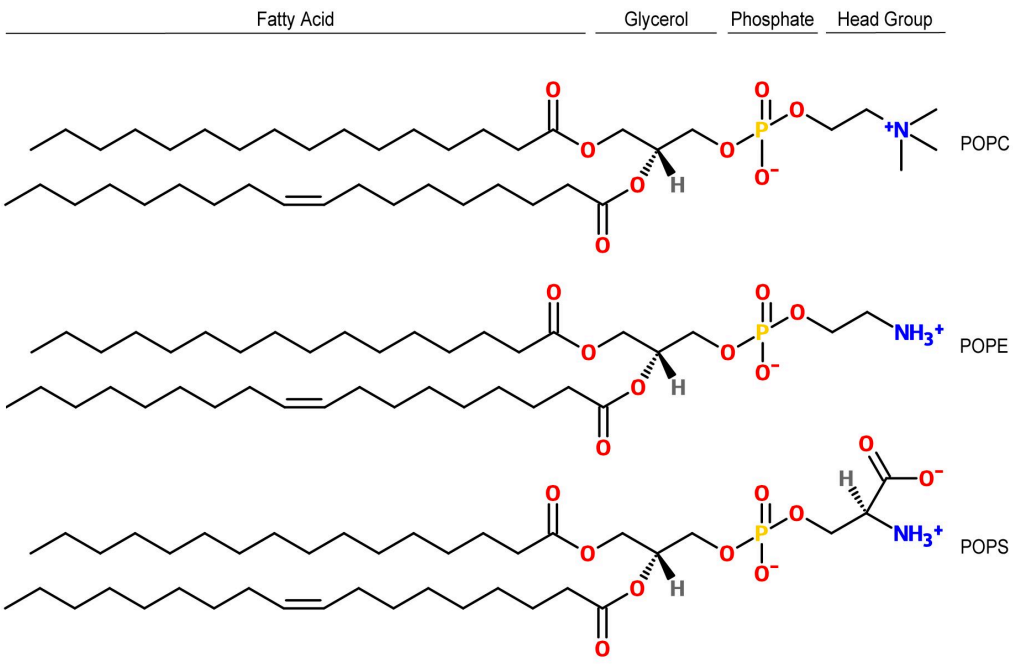

Figure 1.1. Chemical structure of phospholipids. Structures of three common phospholipids found in mammalian cell membranes: POPC (top), POPE (middle), and POPS (bottom). All phospholipids are made up of a hydrophobic, fatty acid tail that often contains unsaturated carbon-carbon double bonds. A glycerol moiety (in most cases) links these fatty acid tails to a phosphate group, which is followed by a simple organic molecule (called the headgroup). Variations in the identity of the headgroup and degree of saturation in the fatty acid tails determine the specific properties of phospholipids in the membrane.

of lipid are comprised primarily of three parts: a glycerol core, hydrophobic fatty-acid tails, and a phosphoester linked hydrophilic head group that can take on a variety of shapes, sizes, and charge states. Each membrane subcompartment can be comprised of numerous lipid types, differing both in their hydrophobic tails and their head groups. Some of these lipids are present for signaling purposes (i.e. Phosphatidylinositol phosphates [PIPs]), some serve to impart a certain structure to a membrane (curvature), while others are present to form platforms on which biological reactions and interactions can occur (rafts). Each organelle compartment is comprised of a specific mixture of lipids that both defines it and aids it in its function.

Of particular relevance to the topic of this dissertation is the smooth ER (sER). The sER is the site of lipid synthesis, where they are assembled from cytosolic precursors, packaged into vesicles, and finally trafficked to their target organelle via endosomal transport or direct contact sites (2, 3). The tubular, reticular shape of the sER serves to maintain its luminal continuity and increase the surface area of this organelle in order for it to do the job of lipid synthesis, calcium buffering, and metabolism of various molecules in locations throughout the cell. This tubular structure requires energy to stabilize its highly curved structure. This can often be accomplished simply by distributing specific proteins and lipids unevenly across the two leaflets of the membrane. In particular, ER resident proteins called Receptor Accessory Proteins (REEPs) and reticulons (4) can insert into the outer leaflet of the bilayer, effectively increasing the surface area of that leaflet and causing the membrane to take on an inherently curved structure to accommodate the mismatched surface area of the two leaflets, a phenomenon called hydrophobic insertion (5, 6) (Figure 1.2.). Lipids can also accomplish this task if the headgroups of the lipids in one leaflet of the bilayer take up more volume than those on the opposite leaflet. In the sER, both of these strategies are used in order to create long tubules. The branched (or

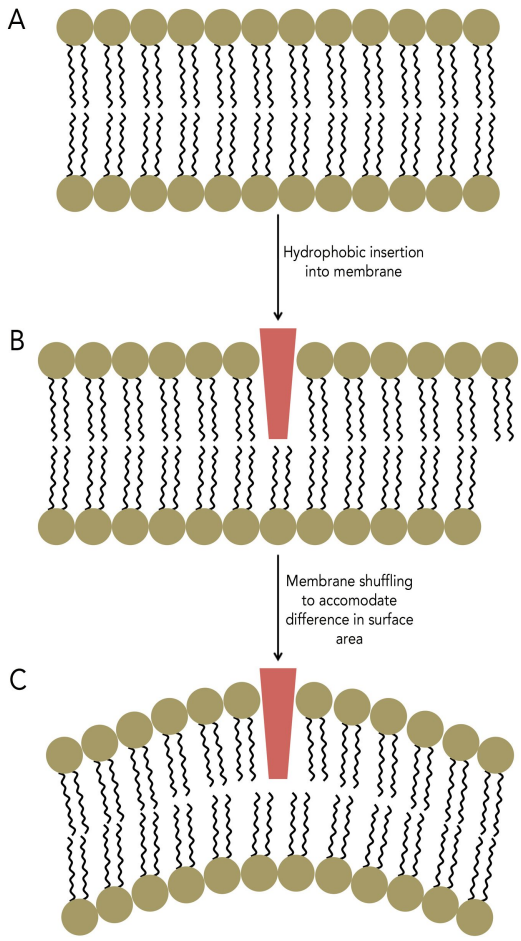

Figure 1.2. Hydrophobic insertion. (A) Within the lipid membrane, the hydrophobic tails (black, curvy lines) of lipids are buried within the bilayer and protected from water exposure by hydrophilic headgroups (brown circles). (B) When a protein inserts a hydrophobic region into one leaflet of the membrane, the surface area of that leaflet is effectively increased. (C) This disparity in surface area can be accommodated on the opposite leaflet by curving the membrane.

reticular) nature of the sER is achieved through the fusion of these tubules (3, 7-10). However, membrane fusion is a non-trivial process that also requires energy and importantly, specificity in order to control the shape of the resulting structure. In most fusion events throughout the secretory pathway, proteins called SNAREs (Soluble Attachment N-ethyl-maleimide-sensitive fusion Protein REceptor) mediate this process through the use of metastable protein-folding intermediates that store the potential energy used to power fusion (11-14). Within this family of proteins, there are

both target (t) and vesicle (v) SNAREs that are paired specifically to one another in order to fuse only vesicles containing the correct v-SNARE with a target membrane containing the corresponding t-SNARE. Although the sER contains SNAREs for exporting lipids and proteins, it was recently discovered that homotypic fusion of sER tubules into a reticular network is accomplished through a new family of fusogenic proteins called atlastins (8, 10, 15-17). Atlastins are integral membrane proteins belonging to the dynamin superfamily of proteins that use chemical energy to sculpt membranes. In the case of atlastins, the chemical energy stored in GTP is used to bring together and ultimately fuse opposing membranes in the sER. Atlastin's fusion activity is necessary for both ER establishment and maintenance, with knockdowns of atlastin in *Drosophila melanogaster* exhibiting fragmentation of the ER (10).

The ability of a membrane to be dynamic, to achieve fusion and fission, and to take on specific morphologies is not a unique requirement of the sER. These activities go on throughout the cell in every membrane, involving a vast number of proteins to control these processes. The dynamin-superfamily of large guanosine triphosphatases (GTPases, to which atlastin belongs), is a major player in these processes, especially membrane fusion and fission, and will be discussed further below.

DYNAMIN RELATED PROTEINS

Proteins of the dynamin superfamily have ancestors dating all the way back to prokaryotes (18), highlighting their importance in mediating membrane dynamics in all types of cells. A major subset of this diverse group of proteins is primarily involved in facilitating membrane fission and fusion. These proteins take part in numerous essential cellular processes, including pathogen resistance, endocytosis, organelle fission and fusion, and cytokinesis (19, 20). The genetic locus of the family's namesake, dynamin, was first discovered as a temperature-sensitive mutation in

Drosophila melanogaster that caused paralysis (21). Even before this, the protein dynamin was found in extracts of cow brain, associated with microtubules and reported as a mechanochemical enzyme (22). Presently, dynamin is the most intensively studied member of the superfamily, with numerous high-resolution structures that have helped shape our understanding of this important protein (23-27).

Dynamin and it's related proteins are composed of a large GTPase domain as well as one or several domains that aid in their mechanochemical functions. The GTPase domains of proteins in the dynamin family are related to the well-known Ras-like GTPases, but with several distinct differences. First, the GTPase domain of dynamin-like proteins is larger in size compared to Ras-like GTPases (~300 amino acids compared to ~180). Second, instead of relying on GTPase activating proteins (GAPs) many dynamin-like proteins have been shown to use homo-oligomerization to activate and accelerate their GTPase activity (28). In this regard, dimerization is believed to stabilize the conformation of the otherwise flexible switch regions and hence the catalytically active state. In addition, they do not need Guanine-nucleotide Exchange Factors (GEFs) in order to initially bind GTP in exchange for GDP, because they have a much lower affinity for nucleotide in general compared to Ras-like GTPases. Dynamin-like GTPases are also fundamentally different from their Ras-like cousins in that their main function is not for signaling using GTP and GDP as an on-off switch, but instead they use it to do mechanical work in the cell. Because of this, all dynamin-like proteins contain other functionally relevant domains in addition to their GTPase domain. In particular, they all include a middle or helical domain that is involved in oligomerization and usually assists in the mechanics of the protein's function. They are also all targeted to one or more membranes by an integrated membrane interaction domain or via post-translational modification with the addition of a lipid group such as an isoprenoid moiety (29). Some members also contain other

types of targeting domains, such as PRD (Proline-rich domain) to mediate protein-protein interactions (Figure 1.3.).

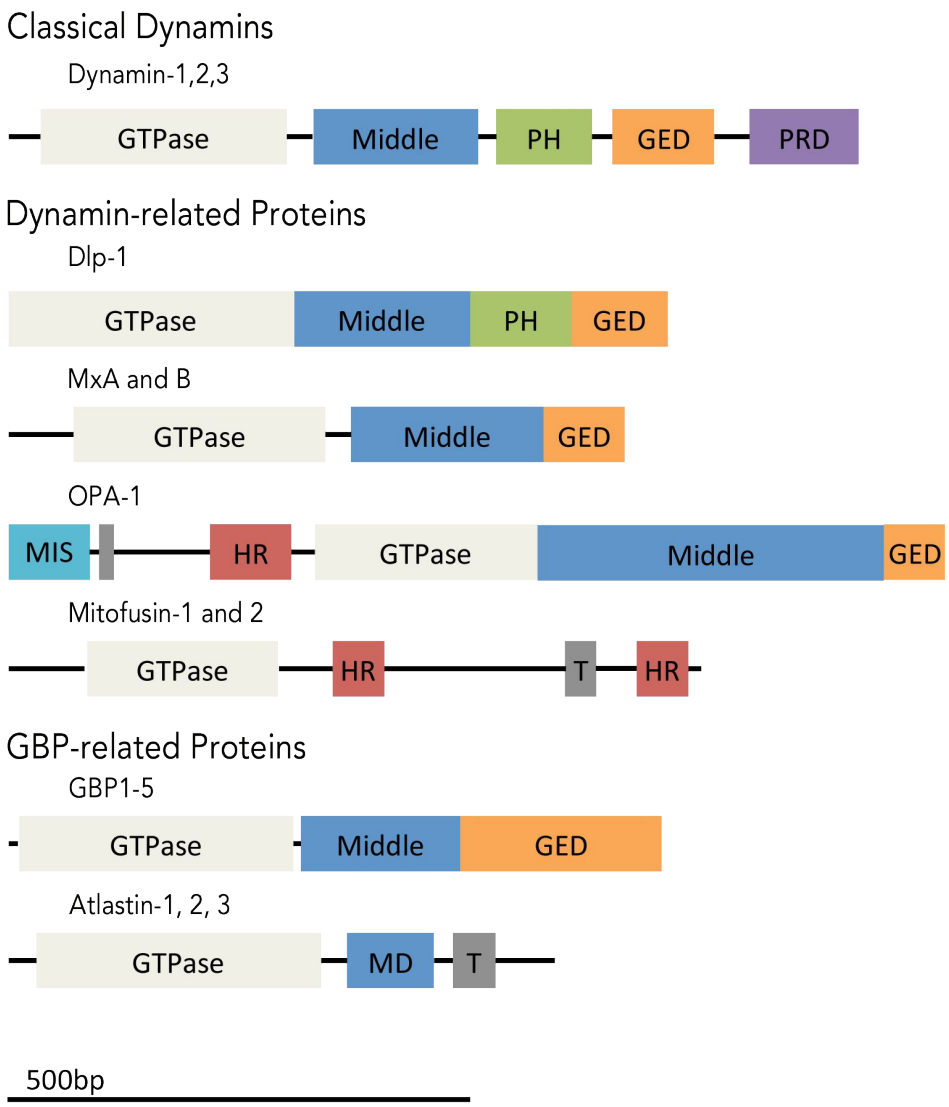

Figure 1.3. Dynamin superfamily proteins. Domain architecture of the human dynamin superfamily members, broken down into subfamilies according to Praefcke and McMahon (19). The Classical Dynamins include the three human isoforms, each containing the five domains shown above. The Dynamin-related Protein subfamily includes Dlp-1, MxA/B, OPA-1, and Mitofusin-1 and 2. The last subfamily, and furthest related by sequence, are the GBP-related Proteins, which include the five GBP isoforms and three atlastin isoforms. All domains and interdomain regions are drawn to scale and are color coded as follows: GTPase domains (off white), Middle domain (Blue), GED [GTPase effector domain] (Orange), PH [Pleckstrin homology] (Green), PRD [Proline-rich domain] (Purple), Transmembrane domains (Grey), HR [Heptad repeat] domains (Red), and MIS [Mitochondrial import sequence] (Teal).

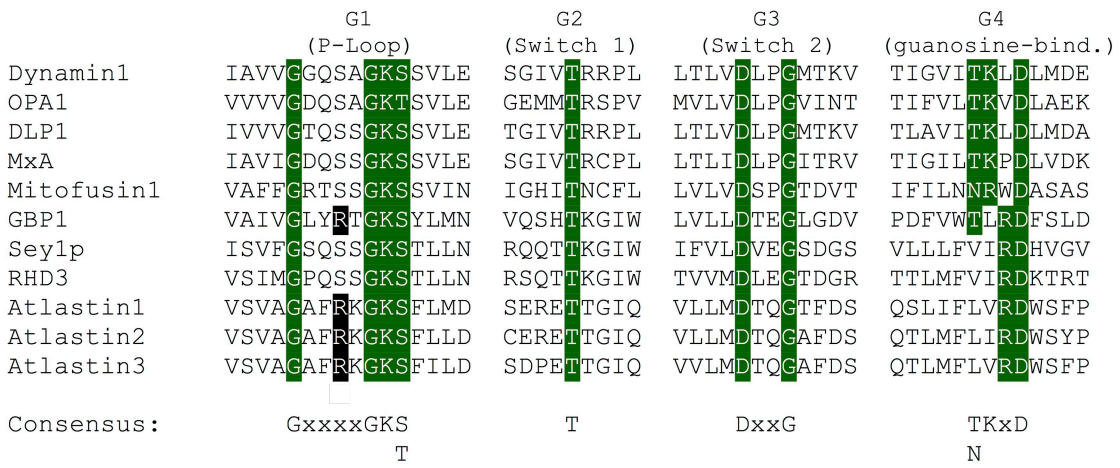

Figure 1.4. Dynamin superfamily nucleotide binding and switch region homology. Switch regions G1-4, regions of homology. Sequence alignment of several dynamin superfamily members shows conserved regions involved in nucleotide binding and hydrolysis, with strictly conserved residues highlighted in green. Arginine-77, specifically conserved in atlastins and GBPs, is highlighted in black.

Within the dynamin superfamily the sequence homology between members can vary widely; but in the GTPase domain the homology is closer, especially within the GTP binding motifs (switch regions G1-G4) that are essential for nucleotide binding and GTPase activity (Figure 1.4.). Using sequence homology, domain organization, and functional homology the dynamin superfamily can also be broken up into three subgroups, namely the classical dynamins, the dynamin-related proteins, and the GBP-related proteins. The classical dynamins all contain the following five domains: GTPase, middle, PH, GED, and PRD. By contrast, the dynamin-related proteins do not contain a PRD. This subfamily includes the proteins Dlp (Dynamin-like protein), MxA and B, OPA1 (Optic-atrophy 1), and mitofusin1 and 2. The last subfamily, the GBP-related proteins, is made up of GBP1-5 (Guanylate binding proteins: isoforms 1 through 5) and the atlastin1-3 (Figure 1.3.).

Dynamin, the founding member of this superfamily, is the best characterized in the group. There are three isoforms of dynamin in mammals. Dynamin-1 is found mostly in the brain, where it is involved in vesicle recycling in the presynapse.

Dynamin-2 is found all throughout the body, and is involved in endocytosis generally. Dynamin-3 is found in the testis, as well as the brain but mostly postsynaptically in neurons. These classical dynamins have been shown to take part in not only clathrin-mediated endocytosis (for which they are best known), but also budding of caveoli, podosome formation, phagocytosis, and cytokinesis. Much of the molecular mechanism for dynamin-mediated membrane fusion has been studied and is now well understood. Cyro-EM reconstructions of near full-length dynamin coated membrane tubes revealed that the middle domain and GED form a stalk-like structure involved in self-assembly. In addition, a three-helix bundle formed by the C terminus of the GTPase domain and the GED of dynamin, termed the bundle signaling element (BSE) was found to modulate dynamin function (26, 30), along with the PH domain, which regulates membrane binding and GTPase activity (31). Furthermore, membrane-mediated higher-order oligomerization stimulates dynamin GTPase activity, properties that have also been shown to be important for the function of other dynamin family members including MxA and GBP (32, 33). In a recent report, it was shown that following dynamin assembly on nanotubes, GTP addition caused disassembly of dynamin coats, but allowed shorter segments (2-3 rungs) of dynamin rings to catalyze membrane fission by application of elastic stress and coordination of membrane rearrangements through its PH domain (34).

The members of the subfamily of dynamin-related proteins have a similar domain structure to the classical dynamins, containing the large GTPase domain, middle domain, and GED. Dlp1, the member most closely related to the classical dynamins, also contains a PH domain, but the other members (MxA/B, OPA-1, and the mitofusins) do not. Instead, the mitofusins and OPA-1 contain a transmembrane domain. In the case of MxA/B it is thought that a cluster of positively charged residues on an unstructured loop (Loop 4 in the recently solved structure; located between the

middle domain and GED) mediates its interaction with lipids, since charge-reversal mutations in this loop abolish lipid binding (35). Excluding MxA and B, the remaining members of this subfamily are all localized to the mitochondria and are indispensible parts of mitochondrial fission and fusion events. Specifically, Dlp-1 (called Dnm1 in yeast) is necessary for the fission of this organelle, and similar to dynamin, forms ring-like structures around mitochondrial fission sites (36-38). Both mitofusin and OPA1 are required for mitochondrial fusion, with the mitofusins involved in fusion of the outer mitochondrial membrane and OPA1 (called Mgm1 in yeast) the inner mitochondrial membrane (39, 40).

The GBP-related subfamily of dynamin proteins contains only two subtypes, the GBPs and the atlastins (discussed in more detail in the next section); but these two protein types have very different functions and molecular details. Atlastins function as membrane fusogens, whereas GBPs function in pathogen resistance. The GBP's are a large group of proteins (with at least 5 isoforms in humans) that have been studied extensively, with many aspects of its biochemical and structural characteristics revealed in the last ten years (41-46). In addition to its anti-microbial activities, GBPs have been linked to new functions including cell proliferation (47), inhibition of matrix metalloprotease expression (48), inhibition of cell spreading (49), and intestinal epithelial cell development and barrier functions (50, 51). Yet, it is still not well understood how these proteins perform these functions *in vivo*. What is known about GBP is that it can be targeted to membranes via lipid modification on its CaaX motif (29, 52), and that some isoforms have the unique ability among dynamin superfamily members not only to hydrolyze GTP to GDP, but also to subsequently hydrolyze GDP to GMP. *In vitro* experiments have shown that GBP does rely on homodimerization to accelerate these reactions (42-46). Two crystal structures of GBP-1 have been solved including one full-length, nucleotide-free form and one of the GTPase domain alone

bound to the non-hydrolyzable GTP analog GppNHp. The full-length structure illustrates how the GTPase and middle domains can interact with its C-terminal GED, while the GTPase domain structure shows how two of these proteins can homodimerize when bound to nucleotide, consistent with *in vitro* studies.

Although the dynamin-superfamily members are somewhat diverse in sequence and functionality, comparisons between them can also be enlightening. Numerous structures of dynamin family proteins have been solved to date (Table 1.1.), and while they have indeed helped shed light on their own molecular mechanisms they also all show striking structural similarity, suggesting that these proteins may have more in common than their sequences suggest.

Table 1.1. Functions of mammalian Dynamin-like proteins at the membrane[a]

Name	Location in the cell	Functionality	Structures[b]	Refs
Classical Dynamin	Endocytic sites at the PM, ARP2/3 containing actin meshworks	Endocytic membrane fission, ARP2/3-dependent actin dynamics regulation	11	(23-27, 53-56)
Dynamin-related protein 1 (Dynamin 1-like protein)	Mitochondrial outer membrane, peroxisomes	Mitochondrial and peroxisomal fission/division	1	(36, 57-60)
Mitofusins	Mitochondrial outer membrane	Mitochondrial fusion	1	(57-61)
OPA1	Mitochondrial inner membrane	Mitochondrial fusion	0	(57-60, 62)
Myxovirus resistant proteins	ER	Antiviral	2	(32, 63, 64)
Guanylate-binding proteins	Intracellular vesicles	Viral and bacterial pathogen resistance	6	(43, 45, 65, 66)
Atlastins	ER, cis-Golgi	ER membrane fusion	10 (3 unique)	(10, 17, 67-70)

[a] *modified from Ferguson et al 2012* (20)
[b] *number of high-resolution structures solved to date; does not include EM reconstructions*

ATLASTIN

As the most distantly related members of the dynamin superfamily, atlastin proteins have several unique features. Unlike dynamin they have been shown to catalyze membrane fusion as opposed to fission. They are the smallest members of the superfamily at around 60kDa in size, but still contain a large (280AA) GTPase domain, a helical middle domain, a membrane interaction domain in the form of two transmembrane alpha helices, and an amphipathic C-terminal tail. The N- and C-termini of atlastin lie on the cytosolic side of the membrane, with the two transmembrane helices each spanning the membrane (16). Atlastin proteins have been found in all types of metazoans, and although there is no sequence homology, there are functional homologs of atlastin in yeast and plants, called Sey1p and RHD3 respectively (71, 72). Presently, the most well studied forms of atlastin are the human isoforms (mainly isoform 1), atlastin from *Drosophila melanogaster* (DmAtl), and atlastin from the plant *Arabidopsis thaliana* (called Root Hair Defective-3, RHD3).

In humans there exist three isoforms, named atlastin-1 through atlastin-3, with several alternative splice-forms listed in the Genbank. All three isoforms share a high degree of homology (66-72% identical) in their overall amino acid sequences, with most variability confined in the extreme N- and C-termini. The isoforms differ in their tissue expression patterns, with isoforms 2 and 3 expressed ubiquitously throughout the body and isoform 1 more restricted, found mostly in the central nervous system. Within the cell, all three isoforms contain ER retention signals on their C-termini and are found in the ER, with atlastin-1 also located in the cis-Golgi and growth cones of neurons (9). Within the ER atlastins are associated with three-way junctions. This reticular morphology is reduced and partially replaced by long, unbranched tubules when atlastin-2 and -3 are knocked down in HeLa cells (17, 73). A similar but more drastic phenotype is observed when DmAtl is knocked down in *Drosophila*, where the

authors observe extreme ER fragmentation in muscle and neurons (10). Since *Drosophila* only have a single isoform, the more pronounced effect of knocking down atlastin is unsurprising. It will take more study to figure out the functional disparities or overlaps between the three human isoforms and to determine whether they retain similar fusion capabilities as the *Drosophila* homolog.

Atlastin-1 has several interacting protein partners, including spastin/SPG4 (74, 75), reticulons/DP1 (17), REEP1/SPG31 (73), and NIPA1/SPG6 (76). Interestingly, atlastin-1 and most of its interaction partners have been identified as some of the most frequently mutated loci in Hereditary Spastic Paraplegia (HSP; also called Familial Spastic Paraplegia and Strumpell-Lorrain disease), a neurodegenerative disorder caused primarily by axonal degeneration of upper motor neurons (77). Atlastin-1 mutations have also been found in patients of another neurodegenerative disease called Hereditary Sensory Neuropathy Type I (HSN I). Both of these disorders involve progressive axonal degeneration of neurons that control muscles, and will be discussed in more detail in the next section. Atlastin's interaction with another HSP locus spastin, a microtubule severing enzyme, has been observed by a number of groups, but the exact mode of interaction remains unclear from these studies. In the case of atlastin's interactions with the reticulon and REEP1 (receptor accessory protein-1) proteins (integral membrane proteins that stabilize the highly-curved tubules found in the sER) the most likely domain of interaction with atlastin-1 is in their membrane-spanning domains (73). Although an interaction between HSP proteins NIPA-1 and atlastin-1 has been shown via immunoprecipitation studies (76), other groups have not confirmed this interaction, nor has the domain of interaction been identified.

It has been assumed that all isoforms of atlastin are involved in membrane fusion of ER tubules, but no conclusive *in vitro* evidence for this exists for any atlastin isoforms in human. The only convincing case for atlastin-mediated membrane fusion

is for the *Drosophila* atlastin homolog. First, as stated previously, an RNAi knockdown of atlastin in *Drosophila* causes fragmented ER (10). Perhaps more convincingly, DmAtl has been shown to fuse membranes *in vitro*. Using a simple lipid-mixing assay, reconstituted full-length DmAtl is able to fuse synthetic liposomes when GTP and a divalent cation (magnesium) are added, an activity that is blocked when a GTPase defective mutant is used (10). Interestingly, both of atlastin's transmembrane domains (the specific sequences of which was also important) and the C-terminal amphipathic helix are necessary for catalyzing membrane fusion (78). In addition to *Drosophila*, atlastins from *Xenopus laevis* gained some additional evidence for their role as fusogens when it was observed that antibodies against *Xenopus* atlastins (as well as GTP analogs) inhibited reformation of ER tubules from ER derived vesicles in *Xenopus* egg extracts (17).

Although atlastin-1 is implicated in ER fusion, it has also been associated in other cellular processes such as vesicle transport and BMP (bone morphogenetic protein) signaling (79, 80). In addition, evidence suggests that atlastin is indirectly and/or directly involved in the transport of sER tubules down the axon via microtubules where they serve as calcium stores (81-83), a necessary function in axons of any length (84, 85). One possible mode of regulation of this process is through the protein spastin-1 (specifically the M1, or long form), a microtubule binding and severing AAA ATPase (85), whose activity atlastin-1 has been shown to modulate. For these reasons, it will be important for future research to not only address the role of atlastins in membrane fusion but also assess other possible cellular functions that may have evolved in higher eukaryotes and that could contribute to disease.

HEREDITARY SPASTIC PARAPLEGIA AND HEREDITARY SENSORY NEUROPATHY

Perhaps the most interesting aspect of neurons is their complexity. Neurons have amazing capabilities that we are just beginning to understand, and without them our ability to think, move, and sense our environment would be impossible. However, the complexity of neuronal cells can ultimately become their downfall. Many types of neurodegenerative diseases have been found that affect each of the different types of neurons in the human body, but unlike other diseases that can be treated, cured, or otherwise overcome with modern medicine, neurodegenerative diseases currently have few proven treatments, are generally devastating in their effects (physically and/or mentally), and are usually progressive in nature.

One of the reasons neurons tend to be more prone to disease is because of their unusual architecture. Neurons are made up of a cell body, dendrites, and an axon. The cell body contains the nucleus and all of the organelles found in other cells (i.e. ER, Golgi complex, mitochondria, etc.). In order to communicate between neurons, they also contain dendrites, which are long, branched projections containing many types of receptors to sense incoming chemical and electric signals from neighboring neurons. Dendrites receive these signals by forming a connection (called a synapse) with the axon of a neighboring neuron. The axon is usually a single, long projection from the cell body that transmits a chemical or electric signal (first sensed in the dendrite) to the next neuron. Axons in the human nervous system can span vast distances, especially those of upper and lower motor neurons (Figure 1.5.). The main problem neurons face is how to get nutrients and signals from the cell soma to the ends of the neurites. Neurons solve this problem in different ways for axons and dendrites. Dendrites have areas of ER extensions and “Golgi outposts” to provide them with the proteins necessary for their function (86, 87). In axons, smooth ER tubules and mitochondria

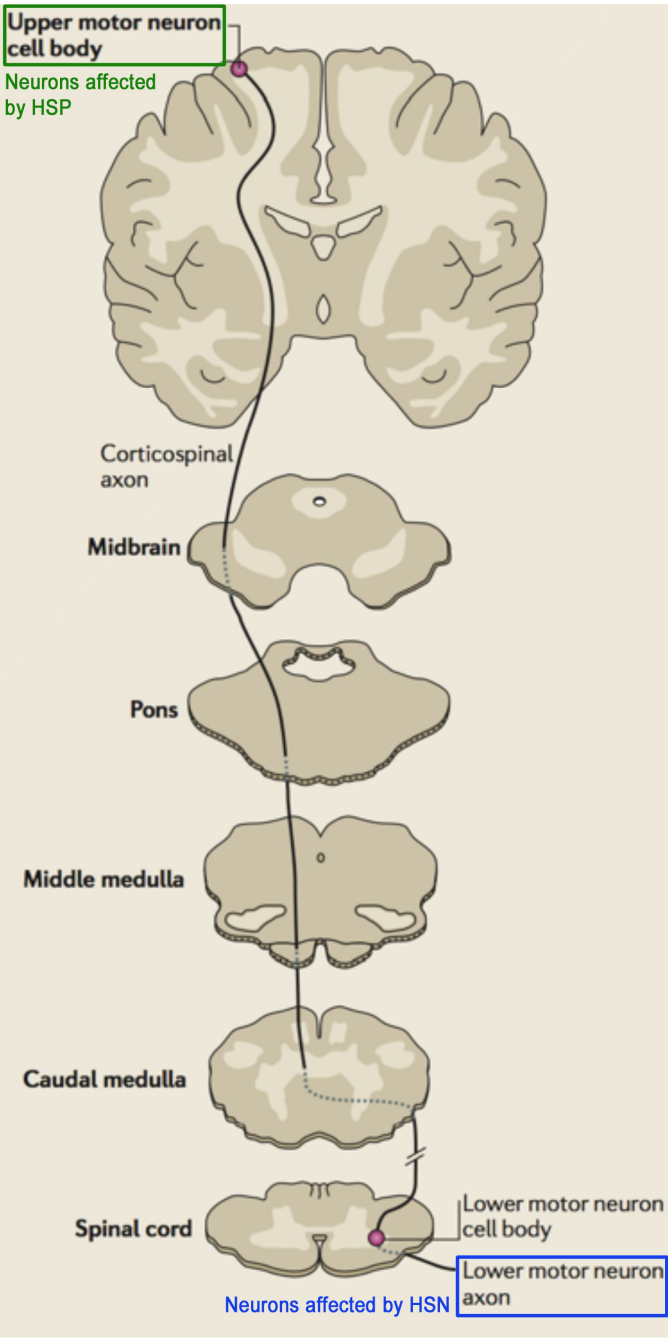

Figure 1.5. The human cortical spinal tract. Adapted from Goyal et al (7). Upper motor neurons that control voluntary muscle movement originate with their cell bodies in the motor cortex with axons that traverse down to the spinal cord (often crossing the midline) to connect to the cell body of lower motor neurons. Lower motor neuron cell bodies start in the spinal cord, where they receive signals from upper motor neurons, and extend their axons away eventually connecting directly to muscle cells. Green and blue boxes indicate areas affected by HSP and HSN, respectively.

are transported down the axon and are positioned strategically along the axon as well as in the synapse itself. These two organelles are necessary for axonal function and maintenance because of the axon's high-energy needs and reliance on calcium signaling (81, 88). Mitochondria, for example, are found concentrated in areas with extreme energy needs such as nodes of Ranvier and at the synapse (89-91). Organelles as well as vesicles containing necessary proteins from the soma are transported down the axon via anterograde microtubule transport. When transport in either direction is compromised, axonal degeneration followed by apoptosis can occur (92).

Hereditary Spastic Paraplegia (HSP) comprises a group of related inherited disorders, which cause progressive weakness and spasticity beginning in the lower extremities (77). The disease is characterized by axonal degeneration at the distal tips of long, cortical motor neurons. While over 40 genetic loci have been identified to cause this disease, just three of these loci, spastin-1 (SPG4), atlastin-1 (SPG3A), and REEP1 (SPG31), account for over 60% of cases (77). First discovered in 2001 (15), over 40 mutations in atlastin-1 have been identified to date, with the majority being missense mutations (Figure 1.6.). Although atlastin-1 mutations cause only about 10% of autosomal dominant HSP cases, they are the most common when the disease occurs in infancy and early childhood. In these cases, the disease progresses slowly or has no apparent progression, leading to the presumption that atlastin-1 may be involved in development as opposed to maintenance of affected neurons (9). Recently, this conjecture has gained some support in a study using zebrafish, where researchers observed an apparent inhibition of BMP signaling by atlastin-1 during neuronal development via regulation of BMP receptor trafficking, which affected motor axon architecture and larval mobility (79).

Hereditary Sensory Neuropathies (or Hereditary Sensory and Autonomic Neuropathies) are a group of five types of sensory/autonomic neuropathies (HSNI-V).

Juvenile and adult onset cases of HSN that are caused by autosomal dominant mutations are classified as HSN Type I, whereas the other four subtypes are autosomal recessive and are either congenital or early-onset diseases. It is a rare disease, though the exact prevalence is unknown. HSN I, for which atlastin-1 is one of four genetic loci identified to cause the disease, is characterized by progressive loss in sensation of the lower limbs with some motor involvement. Symptoms include general sensory loss, along with slow wound healing and chronic skin ulcers. Atlastin-1 was first discovered in HSN I patients in 2011, with two missense mutations and one truncation mutation so far identified (93) (Figure 1.6.). The other three genetic loci identified for HSN I include serine palmitoyltransferase long chain subunit 1 and 2 (SPTLC1 and 2) and Ras-related GTPase Rab7 (94-96).

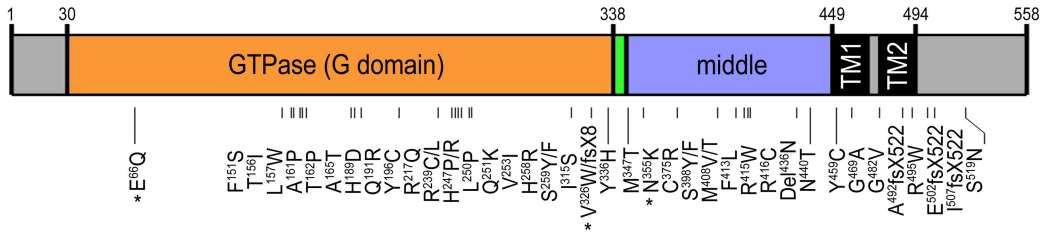

Figure 1.6. Atlastin-1 mutations. HSP and HSN mutations identified to date. Mutations are positioned at the location in the primary sequence in which they occur. An asterisk indicates mutations that are specific to HSN, while the remaining mutations are associated with only HSP.

Currently, no drug-based therapies exist for treating either of these neurological disorders. By studying the molecular mechanisms of proteins associated with these diseases, we can gain a better understanding of disease pathogenesis as well as axonal maintenance and development. Not only will this result in the possibility of new and improved therapies for patients, but it can also lead to breakthroughs in our understanding of how the nervous system works in general. Since atlastin-1 and other dynamin superfamily members are involved in a number of different

neurodegenerative diseases (including Charcot-Marie Tooth 2A, HSP, HSN I, and Optic Atrophy Type 1), a better understanding of their molecular mechanisms and functions within the cell will push the field of neurobiology closer to finding better ways to combat these and perhaps other debilitating neurological disorders.

OVERVIEW

Until now, most research pertaining to atlastin remained *in vivo*, which can yield significant and relevant results for figuring out the function of the protein in the cell. However, *in vivo* experiments are often complicated by many different factors such as the numerous unseen protein partners and chemical processes that occur in the cell, but not in a purified *in vitro* system. Furthermore, structural analysis of similar proteins, including dynamin and GBP, has contributed immensely to our understanding of how these proteins work and has guided new research efforts. The saying "form follows function" truly does apply to these and most biological molecules, and explains why structural biology has grown so rapidly in recent years. This thesis aims to use both biophysical and biochemical *in vitro* techniques to answer fundamental mechanistic questions pertaining to the protein atlastin-1. In particular, high-resolution structures solved via x-ray crystallography are used as a basis for designing more targeted biochemical and biophysical experiments in order to gain insight into the molecular mechanism of atlastin-1 membrane fusion.

In the second chapter, the first structures of atlastin are reported. In this study we utilized a construct of human atlastin-1 that contained the N-terminal soluble region of the protein, stopping just before the transmembrane domains but including

the large GTPase domain and middle domain (the catalytic core fragment). We were able to solve the structure of two completely different crystal forms from the same protein construct bound to the same nucleotide. Interestingly, these two crystal forms displayed distinct conformations, where the GTPase and middle domains were rotated with respect to one another, although it was unclear how the observed conformational change could occur with the same nucleotide. The protein also showed a weak dimeric assembly in the crystal structures. We were able to show that in solution the protein does indeed dimerize but not with the nucleotide contained in the crystal structures. In addition, we were able to map mutations in atlastin-1 that occur in patients suffering from HSP onto our structures, and analyze many of them for defects in activity and oligomerization.

In the third chapter, we have solved new structures of atlastin-1 bound to two new nucleotides. The four resulting crystal structures are virtually identical, excluding the bound nucleotide. These new nucleotide bound states reveal a much tighter, physiologically relevant dimeric state. Additionally, the structures uncover important changes in the nucleotide binding and hydrolysis motifs that are of fundamental importance to the molecular mechanism. Using knowledge gained from the structures in both this chapter and the previous chapter, we designed and implemented an assay to track changes in the conformation of atlastin-1 during nucleotide binding and hydrolysis. This analysis allowed us to better understand and follow the order of events during the hydrolysis cycle. Lastly, using information from one of our first structures as well as studies from other groups, we discovered a unique mode of internal regulation within atlastin-1's catalytic core. This mechanism allows atlastin-1

to regulate the process of nucleotide binding and possibly protein oligomerization. All of the data from chapters two and three have been condensed into a working model at the end of chapter three.

Chapter four delves deeper into the mechanism of atlastin-1 nucleotide binding and hydrolysis with two new structures including the isolated GTPase domain and an arginine finger mutant. Using these and our previous structures as guides, we also made two mutations in the catalytic core of atlastin-1. The first mutation probes the importance of a bulky aromatic side chain in a conserved nucleotide-binding motif. The second deletes an interaction observed in all of the dimeric structures, revealing the importance of this interaction on atlastin's GTPase activity.

The last chapter provides a summary of the results found in this thesis and extends them to future directions in the study of atlastin. Some preliminary results are presented and used as a platform to discuss new opportunities for exploration. In addition, the remaining issues and questions about atlastin membrane fusion and disease will be reviewed.

REFERENCES

1. Cooper GM (2000) *The Cell* (Sunderland, MA). 2nd Ed. Available at: http://www.ncbi.nlm.nih.gov/books/NBK9841/.

2. Lynes EM, Simmen T (2011) Biochimica et Biophysica Acta. *BBA - Molecular Cell Research* 1813:1893–1905.

3. Park SH, Blackstone C (2010) Further assembly required: construction and dynamics of the endoplasmic reticulum network. *EMBO Rep*.

4. Voeltz GK, Prinz WA, Shibata Y, Rist JM, Rapoport TA (2006) A Class of Membrane Proteins Shaping the Tubular Endoplasmic Reticulum. *Cell* 124:573–586.

5. McMahon HT, Gallop JL (2005) Membrane curvature and mechanisms of dynamic cell membrane remodelling. *Nat Cell Biol* 438:590–596.

6. Zimmerberg J, Kozlov MM (2005) How proteins produce cellular membrane curvature. *Nat Rev Mol Cell Biol* 7:9–19.

7. Goyal U, Blackstone C (2013) Untangling the web: Mechanisms underlying ER network formation. *BBA - Molecular Cell Research*:1–7.

8. Zhu P-P et al. (2003) Cellular Localization, Oligomerization, and Membrane Association of the Hereditary Spastic Paraplegia 3A (SPG3A) Protein Atlastin. *Journal of Biological Chemistry* 278:49063–49071.

9. Zhu P-P, Soderblom C, Tao-Cheng J-H, Stadler J, Blackstone C (2006) SPG3A protein atlastin-1 is enriched in growth cones and promotes axon elongation during neuronal development. *Hum Mol Genet* 15:1343–1353.

10. Orso G et al. (2009) Homotypic fusion of ER membranes requires the dynamin-like GTPase Atlastin. *Nature*.

11. Gao Y et al. (2012) Single Reconstituted Neuronal SNARE Complexes Zipper in Three Distinct Stages. *Science* 337:1340–1343.

12. Mcnew JA (2008) Regulation of SNARE-Mediated Membrane Fusion during Exocytosis. *Chem Rev* 108:1669–1686.

13. Hernandez JM et al. (2012) Membrane fusion intermediates via directional and full assembly of the SNARE complex. *Science* 336:1581–1584.

14. Wickner W, Schekman R (2008) Membrane fusion. *Nat Struct Mol Biol* 15:658–664.

15. Zhao X et al. (2001) Mutations in a newly identified GTPase gene cause autosomal dominant hereditary spastic paraplegia. *Nat Genet* 29:326–331.

16. Rismanchi N, Soderblom C, Stadler J, Zhu P-P, Blackstone C (2008) Atlastin GTPases are required for Golgi apparatus and ER morphogenesis. *Hum Mol Genet* 17:1591–1604.

17. Hu J et al. (2009) A Class of Dynamin-like GTPases Involved in the Generation of the Tubular ER Network. *Cell* 138:549–561.

18. Low H, Löwe J (2006) A bacterial dynamin-like protein. *Nature* 444:766–769.

19. Praefcke GJK, McMahon HT (2004) The dynamin superfamily: universal membrane tubulation and fission molecules? *Nat Rev Mol Cell Biol* 5:133–147.

20. Ferguson SM, Pietro De Camilli (2012) Dynamin, a membrane-remodelling GTPase. *Nat Rev Mol Cell Biol* 13:75–88.

21. Chen MS et al. (1991) Multiple forms of dynamin are encoded by shibire, a Drosophila gene involved in endocytosis. *Nature* 351:583–586.

22. Shpetner HS, Vallee RB (1989) Identification of dynamin, a novel mechanochemical enzyme that mediates interactions between microtubules. *Cell* 59:421–432.

23. Ford MGJ, Jenni S, Nunnari J (2011) The crystal structure of dynamin. *Nature*:1–6.

24. Faelber K et al. (2011) Crystal structure of nucleotide-free dynamin. *Nature*:1–7.

25. Chappie JS et al. (2011) A Pseudoatomic Model of the Dynamin Polymer Identifies a Hydrolysis-Dependent Powerstroke. *Cell* 147:209–222.

26. Chappie JS, Acharya S, Leonard M, Schmid SL, Dyda F (2010) G domain dimerization controls dynamin's assembly-stimulated GTPase activity. *Nature*.

27. Reubold TF et al. (2005) Crystal structure of the GTPase domain of rat dynamin 1. *Proc Natl Acad Sci USA* 102:13093–13098.

28. Gasper R, Meyer S, Gotthardt K, Sirajuddin M, Wittinghofer A (2009) It takes two to tango: regulation of G proteins by dimerization. *Nat Rev Mol Cell Biol* 10:423–429.

29. Nantais DE, Schwemmle M, Stickney JT, Vestal DJ, Buss JE (1996) Prenylation of an interferon-gamma-induced GTP-binding protein: the human guanylate binding protein, huGBP1. *Journal of leukocyte biology* 60:423–431.

30. Chappie JS et al. (2009) An intramolecular signaling element that modulates dynamin function in vitro and in vivo. *Mol Biol Cell* 20:3561–3571.

31. Kenniston JA, Lemmon MA (2010) Dynamin GTPase regulation is altered by PH domain mutations found in centronuclear myopathy patients. *EMBO J*.

32. Gao S et al. (2010) Structural basis of oligomerization in the stalk region of dynamin-like MxA. *Nature* 465:502–506.

33. Fres JM, Müller S, Praefcke GJK (2010) Purification of the CaaX-modified, dynamin-related large GTPase hGBP1 by coexpression with farnesyltransferase. *The Journal of Lipid Research* 51:2454–2459.

34. Shnyrova AV et al. (2013) Geometric Catalysis of Membrane Fission Driven by Flexible Dynamin Rings. *Science* 339:1433–1436.

35. Malsburg von der A, Abutbul-Ionita I, Haller O, Kochs G, Danino D (2011) Stalk Domain of the Dynamin-like MxA GTPase Protein Mediates Membrane Binding and Liposome Tubulation via the Unstructured L4 Loop. *Journal of Biological Chemistry* 286:37858–37865.

36. Fröhlich C et al. (2013) Structural insights into oligomerization and mitochondrial remodelling of dynamin 1-like protein. *EMBO J*:1–13.

37. Smirnova E, Griparic L, Shurland DL, van der Bliek AM (2001) Dynamin-related protein Drp1 is required for mitochondrial division in mammalian cells. *Mol Biol Cell* 12:2245–2256.

38. Labrousse AM, Zappaterra MD, Rube DA, van der Bliek AM (1999) C. elegans dynamin-related protein DRP-1 controls severing of the mitochondrial outer membrane. *Mol Cell* 4:815–826.

39. Wong ED (2003) The intramitochondrial dynamin-related GTPase, Mgm1p, is a component of a protein complex that mediates mitochondrial fusion. *J Cell Biol* 160:303–311.

40. Meeusen S et al. (2006) Mitochondrial Inner-Membrane Fusion and Crista Maintenance Requires the Dynamin-Related GTPase Mgm1. *Cell* 127:383–395.

41. Praefcke GJ, Geyer M, Schwemmle M, Robert Kalbitzer H, Herrmann C (1999) Nucleotide-binding characteristics of human guanylate-binding protein 1 (hGBP1) and identification of the third GTP-binding motif. *J Mol Biol* 292:321–332.

42. Praefcke GJK et al. (2004) Identification of residues in the human guanylate-binding protein 1 critical for nucleotide binding and cooperative GTP hydrolysis. *J Mol Biol* 344:257–269.

43. Prakash B, Praefcke GJ, Renault L, Wittinghofer A, Herrmann C (2000) Structure of human guanylate-binding protein 1 representing a unique class of GTP-binding proteins. *Nature* 403:567–571.

44. Kunzelmann S, Praefcke GJK, Herrmann C (2005) Nucleotide binding and self-stimulated GTPase activity of human guanylate-binding protein 1 (hGBP1). *Meth Enzymol* 404:512–527.

45. Ghosh A, Praefcke GJK, Renault L, Wittinghofer A, Herrmann C (2006) How guanylate-binding proteins achieve assembly-stimulated processive cleavage of GTP to GMP. *Nature* 440:101–104.

46. Abdullah N, Srinivasan B, Modiano N, Cresswell P, Sau AK (2009) Role of individual domains and identification of internal gap in human guanylate binding protein-1. *J Mol Biol* 386:690–703.

47. Guenzi E et al. (2001) The helical domain of GBP-1 mediates the inhibition of endothelial cell proliferation by inflammatory cytokines. *EMBO J* 20:5568–5577.

48. Guenzi E et al. (2003) The guanylate binding protein-1 GTPase controls the invasive and angiogenic capability of endothelial cells through inhibition of MMP-1 expression. *EMBO J* 22:3772–3782.

49. Weinlander K et al. (2008) Guanylate binding protein-1 inhibits spreading and migration of endothelial cells through induction of integrin 4 expression. *FASEB J* 22:4168–4178.

50. Mirpuri J et al. (2010) Commensal Escherichia coli Reduces Epithelial Apoptosis through IFN- A-Mediated Induction of Guanylate Binding Protein-1 in Human and Murine Models of Developing Intestine. *The Journal of Immunology* 184:7186–7195.

51. Schnoor M, Betanzos A, Weber DA, Parkos CA (2008) Guanylate-binding protein-1 is expressed at tight junctions of intestinal epithelial cells in response to interferon-γ and regulates barrier function through effects on apoptosis. *Mucosal Immunol* 2:33–42.

52. Modiano N, Lu YE, Cresswell P (2005) Golgi targeting of human guanylate-binding protein-1 requires nucleotide binding, isoprenylation, and an IFN-γ-inducible cofactor. *Proc Natl Acad Sci USA* 102:8680–8685.

53. Timm D et al. (1994) Crystal structure of the pleckstrin homology domain from dynamin. *Nat Struct Biol* 1:782–788.

54. Ferguson KM, Lemmon MA, Schlessinger J, Sigler PB (1994) Crystal structure at 2.2 A resolution of the pleckstrin homology domain from human dynamin.

Cell 79:199–209.

55. Niemann HH, Knetsch ML, Scherer A, Manstein DJ, Kull FJ (2001) Crystal structure of a dynamin GTPase domain in both nucleotide-free and GDP-bound forms. *EMBO J* 20:5813–5821.

56. Yang S et al. (2010) Crystal structure of the dynamin 3 GTPase domain bound with GDP. Available at: http://www.rcsb.org/pdb/explore/explore.do?structureId=3L43.

57. Okamoto K, Shaw JM (2005) Mitochondrial morphology and dynamics in yeast and multicellular eukaryotes. *Annu Rev Genet* 39:503–536.

58. Westermann B (2010) Mitochondrial fusion and fission incell life and death. *Nat Rev Mol Cell Biol* 11:872–884.

59. Hoppins S, Lackner L, Nunnari J (2007) The Machines that Divide and Fuse Mitochondria. *Annu Rev Biochem* 76:751–780.

60. Detmer SA, Chan DC (2007) Functions and dysfunctions of mitochondrial dynamics. *Nat Rev Mol Cell Biol* 8:870–879.

61. Koshiba T et al. (2004) Structural basis of mitochondrial tethering by mitofusin complexes. *Science* 305:858.

62. Cipolat S, Martins de Brito O, Dal Zilio B, Scorrano L (2004) OPA1 requires mitofusin 1 to promote mitochondrial fusion. *Proc Natl Acad Sci USA* 101:15927–15932.

63. Haller O, Gao S, Malsburg von der A, Daumke O, Kochs G (2010) Dynamin-like MxA GTPase: Structural Insights into Oligomerization and Implications for Antiviral Activity. *Journal of Biological Chemistry* 285:28419–28424.

64. Gao S et al. (2011) Structure of Myxovirus Resistance Protein A Reveals Intra- and Intermolecular Domain Interactions Required for the Antiviral Function. *Immunity* 35:514–525.

65. Kim BH et al. (2011) A Family of IFN- -Inducible 65-kD GTPases Protects Against Bacterial Infection. *Science* 332:717–721.

66. MacMicking JD (2004) IFN-inducible GTPases and immunity to intracellular pathogens. *Trends in Immunology* 25:601–609.

67. Byrnes LJ et al. (2013) Structural basis for conformational switching and GTP loading of the large G protein atlastin. *EMBO J*:1–16.

68. Byrnes LJ, Sondermann H (2011) Structural basis for the nucleotide-dependent

dimerization of the large G protein atlastin-1/SPG3A. *Proc Natl Acad Sci USA* 108:2216–2221.

69. Bian X et al. (2011) Structures of the atlastin GTPase provide insight into homotypic fusion of endoplasmic reticulum membranes. *Proc Natl Acad Sci USA* 108:3976–3981.

70. Moss TJ, Daga A, Mcnew JA (2011) Fusing a lasting relationship between ER tubules. *Trends Cell Biol*.

71. Brands A (2002) Function of a Plant Stress-Induced Gene, HVA22. Synthetic Enhancement Screen with Its Yeast Homolog Reveals Its Role in Vesicular Traffic. *PLANT PHYSIOLOGY* 130:1121–1131.

72. Wang H, Lockwood SK, Hoeltzel MF, Schiefelbein JW (1997) The ROOT HAIR DEFECTIVE3 gene encodes an evolutionarily conserved protein with GTP-binding motifs and is required for regulated cell enlargement in Arabidopsis. *Genes Dev* 11:799–811.

73. Park SH, Zhu P-P, Parker RL, Blackstone C (2010) Hereditary spastic paraplegia proteins REEP1, spastin, and atlastin-1 coordinate microtubule interactions with the tubular ER network. *The Journal of clinical investigation*.

74. Evans K et al. (2006) Interaction of two hereditary spastic paraplegia gene products, spastin and atlastin, suggests a common pathway for axonal maintenance. *Proc Natl Acad Sci USA* 103:10666–10671.

75. Sanderson CM et al. (2006) Spastin and atlastin, two proteins mutated in autosomal-dominant hereditary spastic paraplegia, are binding partners. *Hum Mol Genet* 15:307–318.

76. Botzolakis EJ, Zhao J, Gurba KN, Macdonald RL, Hedera P (2011) The effect of HSP-causing mutations in SPG3A and NIPA1 on the assembly, trafficking, and interaction between atlastin-1 and NIPA1. *Mol Cell Neurosci* 46:122–135.

77. Fink JK (2006) Hereditary spastic paraplegia. *Curr Neurol Neurosci Rep* 6:65–76.

78. Liu TY et al. (2012) Lipid interaction of the C terminus and association of the transmembrane segments facilitate atlastin-mediated homotypic endoplasmic reticulum fusion. *Proc Natl Acad Sci USA* 109:E2146–54.

79. Fassier C et al. (2010) Zebrafish atlastin controls motility and spinal motor axon architecture via inhibition of the BMP pathway. *Nat Neurosci* 13:1380–1387.

80. Zhao J, Hedera P (2012) Hereditary spastic paraplegia-causing mutations in atlastin-1 interfere with BMPRII trafficking. *Mol Cell Neurosci* 52:87–96.

81. Renvoisé B, Blackstone C (2010) Emerging themes of ER organization in the development and maintenance of axons. *Current Opinion in Neurobiology* 20:531–537.

82. Collin T, Marty A, Llano I (2005) Presynaptic calcium stores and synaptic transmission. *Current Opinion in Neurobiology* 15:275–281.

83. Spacek J, Harris KM (1997) Three-dimensional organization of smooth endoplasmic reticulum in hippocampal CA1 dendrites and dendritic spines of the immature and mature rat. *J Neurosci* 17:190–203.

84. Misko A, Jiang S, Wegorzewska I, Milbrandt J, Baloh RH (2010) Mitofusin 2 is necessary for transport of axonal mitochondria and interacts with the Miro/Milton complex. *J Neurosci* 30:4232–4240.

85. Lee M et al. (2009) Drosophila Atlastin regulates the stability of muscle microtubules and is required for synapse development. *Dev Biol* 330:250–262.

86. Hanus C, Ehlers MD (2008) Secretory Outposts for the Local Processing of Membrane Cargo in Neuronal Dendrites. *Traffic* 9:1437–1445.

87. Herpers B, Rabouille C (2004) mRNA localization and ER-based protein sorting mechanisms dictate the use of transitional endoplasmic reticulum-golgi units involved in gurken transport in Drosophila oocytes. *Mol Biol Cell* 15:5306–5317.

88. Hollenbeck PJ, Saxton WM (2005) The axonal transport of mitochondria. *Journal of Cell Science* 118:5411–5419.

89. Fabricius C, Berthold CH, Rydmark M (1993) Axoplasmic organelles at nodes of Ranvier. II. Occurrence and distribution in large myelinated spinal cord axons of the adult cat. *J Neurocytol* 22:941–954.

90. PALAY SL (1956) Synapses in the central nervous system. *J Biophys Biochem Cytol* 2:193–202.

91. Peters A, PALAY SL, Webster HD (1991) *The fine structure of the nervous system: neurons and their supporting cells*.

92. Perlson E, Maday S, Fu M-M, Moughamian AJ, Holzbaur ELF (2010) Retrograde axonal transport: pathways to cell death? *Trends Neurosci* 33:335–344.

93. Guelly C et al. (2011) Targeted High-Throughput Sequencing Identifies Mutations in atlastin-1 as a Cause of Hereditary Sensory Neuropathy Type I. *Am J Hum Genet* 88:99–105.

94. Dawkins JL, Hulme DJ, Brahmbhatt SB, Auer-Grumbach M, Nicholson GA (2001) Mutations in SPTLC1, encoding serine palmitoyltransferase, long chain base subunit-1, cause hereditary sensory neuropathy type I. *Nat Genet* 27:309–312.

95. Rotthier A et al. (2010) AR TICLEMutations in the SPTLC2 Subunitof Serine Palmitoyltransferase CauseHereditary Sensory and Autonomic Neuropathy Type I. *Am J Hum Genet* 87:513–522.

96. Verhoeven K et al. (2003) Mutations in the small GTP-ase late endosomal protein RAB7 cause Charcot-Marie-Tooth type 2B neuropathy. *Am J Hum Genet* 72:722–727.

CHAPTER 2

STRUCTURAL BASIS FOR THE NUCLEOTIDE-DEPENDENT DIMERIZATION OF THE LARGE G PROTEIN ATLASTIN-1/SPG3A[‡]

ABSTRACT

The large GTPase atlastin belongs to the dynamin superfamily that has been widely implicated in facilitating membrane tubulation, fission, and in select cases, fusion. Mutations spread across atlastin isoform 1 (atlastin-1) have been identified in patients suffering from hereditary spastic paraplegia (HSP), a neurodegenerative disorder affecting motor neuron function in the lower extremities. On a molecular level, atlastin-1 associates with high membrane curvature and fusion events at the endoplasmic reticulum and cis-Golgi. Here we report crystal structures of atlastin-1 comprising the G and middle domains in two different conformations. Although the orientation of the middle domain relative to the G domain is different in the two structures, both reveal dimeric assemblies with a common, GDP-bound G domain dimer. In contrast, dimer formation in solution is observed only in the presence of GTP and transition state analogs, similar to other G proteins that are activated by nucleotide-dependent dimerization. Analyses of solution scattering data suggest that upon nucleotide binding, the protein adopts a somewhat extended, dimeric conformation that is reminiscent of one of the two crystal structures. These structural studies suggest a model for nucleotide-dependent regulation of atlastin with implications for membrane fusion. This mechanism is affected in several mutants associated with HSP, providing insights into disease pathogenesis.

[‡] The following sections are reproduced from: Byrnes, L.J. and Sondermann, H. 2011. Structural basis for the conformational switching and GTP loading of the large G protein atlastin. PNAS. 108(6) pp2216-2221, doi: 10.1073/pnas.1012792108, with modifications to conform to the required format. LJB and HS conceived the project, designed and performed the experiments, analyzed the data, and wrote the paper.

INTRODUCTION

The superfamily of dynamin GTPases comprises a group of proteins that are involved in diverse cellular functions and are often closely associated with biological membranes (1). They function in a wide range of cellular scenarios including vesicle scission, fusion and fission of organelles, cytokinesis, and antiviral activity (1). Although they contain G domains that are structurally related to the small G proteins of the Ras superfamily, the corresponding domains in the dynamin superfamily are significantly larger (300 vs. 180 residues) and have a low intrinsic affinity for nucleotide. In addition, GTPases of this family often depend on nucleotide-dependent homodimerization to facilitate GTP hydrolysis rather than heterodimerization with a GTPase activating protein (2). Such a regulatory mechanism has been established for guanylate-binding protein (GBP) and dynamin (3, 4).

Dynamin and most dynamin-related proteins have a common domain architecture comprising a middle domain and a GTPase effector domain (GED) in addition to the N-terminal G domain (1). To date, the molecular mechanism responsible for nucleotide-dependent functional and structural transitions is best understood for the prototypical member dynamin, a protein that catalyzes membrane fission (5). In low-resolution models of dynamin, the middle domain and GED form a stalk-like structure that is involved in self-assembly (6, 7). Furthermore, the GED and the C terminus of the G domain form a three-helix bundle, called the bundle signaling element (BSE), which modulates dynamin function (4, 8). A recent crystal structure of a minimal G domain-GED fusion protein revealed dimeric G domains in a catalytically competent transition state that was proposed to play a role in the

disassembly of dynamin coats from membrane tubes proceeding the fission event (4, 9). Membrane binding and the GTPase of dynamin are further regulated by the pleckstrin homology (PH) domain, which is located at the tip of the stalk distal to the G domain and serves an autoregulatory function (7). Membrane-mediated, higher-order oligomerization of dynamin stimulates its basal GTPase activity further (10, 11). A similar model has been proposed for MxA, a dynamin-like protein involved in innate immunity (12).

Atlastin, a large G protein most closely related to the GBP subfamily, has been identified as a crucial protein in maintaining endoplasmic reticulum (ER) morphology and vesicle trafficking (13-17). Atlastin lacks a GED but instead contains two trans-membrane helices and a C-terminal domain in addition to its large G and middle domains, both of which face the cytoplasm (1, 18). Three isoforms of atlastin are found in humans, differing in their N and C termini as well as their expression patterns. Atlastin-2 and -3 are found ubiquitously and localize to the ER. In contrast, atlastin-1 is mainly found in the central nervous system, especially in neurons of the corticospinal tract as well as the cerebral cortex and hippocampus and is localized to the cis-Golgi and to a lesser extent in the ER (1, 18, 19). On a microscopic level, they are found to associate with three-way junctions in the ER, and their absence results in a loss of this morphology in exchange for long, unbranched tubules (2, 14, 20). At the ER, atlastin interacts with proteins from the reticulon and DP1 families (3, 4, 14), spastin/SPG4 (1, 21, 22), and REEP1/SPG31 (5, 20). Notably, members of these families have been found to be among the most frequently mutated loci in the

neurodegenerative disorder hereditary spastic paraplegia (HSP; also known as familial spastic paraplegia or Strumpell–Lorrain disease) (6, 7, 23).

HSP is a group of inherited disorders that cause progressive spasticity and weakness in the lower extremities. Mutations in the atlastin gene account for ~10% of autosomal dominant HSP cases (4, 8, 20). Nearly 40 atlastin-1 mutations have been identified in HSP patients, which affect upper motor neurons of the cortical spinal tract (4, 9, 23). The vast majority of disease-associated alleles encode missense mutations, with one deletion and several nonsense mutations also identified (7, 24, 25). Although atlastin accounts for only a tenth of the total HSP cases, it is the most common form in instances where the disorder occurs in infancy or childhood. In addition, many forms of atlastin show very slow progression or no apparent progression when the disease occurs in childhood, which led to the presumption that atlastin may have its effect in development rather than maintenance of affected neurons (10, 11, 26).

Understanding the molecular basis of atlastin function and of HSP-associated alleles will be important for diagnostic and prognostic applications as well as for a basic understanding of HSP pathogenesis. Furthermore, a structural analysis may reveal basic mechanisms controlling the cellular function of atlastin and related proteins. In this study, we determined the crystal structure of the cytoplasmic domain of human atlastin-1 in two different crystal forms, both bound to GDP. This portion of the protein comprises the G domain followed by the middle domain, a common modular architecture found in other members of the large G-protein family. Additionally, we determined the apo- and nucleotide-bound oligomerization states and

low-resolution structures of the cytoplasmic domain in solution by using static light scattering and small-angle X-ray scattering (SAXS). Several mutations associated with HSP affect GTPase activity and/or nucleotide-dependent dimerization suggesting a basis of disease pathogenesis.

MATERIALS AND METHODS

Protein expression and purification

The cytoplasmic domain of human atlastin-1 (residues 1–446) was amplified by standard PCR and cloned into a modified pET28a expression plasmid (Novagen) yielding N-terminally hexahistidine-tagged small ubiquitin-like modifier (SUMO) fusion proteins. The hexahistidine-tagged SUMO moiety was cleavable using the protease Ulp-1 from *Saccharomyces cerevisiae*.

Native and selenomethionine-derivatized proteins were overexpressed in *Escherichia coli* BL21 (DE3) (Novagen) or T7 Crystal Express (NEB) cells, respectively. For the expression of native proteins, cells were grown in Terrific Broth media supplemented with 50 μg/mL kanamycin at 37 °C. At a cell optical density corresponding to an absorbance of 0.8–1.0 at 600 nm (OD_{600}), the temperature was reduced to 18 °C, and protein production was induced with 1 mM IPTG. Selenomethionine-derivatized proteins were produced using a modified protocol (1, 27). Cells were grown in 4 L of LB to an OD_{600} of 0.7. The cells were centrifuged at 4,000 rpm for 20 min. Cell pellets were resuspended in 1 L of 1×M9 salt solution and centrifuged a second time. This step was repeated once more, and the final cell pellet was resuspended in 1 L of M9 minimal media supplemented with 50 μg/mL

kanamycin, 1× vitamin mix, 0.4% glucose, 2 mM $MgSO_4$, 25 μg/mL $FeSO_4$, and 40 μg/ml of each of the 20 amino acids with selenomethionine substituting for methionine. Cells were grown at 37 °C for an additional hour before reducing the temperature to 18 °C and inducing with 0.5 mM IPTG. After 16 h, cells were harvested by centrifugation, resuspended in NiNTA buffer A (25 mM Tris-Cl, pH 8.5, 500 mM NaCl, and 20 mM imidazole), and flash-frozen in liquid nitrogen.

After cell lysis by sonication and removal of cell debris by centrifugation, clear lysates were loaded onto NiNTA Superflow (Qiagen) equilibrated in NiNTA buffer A. The resin was washed with 20 column volumes of NiNTA buffer A, and proteins were eluted three times with 2 column volumes of NiNTA buffer A supplemented with 500 mM imidazole. Proteins were buffer exchanged into desalting buffer (25 mM Tris-HCl, pH 7.5, 400 mM NaCl, 5 mM β-mercaptoethanol), and affinity tags were removed by incubation with the yeast protease Ulp-1 at 4 °C overnight. Cleaved proteins were collected in the flow-through during NiNTA affinity chromatography and were subjected to size exclusion chromatography on a Superdex 200 column (GE Healthcare) equilibrated in gel filtration buffer (25 mM Tris-HCl, pH 7.5, 100 mM NaCl, 2 mM DTT). Proteins were concentrated on a Centricon ultrafiltration device (10 kDa cutoff; Millipore) to a final concentration of approximately 0.5–1 mM. Protein aliquots were flash-frozen in liquid nitrogen and stored at -80 °C.

Site-directed mutagenesis was carried out using Quikchange (Agilent) following the manufacturer's instructions, followed by validation through DNA sequencing.

Crystallization of atlastin-1

Crystals were obtained by hanging drop vapor diffusion mixing equal volumes of protein (30 mg/mL) and reservoir solution followed by incubation at 20 °C. Initial crystals were obtained in the presence of 2 mM GTPγS (Sigma) and 5 mM $MgCl_2$. For the *$P6_522$* crystals (form 1), the reservoir solution contained 0.1 M Bicine, pH 8.5, 30% PEG-MME550, and 0.1 M succinic acid, pH 7.0. Diamond-shaped crystals appeared within 3 d with typical dimensions of 0.30 mm × 0.15 mm × 0.2 mm. For cryoprotection, crystals were soaked in reservoir solution supplemented with 25% glycerol. For the *$P2_12_12_1$* crystals (form 2), the reservoir solution contained 20% PEG 3350 and 0.15 M ammonium phosphate dibasic. Crystals appeared as thin rods overnight with typical dimensions of 0.4 mm × 0.1 mm × 0.05 mm. Crystals were cryoprotected by soaking in the crystallization solutions supplemented with 15% xylitol. Cryopreserved crystals were flash-frozen and stored in liquid nitrogen. Data were collected on frozen crystals at 100 K.

Data reduction was carried out with the software package HKL2000 (1, 28). Experimental phases for *$P6_522$* crystals were obtained from single anomalous diffraction (SAD) experiments on crystals grown from selenomethionine-derivatived proteins. By using the software package Phenix (2, 29), 10 (out of 10) heavy atom positions could be determined. The structure of the *$P2_12_12_1$* crystal was determined by Molecular Replacement by using the software package PHENIX (3, 4, 29) with the GTPase domain and the middle domain of atlastin-1 as separate search models. Refinement in PHENIX (1, 29) and COOT (5, 30) yielded the final models. Data

collection and refinement statistics are summarized in Table 2.1. Illustrations were made in Pymol (DeLano Scientific).

Small-angle X-ray scattering (SAXS) data collection and processing

SAXS experiments were carried out at the Cornell High Energy Synchrotron Source (CHESS, beamline G1) at an electron energy of 8 KeV. Protein samples were prepared by incubating 100 μM protein with 1 mM nucleotide (or no nucleotide in the case of the apo-protein) and 5 mM $MgCl_2$ for 30 min at room temperature, and then loaded onto a size exclusion column (Superdex 200 GE 10/300) equilibrated in multiangle light scattering (MALS) buffer (25 mM Tris-HCl pH 7.4, 100 mM NaCl, 2 mM EGTA, 4 mM $MgCl_2$). Peak fractions were collected and concentrated. Protein concentrations were determined using UV Abs_{280} and theoretical extinction coefficients. Proteins were centrifuged at 13,200 rpm and 4 °C for 10 min prior to loading into a flow cell. Scattering data were collected in triplicate at protein concentrations between 1 and 10 mg/mL. Only data showing no sign of radiation damage or aggregation based on inspection of Guinier plots were used for further analysis. Background scattering was collected from MALS buffer. Scattering data were background corrected, averaged, and scaled by using the program BioXtas (Soeren Nielson) and were analyzed by using the programs GNOM and CRYSOL (6, 7, 31-33). Only scattering data with $S_{max} * R_g < 1.3$, computed from Guinier plots at low-angle regions, were considered for further analysis. Kratky plots were used to assess the folded state of the proteins and overall data quality. Distance distribution functions $P(r)$, R_g, and D_{max} were determined by using the program GNOM (4, 8, 33).

Distance distribution function from crystallographic models was calculated by using CRYSOL (4, 9, 32). SAXS-based shape reconstructions were carried out with the program GASBOR (7, 34) by using the P(r) function as the target. For each sample, 20 models were calculated, superimposed, averaged, and filtered by using the program DAMAVER (10, 11, 35). Similar results were obtained by using the scattering intensity as the target. During the modeling of the dimeric states, P2 symmetry was applied. Crystal structures were docked in the models using SUPCOMB (12, 36).

Size-exclusion chromatography-coupled multiangle light scattering (SEC-MALS)

Purified protein (~1 μg/μL or 20 μM, injected concentration) was subjected to SEC using a WTC-030S5 column (Wyatt Technology) equilibrated in MALS buffer (25 mM Tris-HCl pH 7.5, 100 mM NaCl, 4 mM $MgCl_2$, and 2 mM EGTA). Where specified, wild-type or mutant atlastin was incubated with GDP, GppNHp, or GDP•AlF_x (2 mM) for 30 min at room temperature prior to injection. The SEC was coupled to a static 18-angle light scattering detector (DAWN HELEOS-II) and a refractive index detector (Optilab T-rEX) (Wyatt Technology). Data were collected every second at a flow rate of 1 mL/min. Data analysis was carried out using the program ASTRA, yielding the molar mass and mass distribution (polydispersity) of the sample. Molecular weight distributions were determined by using the Multipeak Fitting Package in Igor Pro (WaveMetrics). For normalization of the light scattering detectors and data quality control, monomeric BSA (Sigma) was used.

GTPase activity assay

GTPase activity was measured using the Enzchek Phosphate Assay kit (Molecular Probes) following the manufacturer's instructions. Measurements were carried out in a 96-well plate (Nunc) in a total volume of 250 μL. Recombinant wild-type or mutant atlastin-1 was combined with 1 U/mL Purine Nucleoside Phosphorylase, 200 μM 2-amino-6-mercapto-7-methylpurine riboside, and provided buffer (20 mM Tris-HCl pH 7.5, 1 mM $MgCl_2$, 0.1 mM sodium azide). The plate was incubated at room temperature for 10 min, after which reactions were started by addition of 400 μM GTP (or alternatively, 50 mM Tris-HCl pH 7.5 for controls). Plates were assayed at 37 °C in a Powerwave XS microplate reader (BioTek). Absorbance at 360 nm was monitored in 30 s intervals for 30 min. Data were normalized to a phosphate standard curve, and initial velocities were calculated using the portion of the curve corresponding to the first 5% of consumed product. Data reported in Table 2.2. are means ± SD of three independent experiments.

Thermal melting

The circular dichroism signal of proteins (0.5 mg/mL) in CD buffer (10 mM NaH_2PO_4 pH 7.4, 100 mM NaCl) was monitored at 222 nm using an Aviv Circular Dichroism Spectrometer (Model 62ADS) between 10–90°C (cell pathlength, 1 mm; bandwidth, 1.5 nm; signal averaging time, 10 s; temperature step, 1 °C). Curves were differentiated and fitted to a Lorentzian distribution to estimate the melting temperature and errors of the measurement.

Nucleotide binding

Purified protein (~10 mg/mL) was subjected to size-exclusion chromatography (SEC) using a Superdex 200 10/300 GL column (GE Healthcare) equilibrated in MALS buffer. Where specified, wild-type or mutant atlastin-1 was incubated with no nucleotide, GDP, GppNHp, or GDP•AlF_x (2 mM) for 30 min at room temperature prior to gel filtration. The entire elution peak was concentrated and subjected to heat denaturation. Denatured proteins were precipitated by high-speed centrifugation and supernatants were filtered in 10 kDa-cutoff spin filters before injection into a reverse-phase HPLC column (Phenomenex Gemini C18) equilibrated in HPLC buffer (100 mM KH_2PO_4 pH 6.5, 10 mM tetrabutylammonium bromide, 7.5% acetonitrile, and 0.02% NaN_3).

RESULTS AND DISCUSSION

Crystal Structures of Atlastin-1.

The purified, cytoplasmic domain of human atlastin-1 (residues 1–446; Figure 2.1.A) crystallized in two distinct crystal forms (form 1: space group $p6_522$; form 2: $p2_12_12_1$; Table 2.1.). The form 1 crystals grown from selenomethionine-derivatized protein diffracted X-rays to a maximal resolution of 2.7 Å with one molecule in the asymmetric unit, and the structure was solved with single anomalous dispersion phasing (Figure 2.1.B). The form 2 crystals yielded a native dataset at 3.0 Å (four molecules/asymmetric unit), and the structure was solved by molecular replacement using the separated GTPase and middle domains as the search models (Figure 2.1.C).

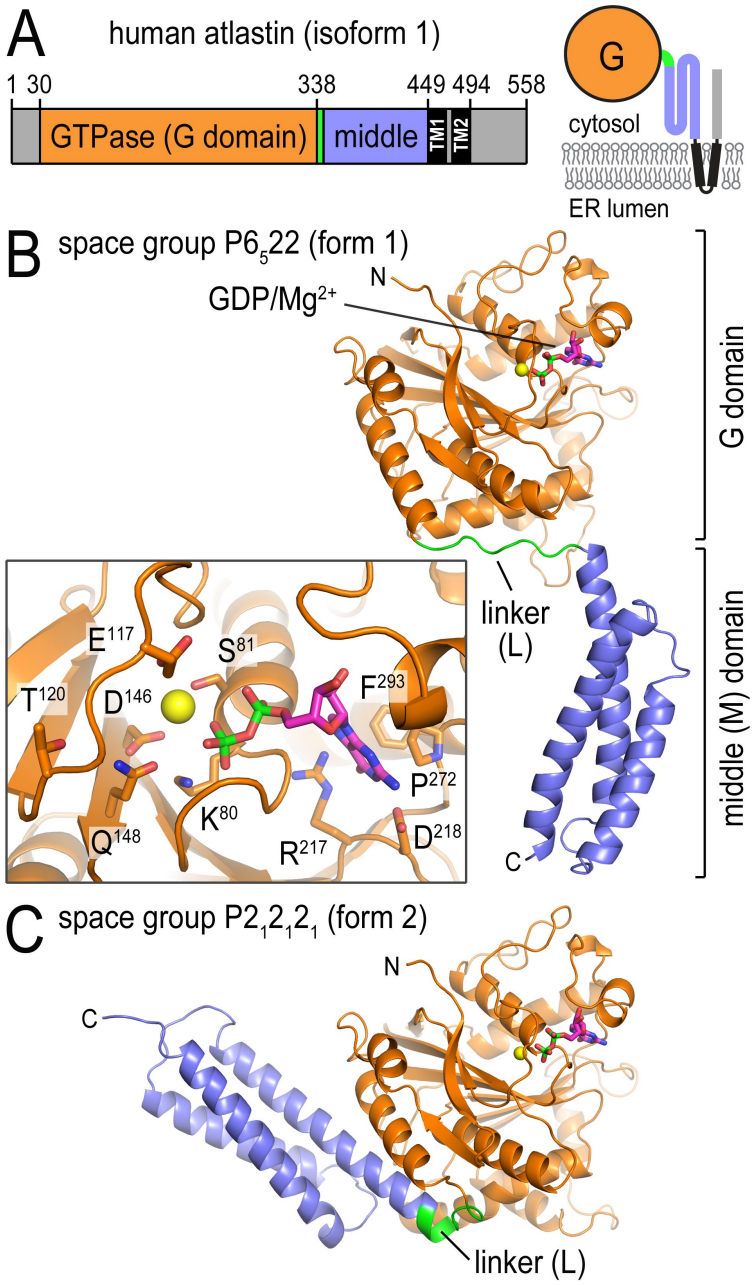

Figure 2.1. Structure of atlastin-1. (A) Domain organization of atlastin-1. The large G domain (orange) is connected to the middle domain (blue) by a short flexible linker (green) and is followed by two transmembrane helices (black) that span the membrane and a C-terminal domain. A topological model is shown (Right). The fragment used in this study consists of residues 1–446 of human atlastin-1. (B) Protomer structure of atlastin-1 in crystal form 1. (Inset) GDP/Mg^{2+}-coordinating residues as sticks. (C) Protomer structure of atlastin-1 in crystal form 2. The G domain is shown in a similar orientation as shown in B. GDP and Mg^{2+} are shown as sticks and spheres, respectively.

Table 2.1. Data collection and refinement statistics.		
	Atlastin-1 (1-446) form 1	**Atlastin-1 (1-446) form 2**
Data collection		
X-ray source	CHESS A1	CHESS A1
Wavelength (Å)	0.987	0.987
Space group	$P6_522$	$P2_12_12_1$
Unit cell parameters		
a, b, c, (Å)	145.4, 145.4, 104.2	104.4, 133.6, 175.8
α, β, γ (°)	90, 90, 120	90, 90, 90
Resolution range (Å)	50-2.70 (2.80-2.70)	50-3.00 (3.11-3.00)
No. of reflections		
Total	425,973	406,102
Unique	18,381 (1,795)	48,872 (4,788)
Completeness (%)	100 (100)	99.7 (99.0)
Redundancy	23.2 (18.3)	8.3 (7.3)
I/σ (I)	38.1 (3.2)	19.2 (2.8)
R_{meas} (%)	7.7 (84.4)	11.3 (68.3)
Refinement		
Phasing	SAD	MR
Unit cell content	1 GDP•Mg^{2+}-bound protomer	4 GDP•Mg^{2+}-bound protomers
R_{work}/R_{free} (%)	18.57/24.73	19.04/26.53
r.m.s. deviations		
Bond length (Å)	0.008	0.008
Bond angles (°)	1.252	1.241
No. of atoms		
Protein	3,289	12,732
Water	5	-
GDP•Mg^{2+}	29	116

Although crystallization for both forms was carried out in the presence of GTPγS, only density for the GDP moiety and a magnesium ion was observed (Figure 2.1.B, inset and Figure 2.2.A). In the present structures, the side chain of F^{76} within the P loop is positioned in such a way that the γ-phosphate moiety cannot be accommodated (Figure 2.2.A). Conformational changes typically accompanying GTP binding to G proteins would allow F^{76} to flip out to accommodate the terminal phosphate. Both the

slow hydrolysis of GTPγS as well as the presence of GDP as a major contaminant in the nucleotide solution may have contributed to this result (Figure 2.3.).

In both crystal forms, the N terminus of atlastin forms a globular GTPase domain fold similar to that of GBP1 (rmsd of 4.5 Å) (13-17, 37). The middle domain that connects to the transmembrane helices folds into a three-helix bundle (Figure 2.1.B and C). Most strikingly, the structures in the two crystal forms differ in their relative orientation of the G and middle domains with minimal variance of the individual domains (rmsd of 0.7 Å for both the G and middle domains; Figures 2.1. and 2.2.D). A rigid body rotation by ~90° of the middle domain relative to the G domain separates the two conformations, with the difference being realized by an alternative conformation of the connecting linker segment (residues 337–346). In contrast to the extended, random-coil conformation of the linker in form 1, it adopts a U-shaped turn in the form 2 crystals. In the latter case, it contributes an additional turn to the first helix of the middle domain, consistent with secondary structure predictions, and one of the two proline residues (P^{344}) in the linker segment serves as a helix cap (Figure 2.2.D). Mutation of this residue in the cytoplasmic domain of atlastin-1 ($P^{344}G$) renders the protein insoluble. The second proline (P^{342}) is located at the center of the linker. Similarly, proline residues are present at comparable positions in dynamin and other G proteins, where they serve as pivot points during nucleotide-dependent transitions (4, 18).

Although atlastin lacks a GED and its sequence conservation to other dynamin-like proteins predominantly resides in the G domain, there is a remarkable conservation with regard to domain arrangements, in particular, when the form 2

Figure 2.2. Crystal structures of GDP-bound atlastin-1. (A) Nucleotide binding site. Switch and nucleotide binding regions are highlighted as shades of blue. Conserved residues and the nucleotide are shown as sticks. A ($|F_{obs}|-|F_{calc}|$) electron density map contoured at 3.6σ is shown as calculated from a model before inclusion of GDP and magnesium. (Right) An overview of the G domain dimer observed in crystal form 1. (B) Sequence alignment of dynamin superfamily members in the conserved regions involved in nucleotide binding and hydrolysis. Conserved residues are highlighted in green and are shown below in the consensus sequence. Residues in the form 1 atlastin-1 dimers that form interfacial contacts are marked with an asterisk below the alignment. (C) Superposition of G domain dimers observed in crystal form 1 (space group $P65_22$) and 2 (space group $P2_12_12_1$). Protomer A from each dimer (gray and orange domain, respectively) were used as the reference for the superposition. (D) Superposition of the cytosolic domain of atlastin-1 in crystal form 1 and form 2 using the respective G domains as the reference. (Right) The major conformational differences that concern a G domain-internal helix and position of the middle domain accompanied by a restructuring of the linker segment.

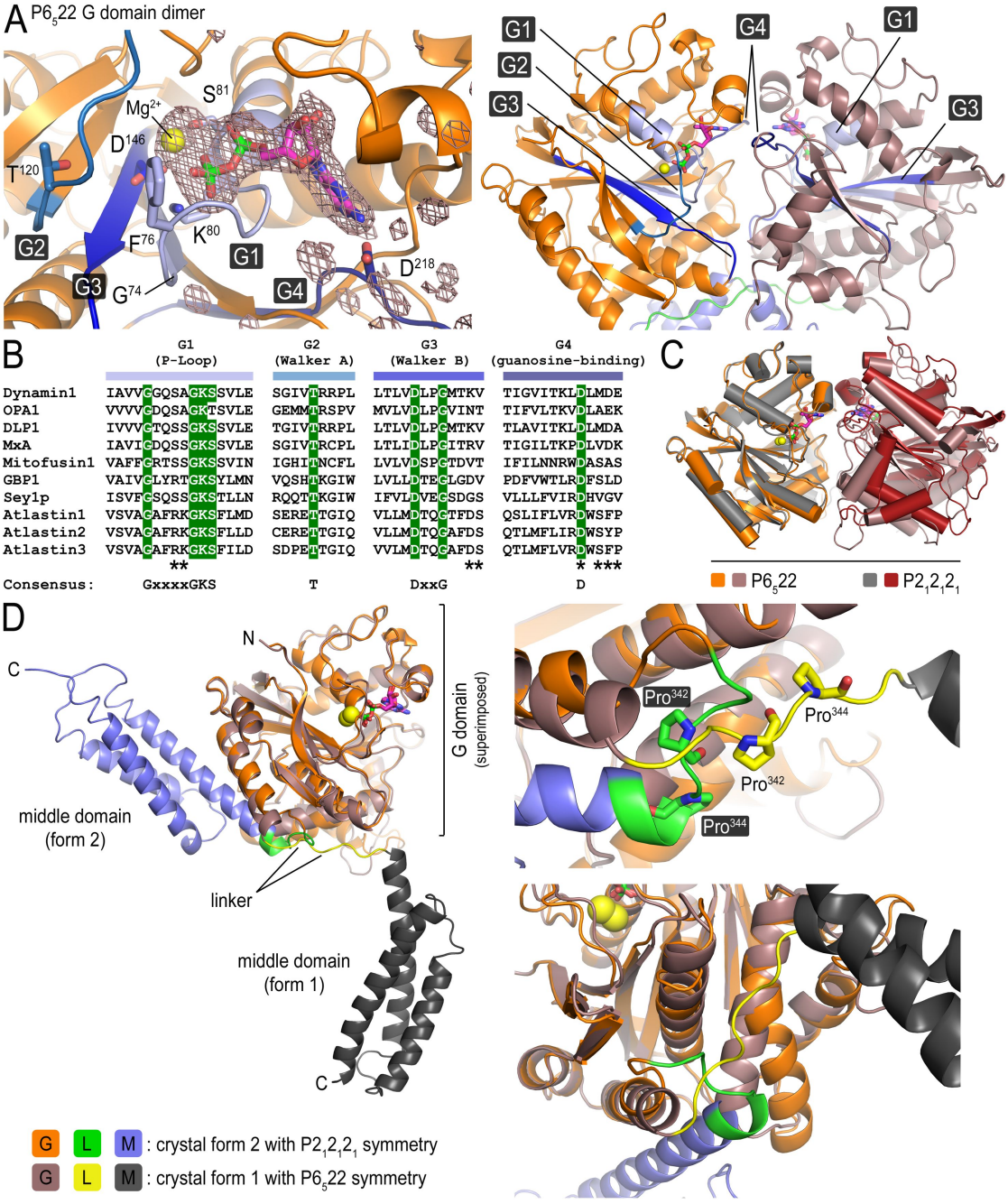
A
P6522 G domain dimer
Mg2+
S81
D146
T120
K80
F76
G74
D218
G1
G2
G3
G4
B
G1 (P-Loop)
G2 (Walker A)
G3 (Walker B)
G4 (guanosine-binding)
Dynamin1 IAVVGGQSAGKSSVLE SGIVTRRPL LTLVDLPGMTKV TIGVITKLDLMDE
OPA1 VVVVGDQSAGKTSVLE GEMMTRSPV MVLVDLPGVINT TIFVLTKVDLAEK
DLP1 IVVVGTQSSGKSSVLE TGIVTRRPL LTLVDLPGMTKV TLAVITKLDLMDA
MxA IAVIGDQSSGKSSVLE SGIVTRCPL LTLIDLPGITRV TIGILTKPDLVDK
Mitofusin1 VAFFGRTSSGKSSVIN IGHITNCFL LVLVDSPGTDVT IFILNNRWDASAS
GBP1 VAIVGLYRTGKSYLMN VQSHTKGIW LVLLDTEGLGDV PDFVWTLRDFSLD
Sey1p ISVFGSQSSGKSTLLN RQQTTKGIW IFVLDVEGSDGS VLLLFVIRDHVGV
Atlastin1 VSVAGAFRKGKSFLMD SERETTGIQ VLLMDTQGTFDS QSLIFLVRDWSFP
Atlastin2 VSVAGAFRKGKSFLLD CERETTGIQ VLLMDTQGAFDS QTLMFLIRDWSYP
Atlastin3 VSVAGAFRKGKSFILD SDPETTGIQ VVLMDTQGAFDS QTLMFLVRDWSFP
Consensus: GxxxxGKS T DxxG D
C
P6522
P2122
D
N
C
middle domain (form 2)
linker
middle domain (form 1)
G domain (superimposed)
Pro342
Pro344
Pro342
Pro344
G L M : crystal form 2 with P2122 symmetry
G L M : crystal form 1 with P6522 symmetry

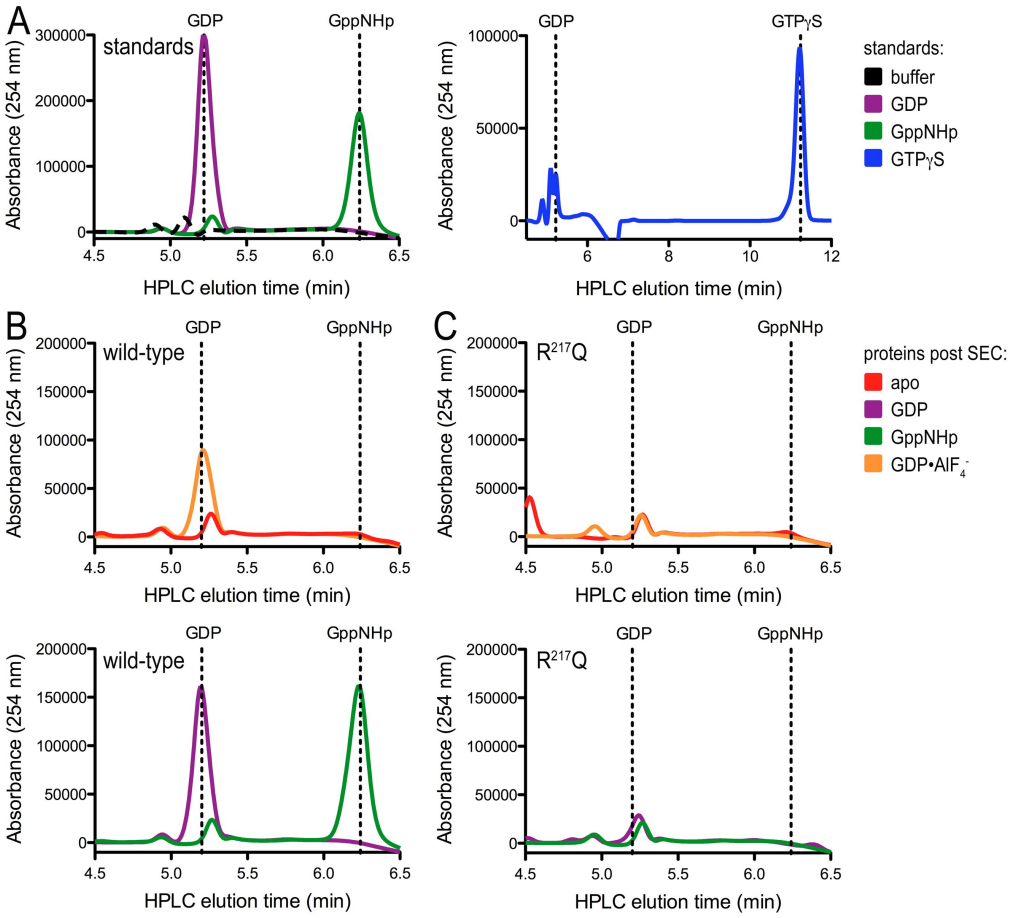

Figure 2.3. Nucleotide-bound state of atlastin wild-type and $R^{217}Q$. (A) Nucleotide standards for GDP (purple), GppNHp (green), and GTPγS (blue). (B) Wild-type atlastin-1. Protein was incubated with no nucleotide (red), GDP•AlF_x (orange), GDP (purple), or GppNHp (green). Excess nucleotide was removed by gel filtration. Nucleotides extracted from protein by heat denaturation were subjected to reverse-phase HPLC. Vertical dashed lines indicate elution positions for nucleotide standards. (C) Atlastin-1 mutant $R_{217}Q$. A similar analysis was performed for the point mutant $R^{217}Q$.

crystal structure is considered. In this conformation, atlastin's middle domain folds back onto the G domain and protrudes at a similar position as the BSE (including the GED) and middle domain in dynamin and GBP1, respectively (3, 4, 18, 19, 37, 38) (Figure 2.4.A and B). Although the contact region in GBP1 and atlastin is preserved, containing in part hydrophobic contacts between corresponding secondary structure motifs (Figure 2.5.A), the available dynamin structures lack the middle domain

impeding a more detailed comparison. Based on low-resolution structural reconstructions of near-full-length dynamin, the BSE and middle domain form a structural unit (7, 14, 20), and the BSE position in the crystal structure serves as an approximate projection of the middle domain (4, 14). The conservation of the overall architecture suggests a common molecular mechanism underlying the regulation and function of these distantly related proteins.

GBP1 and dynamin form G domain-mediated homooligomers in the presence of GTP and transition state analogs, but not in their apo- and GDP-bound states (Figure 2.4.A and B) (4, 21, 22, 37). Considering the symmetry mates in each crystal lattice, the atlastin structures provide insights into potential modes for dimerization, revealing a common interface observed in both structures formed between adjacent G domains (Figure 2.4.C). The two atlastin-1 G domain dimers align with an rmsd of 2 Å, with the main difference observed in the angle the G domains take with respect to each other (Figure 2.2.C). As a result, the interfacial area differs by 470 $Å^2$ considering only interactions between the G domains (1226 $Å^2$ and 756 $Å^2$ for form 1 and form 2 G domain dimers, respectively; Figure 2.5.C and D). The dimerization involves residues close to the nucleotide-binding pocket, especially within the P loop (G1), Walker B (G3) motif, and the guanosine-binding loop (G4) (Figure 2.2.A and B).

The relative position and orientation of the G domains and nucleotide are reminiscent of those seen in the crystal structures of GppNHp-bound GBP1 and dynamin when bound to GDP• AlF_4^- (Figures 2.4. and 2.5.B) (4, 23, 37). Specifically, there is a remarkable structural conservation with regard to the involvement of

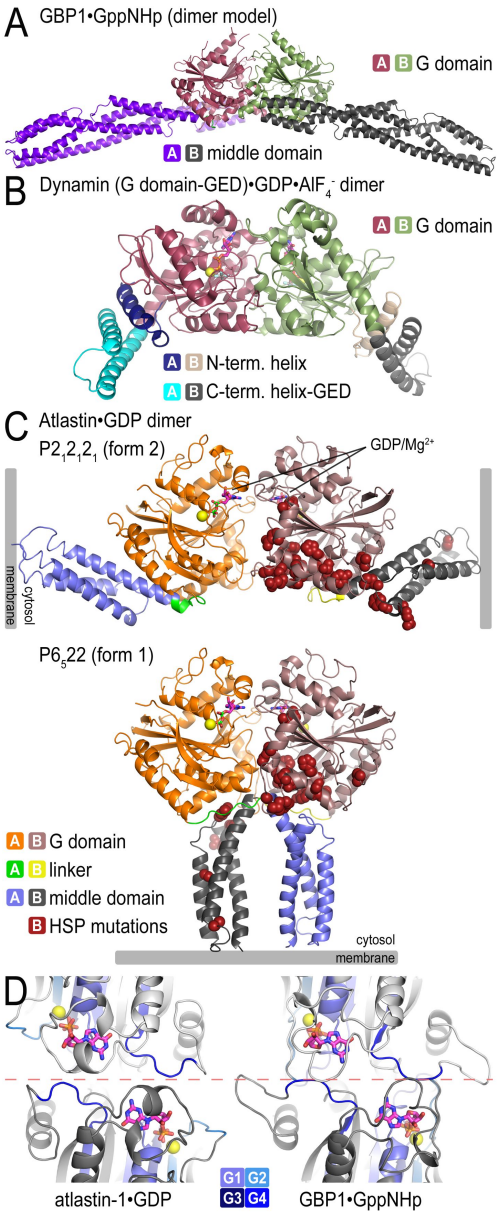

Figure 2.4. Crystallographic dimers of atlastin-1. (A) GBP1. A model for GTP-bound, full-length GBP1 was constructed according to (20, 37). (B) Dynamin. A dynamin G domain-GED fusion dimer bound to GDP•AlF_4^- is shown (PDB ID code 2X2E) (4, 23). (C) Atlastin-1. Dimers observed in crystal lattices with $P2_12_12_1$ symmetry (form 2, Upper) and with $P6_522$ symmetry (form 1, Lower) are shown. GDP and Mg^{2+} positions are indicated and are shown as sticks and spheres, respectively. Hypothetical membrane positions based on the location of the C terminus of the cytosolic domain are indicated. Positions of missense mutation associated with HSP are shown as residues displayed as red spheres in both forms. (D) Nucleotide arrangement and G domain dimer interface. The G domain dimer interfaces of atlastin-1 (form 1; Left) and GBP1 (Right; PDB ID code 2BC9) (3, 20) are shown. The protomers are colored in light and dark gray, with the nucleotide-binding regions (G1–G4) shown in shades of blue. Nucleotide and Mg^{2+} are shown as sticks and spheres, respectively. The dashed, red line separates the dimer halves, marking the interfacial region.

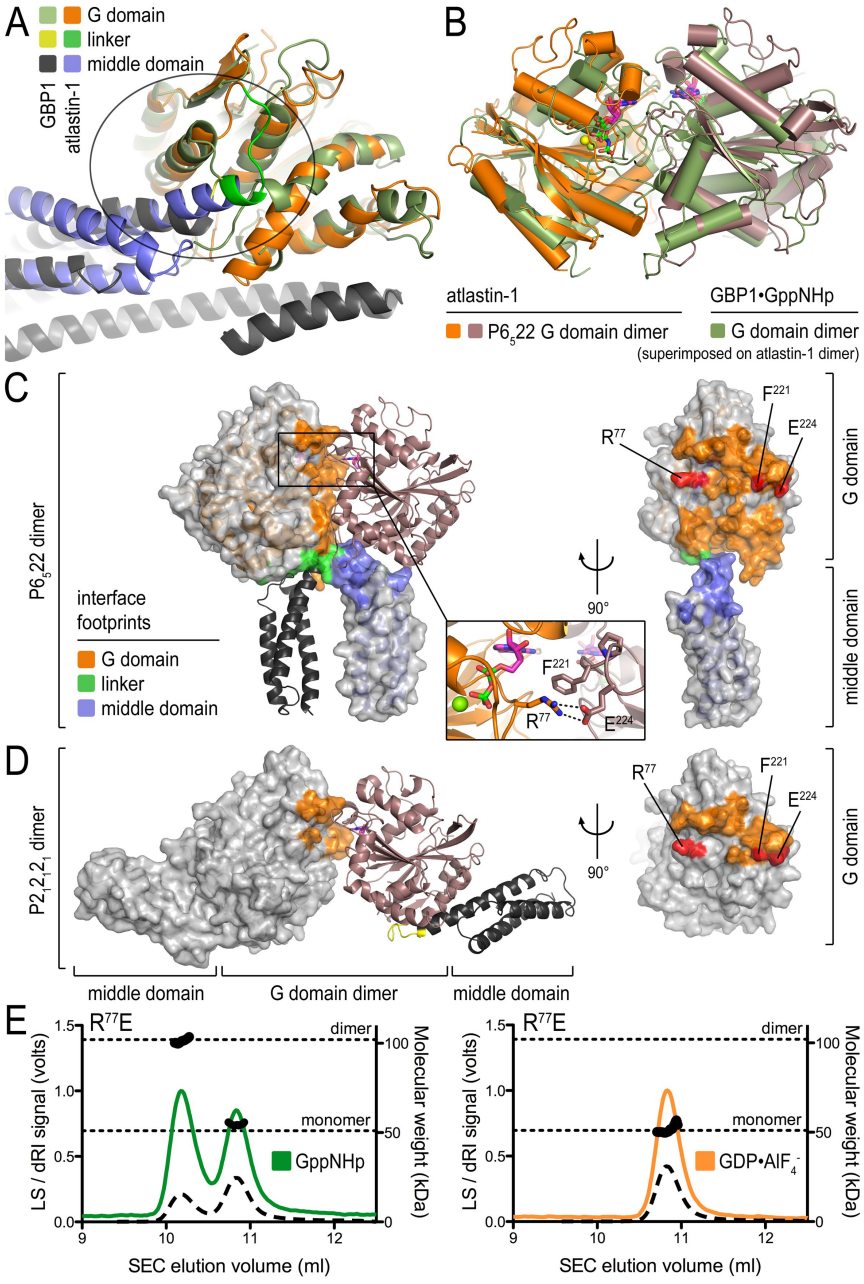

Figure 2.5. Comparison of atlastin-1 and GBP1 dimers. (A) Interdomain interface in GBP1 and atlastin-1. The G domain of GBP1 (green; PDB ID code 1DG3) was superimposed on the G domain of atlastin-1 (orange). The middle domains of GBP1 and atlastin-1 are colored in gray and blue, respectively. (B) The G domain dimer of GBP1 bound to GppNHp (PDB ID code 2BC9) was superimposed on the form 1 G domain dimer of atlastin-1 bound to GDP. (C) Form 1 G domain dimer interface. (D) Form 2 G domain dimer interface. Interfacial residues in form 1 dimers (C) or form 2 dimers (D) are shown in color on the surface of one half of the dimer. Key residues for dimer formation, R^{77} and its binding partners F^{221} and E^{224} in the adjacent G domain, are colored in red. (E) $R^{77}E$ mutant. Based on the crystal structures, we introduced a mutation into atlastin-1 at the dimerization interface and determined its oligomerization behavior by light scattering as described in Figure 2.6.

nucleotide-binding motifs between GBP1 and atlastin-1 (regions G1–G4) in dimerization, despite the difference in bound nucleotide species (Figure 2.4.D). Dynamin and GBP1 dimers bound to GDP•AlF_4^- or GppNHp, respectively, involve more extensive contributions of the P loop (G1) and the Walker A (G2) motif compared to the GDP-bound dimers of atlastin-1 (Figure 2.4.D) (3, 4, 24, 25). Most notably, the two crystallographic atlastin-1 dimer forms differ in their relative position of the middle domains with respect to the G domain dimers (Figure 2.4.C). Although the form 2 dimer resembles GBP1 or dynamin assemblies with the middle domains pointing in opposite directions (3, 4, 26, 37), the form 1 dimer of atlastin is distinct from those because the middle domains run in parallel (Figure 2.4.). In this conformation, the linker segments and middle domains cross over, contributing an additional 1571 $Å^2$ to the overall interfacial area (Figures 2.4.C and 2.5.C). Although the middle domains in the form 1 structure protrude in the same direction and would locate to proximal membrane regions via the successive transmembrane domains (Figure 2.4.C), the functional relevance for this conformation remains elusive.

Nucleotide-Dependent Dimerization of Atlastin.

GTP-dependent dimerization of dynamin and GBP1 establish the catalysis-competent states of these enzymes (4, 37). Several lines of evidence support the presence of a conserved dimerization-based GTPase mechanism for atlastin-1, in addition to the crystallographic observation that GDP-bound atlastin dimers are reminiscent of dimeric states of dynamin and GBP1. Similar to the latter cases, nucleotide-free (apo) and GDP-bound atlastin-1 (residues 1–446) elute in single peaks

from a size-exclusion column with molecular weights determined by in-line, multiangle light scattering close to that calculated for monomers based on the primary sequence (49.2 or 49.3 kDa, respectively; theoretical molecular weight: 51.1 kDa) (Figure 2.6. and Table 2.2.). Incubation of the protein with the GTP analog GppNHp or the transition state analog GDP• AlF_x promotes dimerization, indicated by an earlier elution volume and an average molecular weight of 99.2 kDa or 98.2 kDa, respectively.

A nonconservative mutation in residue R^{77} ($R^{77}E$), a residue located at the G domain dimer interface in the crystal structures of atlastin (Figure 2.5.C), renders the protein monomeric in the presence of GDP•AlF_x, and only partially dimeric when bound to GppNHp, indicating that the crystallographic interface is also involved in the nucleotide-dependent dimerization of the protein in solution (Figure 2.5.E and Table 2.2.). The mutant protein is also devoid of GTPase activity (Table 2.2.), indicating that dimerization can have an impact on enzymatic activity.

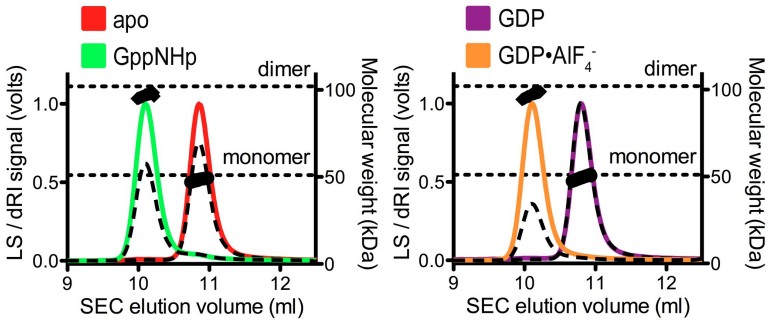

Figure 2.6. Atlastin-1 oligomerization in solution. SEC-MALS data are shown for wild-type atlastin-1 (residues 1–446) in its apo-state (red) or bound to GppNHp (green), GDP (purple), or GDP•AlF_x (orange). The signal from the 90°-scattering detector and refractive index detector are shown as solid, colored lines and black dashed lines, respectively (Left, Y axis). Average molecular weight as calculated every second across the protein elution peak is shown as black circles (Right, Y axis). Theoretical molecular weights based on primary sequence for the monomer and dimer are indicated as horizontal, dashed lines. Proteins (20 μM) were incubated with nucleotides (2 mM) prior to SEC-MALS analysis.

Table 2.2. Oligomeric state and GTPase activity of wild-type and mutant atlastin-1.[a]				
Protein	**Property**	**Apo**	**GppNHp**	**GDP•AlF_4^-**
wild-type				
	Molecular weight[b]	49.2kDa	99.2kDa	98.2kDa
	Polydispersity[b]	1.001 (±0.004)	1.000 (±0.004)	1.000 (±0.003)
	T_m (C)[c]	51.23 (±0.92)		
	GTPase activity (μM P_i/min/μM Enz)	5.33 (±0.09)		
$R^{77}E$				
	Molecular weight[b]	50.4kDa	101.2kDa	51.4kDa
	Polydispersity[b]	1.000 (±0.010)	1.000 (±0.010)	1.000 (±0.020)
	T_m (C)[c]	n.d.		
	GTPase activity (μM P_i/min/μM Enz)	0.01 (±0.01)		
$T^{156}I$				
	Molecular weight[b]	47.9kDa	96.6kDa	96.9kDa
	Polydispersity[b]	1.000 (±0.002)	1.000 (±0.002)	1.000 (±0.003)
	T_m (C)[c]	52.77 (±0.1.43)		
	GTPase activity (μM P_i/min/μM Enz)	2.25 (±0.03)		
$T^{157}W$				
	Molecular weight[b]	50.9kDa	99.8kDa	102.3kDa
	Polydispersity[b]	1.001 (±0.010)	1.000 (±0.020)	1.000 (±0.020)
	T_m (C)[c]	51.74 (±1.03)		
	GTPase activity (μM P_i/min/μM Enz)	5.35 (±0.04)		
$H^{189}D$				
	Molecular weight[b]	50.5kDa	100.6kDa	103.3kDa
	Polydispersity[b]	1.000 (±0.020)	1.000 (±0.010)	1.000 (±0.040)
	T_m (C)[c]	52.88 (±1.09)		
	GTPase activity (μM P_i/min/μM Enz)	3.14 (±0.25)		
$Q^{191}R$				
	Molecular weight[b]	50.5kDa	52.7kDa	100.8kDa
	Polydispersity[b]	1.000 (±0.020)	1.001 (±0.040)	1.000 (±0.020)
	T_m (C)[c]	50.49 (±0.93)		
	GTPase activity (μM P_i/min/μM Enz)	4.48 (±0.08)		
$Y^{196}C$				
	Molecular weight[b]	52.8kDa	98.1kDa	100.1kDa
	Polydispersity[b]	1.000 (±0.050)	1.000 (±0.010)	1.000 (±0.020)
	T_m (C)[c]	51.91 (±1.11)		
	GTPase activity (μM P_i/min/μM Enz)	5.38 (±0.06)		
$R^{217}Q$				

	Molecular weight[b]	49.0kDa	49.0kDa	48.9kDa
	Polydispersity[b]	1.000 (±0.003)	1.001 (±0.003)	1.001 (±0.003)
	T_m (C)[c]	55.82 (±1.76)		
	GTPase activity (μM P_i/min/μM Enz)	0.01 (±0.01)		
$R^{239}C$				
	Molecular weight[b]	48.7kDa	98.8kDa	97.3
	Polydispersity[b]	1.000 (±0.003)	1.000 (±0.003)	1.000 (±0.003)
	T_m (C)[c]	52.60 (±1.01)		
	GTPase activity (μM P_i/min/μM Enz)	2.74 (±0.17)		
$H^{247}R$				
	Molecular weight[b]	51.0kDa	99.1kDa 53.3kDa	100.1kDa
	Polydispersity[b]	1.000 (±0.020)	1.000 (±0.010), 1.000 (±0.030)	1.000 (±0.010)
	T_m (C)[c]	51.87 (±1.04)		
	GTPase activity (μM P_i/min/μM Enz)	1.48 (±0.04)		
$L^{250}P$				
	Molecular weight[b]	53.1kDa	100.4kDa	100.7kDa
	Polydispersity[b]	1.004 (±0.060)	1.000 (±0.010)	1.000 (±0.020)
	T_m (C)[c]	52.12 (±1.22)		
	GTPase activity (μM P_i/min/μM Enz)	3.31 (±0.21)		
$H^{258}R$				
	Molecular weight[b]	48.2kDa	95.9kDa	95.9kDa
	Polydispersity[b]	1.000 (±0.002)	1.000 (±0.002)	1.000 (±0.002)
	T_m (C)[c]	50.83 (±1.21)		
	GTPase activity (μM P_i/min/μM Enz)	2.50 (±0.09)		
$S^{259}F$				
	Molecular weight[b]	50.7kDa	99.2kDa	100.3kDa
	Polydispersity[b]	1.000 (±0.020)	1.000 (±0.010)	1.0 (±0.010)
	T_m (C)[c]	52.09 (±1.21)		
	GTPase activity (μM P_i/min/μM Enz)	2.34 (±0.04)		
$I^{315}S$				
	Molecular weight[b]	47.2kDa	92.0kDa	93.5kDa
	Polydispersity[b]	1.001 (±0.005)	1.000 (±0.003)	1.000 (±0.003)
	T_m (C)[c]	52.06 (±1.28)		
	GTPase activity (μM P_i/min/μM Enz)	3.42 (±0.04)		
$Y^{336}H$				
	Molecular weight[b]	50.4kDa	92.7kDa 53.1kDa	99.0kDa

	Polydispersity[b]	1.000 (±0.020)	1.000 (±0.020) 1.000 (±0.020)	1.000 (±0.010)
	T_m (C)[c]	50.57 (±0.96)		
	GTPase activity (μM P_i/min/μM Enz)	4.24 (±0.11)		
$S^{398}Y$				
	Molecular weight[b]	48.8kDa	98.6kDa	98.0kDa
	Polydispersity[b]	1.001 (±0.003)	1.000 (±0.003)	1.000 (±0.003)
	T_m (C)[c]	44.99 (±2.79)		
	GTPase activity (μM P_i/min/μM Enz)	3.25 (±0.03)		
$M^{408}T$				
	Molecular weight[b]	50.4kDa	87.0kDa 53.4kDa	99.6kDa
	Polydispersity[b]	1.000 (±0.020)	1.000 (±0.050) 1.002 (±0.020)	1.000 (±0.010)
	T_m (C)[c]	49.22 (±0.93)		
	GTPase activity (μM P_i/min/μM Enz)	5.12 (±0.17)		
$M^{408}V$				
	Molecular weight[b]	49.1kDa	91.0kDa 49.8kDa	97.0kDa
	Polydispersity[b]	1.000 (±0.004)	1.000 (±0.005) 1.000 (±0.005)	1.000 (±0.003)
	T_m (C)[c]	50.45 (±0.95)		
	GTPase activity (μM P_i/min/μM Enz)	3.11 (±0.14)		

[a]: The soluble, cytoplasmic domain of atlastin-1 (residues 1-446) was used in these experiments.
[b]: Molecular weight and polydispersity indices were determined by using SEC-MALS.
[c]: protein stability was determined based on measurements of the melting temperature by circular dichroism spectroscopy.

Next, we turned to SAXS to gain further insight into the solution structure of dimeric atlastin. By using a monodisperse protein sample in diffraction experiments, accurate shape information in the form of the radius of gyration (R_g), the maximal diameter of the particle (D_{max}), and the distance distribution function ($P(r)$) can be obtained (39, 40). The experimental scattering curves and $P(r)$ functions for the cytoplasmic domain of atlastin-1 differ in the nucleotide-free, GDP-, GppNHp- and

GDP•AlF$_x$-bound states (Figure 2.7.A), indicating that the structures of these intermediates feature differences (a detailed analysis of the monomeric, apo-, and GDP-bound states is provided as SI Text). The dimeric, GppNHp-, and GDP•AlF$_x$-bound states have overall similar *P(r)* profiles but vary slightly in their D_{max} and R_g with the GDP•AlF -bound specimen being more extended (D_{max}/R_g: 120⁄36 Å vs. 125⁄37 Å for the GppNHp- and GDP•AlF$_x$-bound states, respectively; Figure 2.7.A and Table 2.3.).

We compared the solution scattering data with the crystallographic dimer models (Figure 2.8.). Both solution states are more extended than the crystallographic form 1 dimer but shorter than the form 2 dimer (Figure 2.8.A and Table 2.3.). The position and shape of the main peak in the theoretical *P(r)* functions calculated from

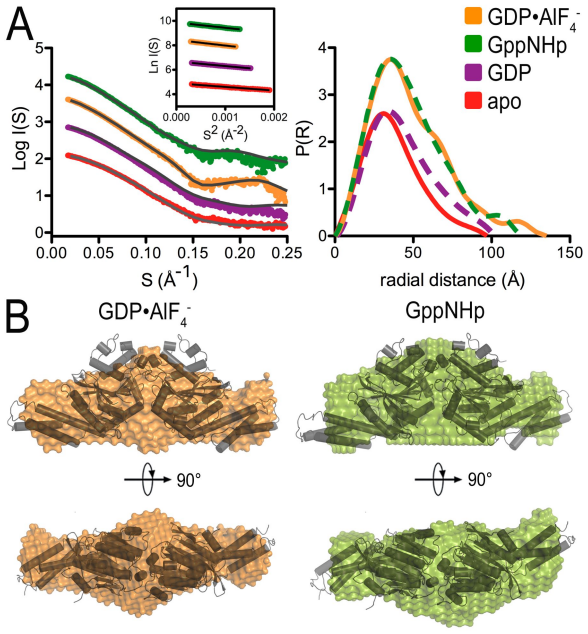

Figure 2.7. Small-angle X-ray scattering. (A) Solution scattering data for atlastin-1. Intensity plots and P(r) functions for apo (red), GDP-bound (purple), GppNHp-bound (green), and GDP•AlF$_x$-bound (orange) atlastin-1 (residues 1–446) are shown. (Left, Inset) Corresponding Guinier plots. (B) SAXS-based shape reconstructions for nucleotide-bound solution states of atlastin-1. The dimeric form 2 crystal structure was docked in the models as a reference and is shown as a cartoon presentation.

Table 2.3. SAXS data statistics and dimensions of crystallographic models.

	R_g (Å)[a]	D_{max} (Å)[a]	V_p (nm^3)[b]	χ_{best}[c]
SAXS data				
Apo	30±0.1	97±2.5	90.4	1.694
GDP	33±0.1	101±2.5	138.7	1.563
GppNHp	36±0.1	120±2.5	157.7	1.093
GDP•AlF_x	37±0.1	125±2.5	156.7	1.325
Crystallographic models				
Form 1 monomer	29	104	n. a.	n. a.
Form 2 monomer	24	86	n. a.	n. a.
Form 1 dimer[d]	31	104	n. a.	n. a.
Form 2 dimer[e]	37	150	n. a.	n. a.

[a]: R_g and D_{max} were determined using the program GNOM (6). Similar values for Rg were obtained from analysis of the Guinier equation and data that satisfies $Q_{max} \times R_g < 1.3$. Values for the crystallographic models were calculated with Crysol (5).
[b]: V_p is the excluded volume (Porod volume). n.a., not applicable
[c]: χ_{best} is the lowest χ value obtained for a free atom model from the *ab initio* shape determinations. n.a., not applicable.
[d]: χ values for the fit between this model and the SAXS data are 4.89 (GppNHp data) and 6.65 (GDP•AlF_x data).
[e]: χ values for the fit between this model and the SAXS data are 2.56 (GppNHp data) and 2.95 (GDP•AlF_x data).

the two crystallographic, GDP-bound dimers are very similar to the corresponding region of the experimental curves, consistent with common folds of the domains and similar G domain dimerization. Yet, in general the crystalline conformations represent inaccurate models for GTP-bound atlastin based on the overall fit (Table 2.3. and Figure 2.8.A). Modeling of the SAXS data can yield low-resolution reconstructions representing the shape of a protein. A similar approach has been described recently for near-full-length dynamin revealing the overall organization of the protein in solution (7). Unbiased models for the solution states of GTP-bound and the transition state atlastin-1 were obtained by using a free-atom, simulated annealing approach with the respective *P(r)* functions as the target (34). For each state, 20 models were computed, averaged, and filtered to yield a consensus envelope. The shape reconstructions for

Figure 2.8. SAXS data. (A) P(r) for the form 1 dimer (gray, solid) and the form 2 dimer (black, dashed) were calculated by using the respective crystal structures. P(r) based on experimental scattering data for GppNHp-bound and GDP•AlF_x-bound atlastin-1 (residues 1–446) are shown in green and orange, respectively. (B) Kratky plots calculated based on intensity data from apo (red), GDP added (purple), GppNHp-bound (green), and GDP•AlF_x-bound (orange) atlastin-1. The SAXS data for the nucleotide-free state of atlastin-1 indicated an unfolded or flexible component evident in Kratky plots, which was suppressed upon binding of GDP. Both flexibility within the G domain and a dislodged middle domain in the absence of nucleotide may contribute to these differences. (C) P(r) functions of monomeric atlastin-1 species. The apo-state (red) and atlastin-1 incubated in GDP (purple) are shown. Theoretical P(r) functions for the form 1 protomer (gray, solid) and form 2 protomer (black, dashed) are shown in both plots. The crystallographic conformations of the monomers are inaccurate models for the solution state. (D) SAXS-based shape reconstructions for monomeric solution states of atlastin-1. Models were calculated by using the P(r) function as the target. The monomeric crystal structure protomers (form 1 and 2) were docked in the models as a reference and are shown as a cartoon presentation. Modeling the SAXS data from apo-atlastin-1 or the GDP-bound protein revealed a large upper lobe that accommodates a G domain. A stalk-like extension resembles the middle domain. In the presence of GDP, the overall solution conformation of the G domain appears more compressed and globular. Both the nucleotide-unbound and GDP-bound solution models could accommodate either crystal structure protomer. Relatively high % values for the comparison between the crystalline states and the solution scattering data (ranging between 5.51–8.10) suggest that the exact solution conformation may be different from the crystallographic states. Given this ambiguity, we refrained from modeling the solution states beyond this analysis.

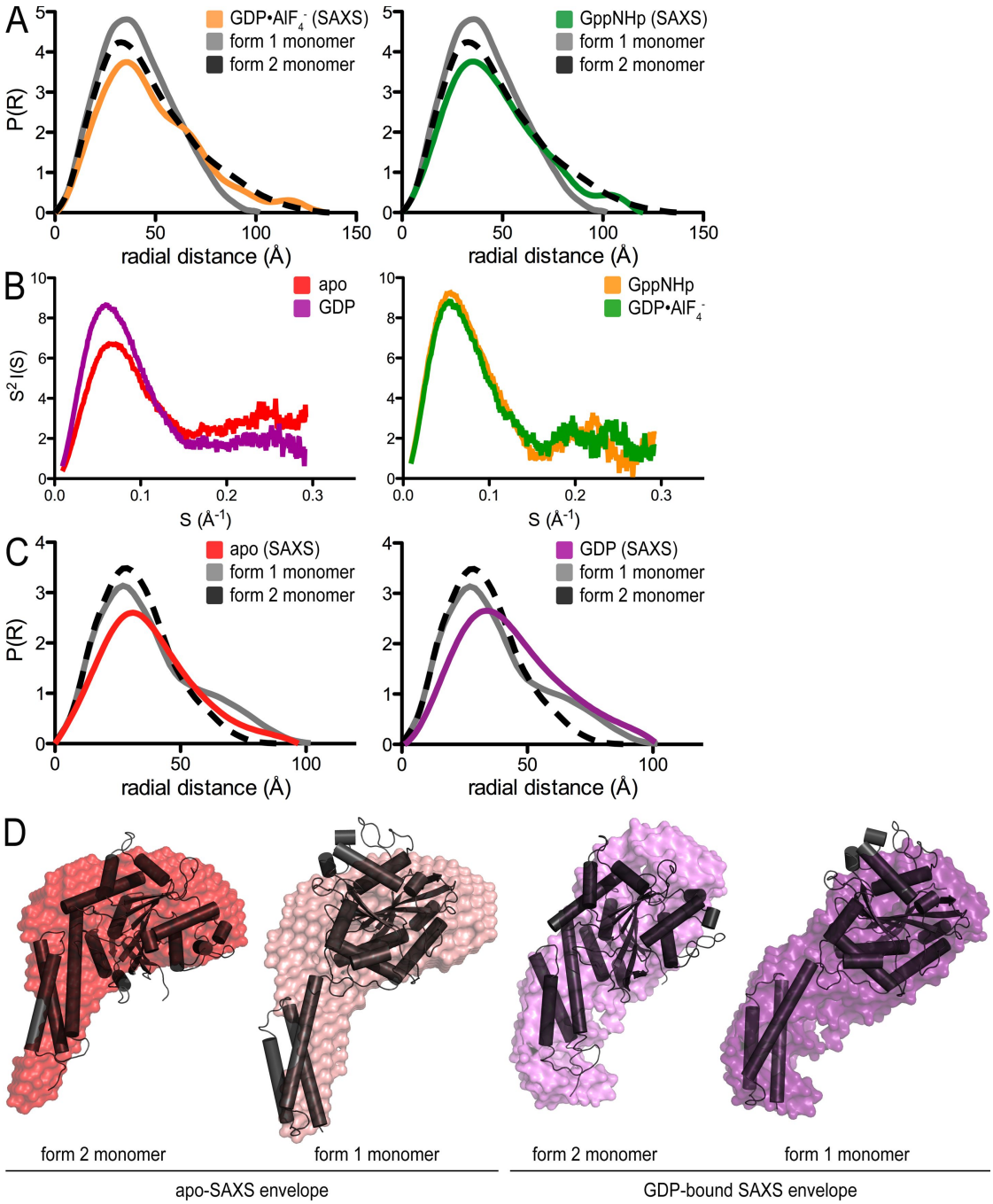
A
GDP•AlF4- (SAXS)
form 1 monomer
form 2 monomer
P(R)
radial distance (Å)
GppNHp (SAXS)
form 1 monomer
form 2 monomer
radial distance (Å)
B
apo
GDP
S2I(S)
S (Å-1)
GppNHp
GDP•AlF4-
S (Å-1)
C
apo (SAXS)
form 1 monomer
form 2 monomer
P(R)
radial distance (Å)
GDP (SAXS)
form 1 monomer
form 2 monomer
radial distance (Å)
D
form 2 monomer
form 1 monomer
apo-SAXS envelope
form 2 monomer
form 1 monomer
GDP-bound SAXS envelope

atlastin-1 bound to GppNHp or GDP•AlF_x are consistent with a central G domain dimer carrying lateral middle domains. Despite the inaccurate fits between the SAXS data and crystallographic models (Table 2.3.), the overall conformation of the dimeric solution states has some resemblance with the extended conformation of the dimeric, form 2 crystal structure, in which the middle domains fold back onto their respective G domains and point in opposite directions (Figure 2.7.B). The G domain dimer fits the mass observed at the center of both models, placing the middle domains roughly into the skinnier density at the distal tips. Subtle differences in the SAXS-based models for atlastin-1 bound to GppNHp and GDP•AlF_x concern these distal regions, extending radially from the center of the G domain dimer, but a more exact prediction of the structural changes is likely beyond the accuracy of the method.

In summary, the nucleotide-dependent oligomerization via central G domain dimers indicates related mechanisms between atlastin, GBP, dynamin, and other large G proteins that are activated by nucleotide-dependent dimerization (2). As described in the next section, further corroboration comes from several atlastin-1 mutants associated with the neurodegenerative disorder HSP, many of which display defects in GTP-dependent dimerization when introduced into the cytosolic domain, suggesting that disruption of this mechanism contributes to the pathogenesis in HSP.

Structure-Based Mapping and Characterization of HSP-Associated Mutations of Atlastin-1.

To date, 28 atlastin-1 missense mutants associated with cases of HSP have been identified within the construct studied here (24, 25). Within the primary

sequence, the mutations are located in the second half of the G domain and the middle domain (Figure 2.9.A). By mapping the mutations onto the three-dimensional structures determined here, HSP-associated mutants cluster in the regions of the protein that vary most between the two crystal forms, including the putative dimer interface, the nucleotide-binding pocket, and the region of the intramolecular rigid body rotation (Figures 2.4. and 2.9.).

For a functional characterization, we introduced the HSP-associated, single-point mutations into the soluble, cytoplasmic domain of atlastin-1 used in this study. The majority of the mutants (16 out of 28) expressed and purified indistinguishably compared to the wild-type protein and elute from the gel filtration column as a single, monodisperse peak (Table 2.2.). Those mutants that did not express in our system likely introduce significant folding defects (black spheres, Figure 2.9.). In contrast, the soluble mutants exhibit similar thermal melting temperatures that are comparable to that of the wild-type protein (Table 2.2. and Figure 2.10.C), indicating that folding defects, if any, are local with no apparent effect on protein stability.

Half of the soluble mutants exhibited dimerization behavior indistinguishable from the wild-type protein (Figure 2.10.A and Table 2.2.). In contrast, several mutant proteins displayed defects in dimerization (Figures 2.10.A, 2.11., and 2.12.). These include $L^{157}W$, $Q^{191}R$, $Y^{196}C$, $R^{217}Q$, $H^{247}R$, $Y^{336}H$, and $M^{408}V/T$ (orange and red residues, Figure 2.9.). $R^{217}Q$, the only mutation located in the nucleotide-binding site, displays the most drastic effect. R^{217} is the first residue in the RD motif and interacts with the nucleotide's guanine base (Figure 2.1.B; red residue, Figure 2.9.) (41). The protein remains monomeric irrespective of the presence of nucleotide and is defective

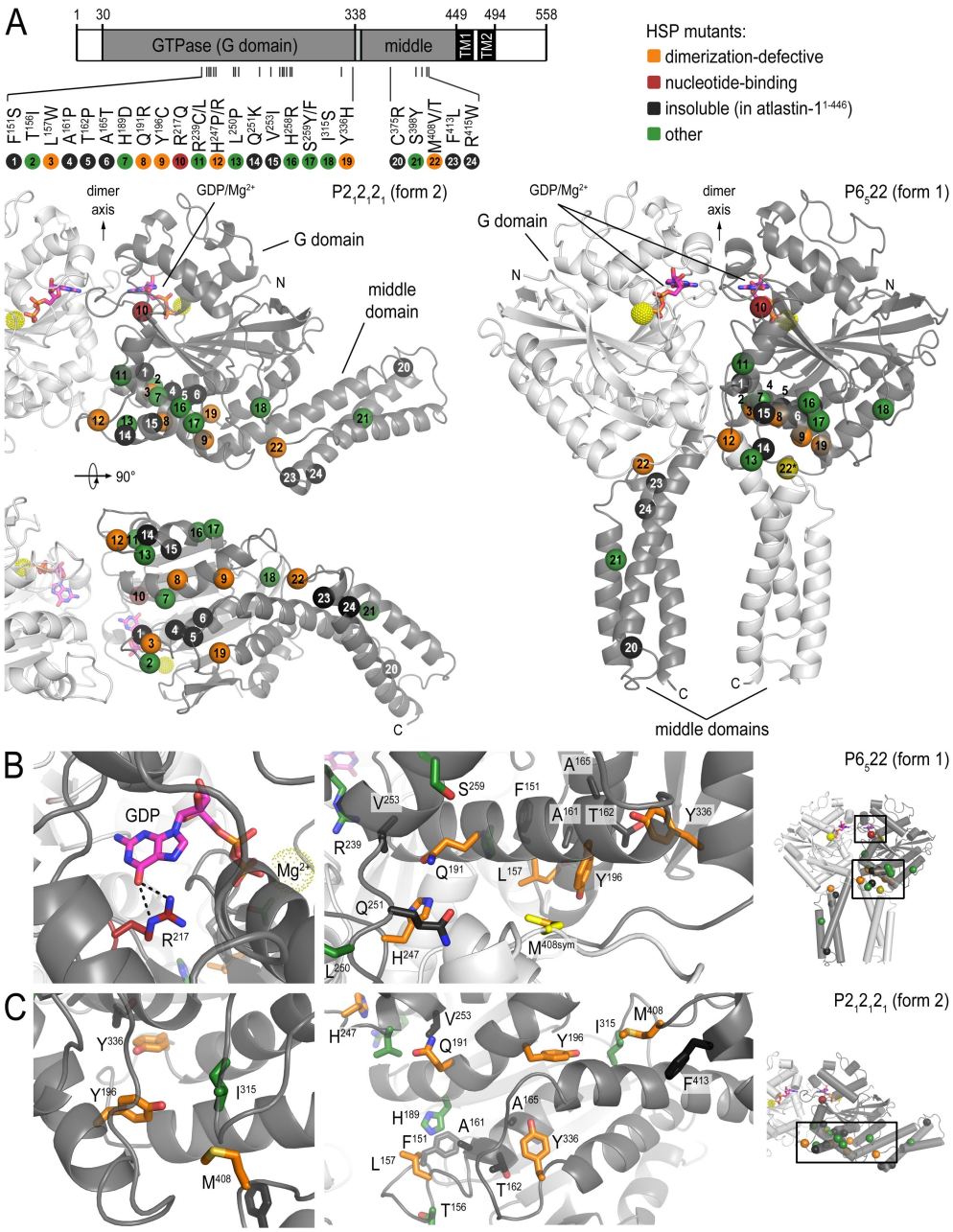

Figure 2.9. Mapping of hereditary spastic paraplegia (HSP) mutant residues onto the primary and tertiary structure of atlastin-1. (A) Overview of the position of HSP mutations. The atlastin-1 domain organization is shown as in Fig. 1, with the locations of all missense mutations that fall into the crystallized construct being marked. HSP mutations were mapped onto the tertiary structure of atlastin-1 (form 1, Right; form 2, Left). The two protomers of each dimer are colored in light and dark gray, respectively. Positions of missense mutations associated with HSP are shown as spheres and color-coded according to their biochemical properties. Position of the dimerization-defective mutants in the form 1 (B) and form 2 (C) dimer models for atlastin-1. Detailed views of several HSP mutation sites in atlastin-1 that show defects in nucleotide binding and/or oligomerization are shown. Color-coding is shown as in A.

with regard to nucleotide binding and GTPase activity (Figures 2.3., 2.11. and 2.12.), consistent with its direct role in nucleotide coordination. The oligomerization propensities of the mutants $T^{157}W$, $Q^{191}R$, $Y^{196}C$, $H^{247}R$, $Y^{336}H$, and $M^{408}V/T$ are peculiar in that they exhibit dimer formation similar to wild-type protein upon binding of the transition state analog, but show a significant fraction of monomeric species upon incubation with GppNHp (Figures 2.11. and 2.12.). Although they show variable degrees of GTPase activity and no direct correlation between GppNHp-dependent dimer formation and activity, they coalesce at or close to a surface on the G domain that is part of the interdomain interfaces in both crystal forms (Figures 2.9. and 2.11.). Although the location of the mutations in the crystal structures and type of amino acid change do not allow for any obvious predictions regarding their effect on oligomerization or enzymatic activity, the defective dimerization upon GppNHp incubation and the spatial proximity suggest a common mode of action.

Taken together, the subset of atlastin-1 mutations with reduced dimerization propensity further support a dimer-dependent molecular mechanism for atlastin function and reveal a prominent mode of action for genetic alterations that contribute to HSP pathogenesis. Despite the measurable reduction in dimer formation upon incubation with GppNHp, the transition state dimers appear to be less affected by the mutations (with the exception of the nucleotide-binding-deficient mutant $R^{217}Q$), which may explain why changes in GTPase activity are less pronounced. Alternatively, nucleotide binding and dimerization may not be necessarily interdependent and could potentially constitute distinct mechanisms underlying HSP.

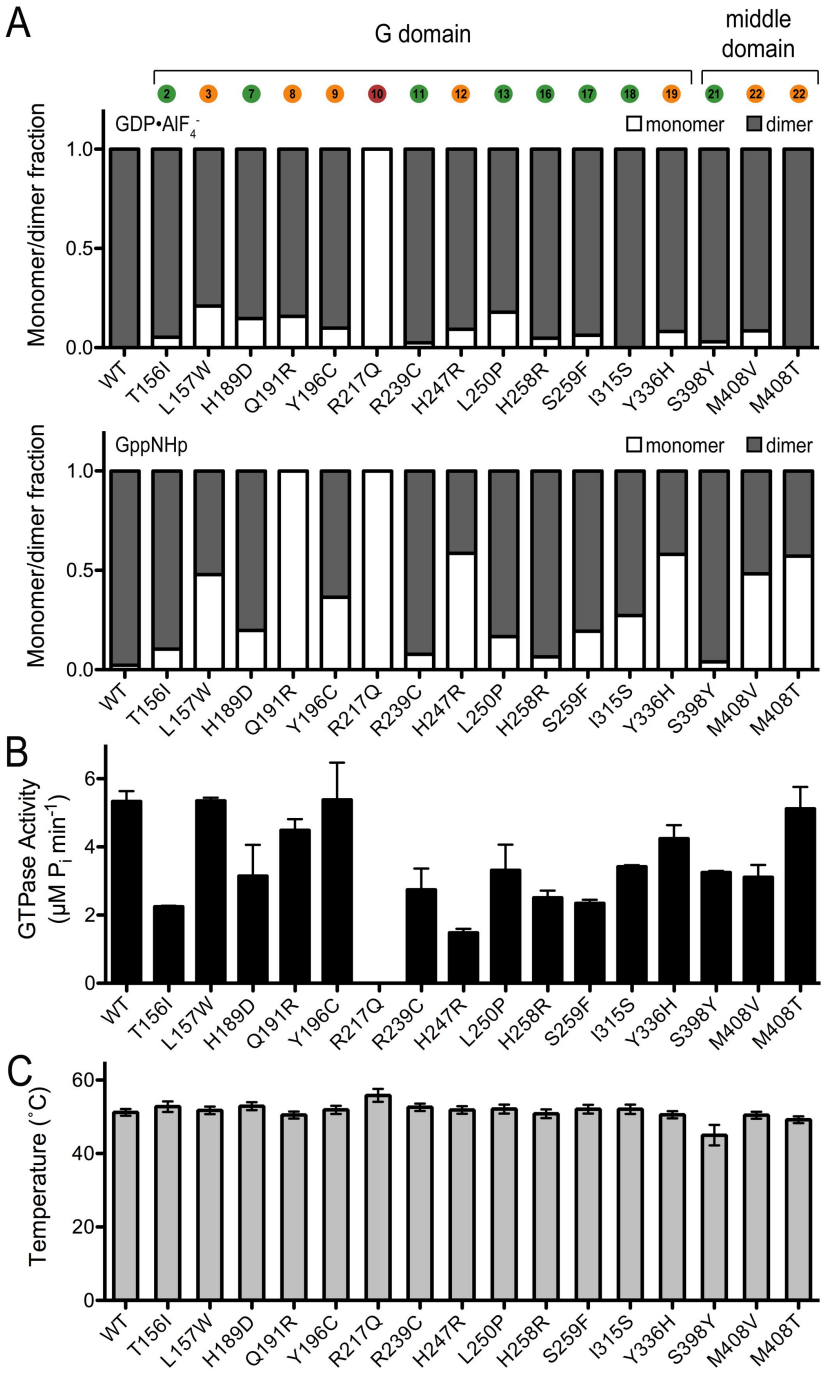

Figure 2.10. Solution properties of HSP-associated mutations introduced in the cytoplasmic domain of atlastin-1. (A) Nucleotide-dependent dimerization of HSP-associated atlastin-1 mutants. Molecular weight distributions for GppNHp- or AlF_x-bound atlastin-1 variants (residues 1–446) were determined by static multiangle light scattering. Errors correspond to calculated errors in the fitting function parameters. (B) GTPase activity. GTPase activity was determined by measuring the production of inorganic phosphate upon GTP hydrolysis (see Material and Methods for details). (C) Protein stability was determined based on measurements of the melting temperature by circular dichroism spectroscopy.

In addition, other mutants showed only modestly decreased GTPase activity and near wild-type dimerization (green spheres, Figures 2.9. and 2.10.; Table 2.2.), indicating that they confer defects in some other, yet unknown aspect.

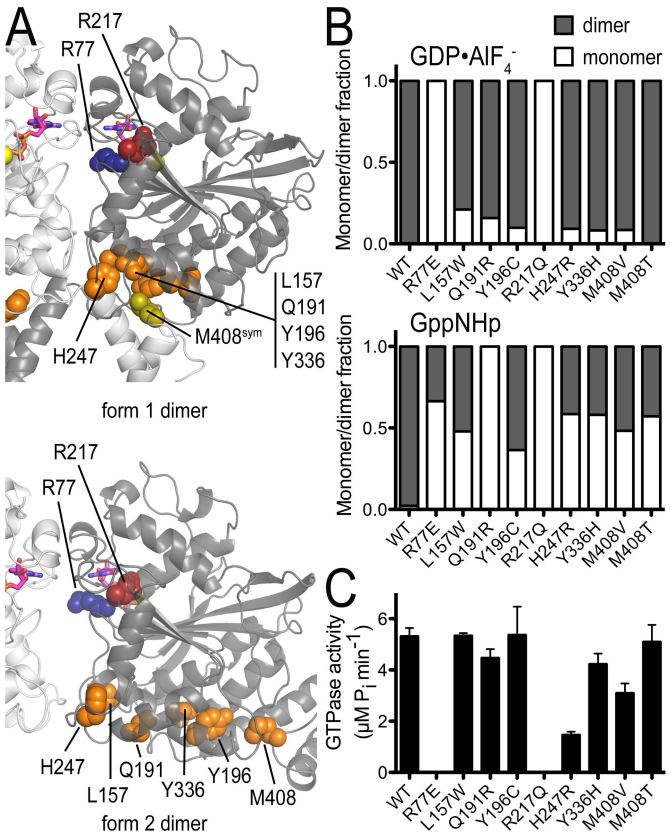

Figure 2.11. Characterization of HSP-associated mutations in atlastin-1. (A) Mapping of HSP mutant residues that affect dimerization (red and orange) onto the crystal structures of atlastin-1. Protomers are colored in light and dark gray. R^{217} (red) is located in the nucleotide-binding pocket. Dimer interface mutant R^{77} (blue) is not associated with HSP but was chosen based on the crystallographic dimer interface. (B) Nucleotide-dependent dimerization of HSP-associated atlastin-1 mutants. Molecular weight distributions for GppNHp- or AlF_x -bound atlastin-1 variants (residues 1–446) were determined by static multiangle light scattering. Errors correspond to calculated errors in the fitting function parameters. (C) GTPase activity. GTPase activity was determined by measuring the production of inorganic phosphate upon GTP hydrolysis.

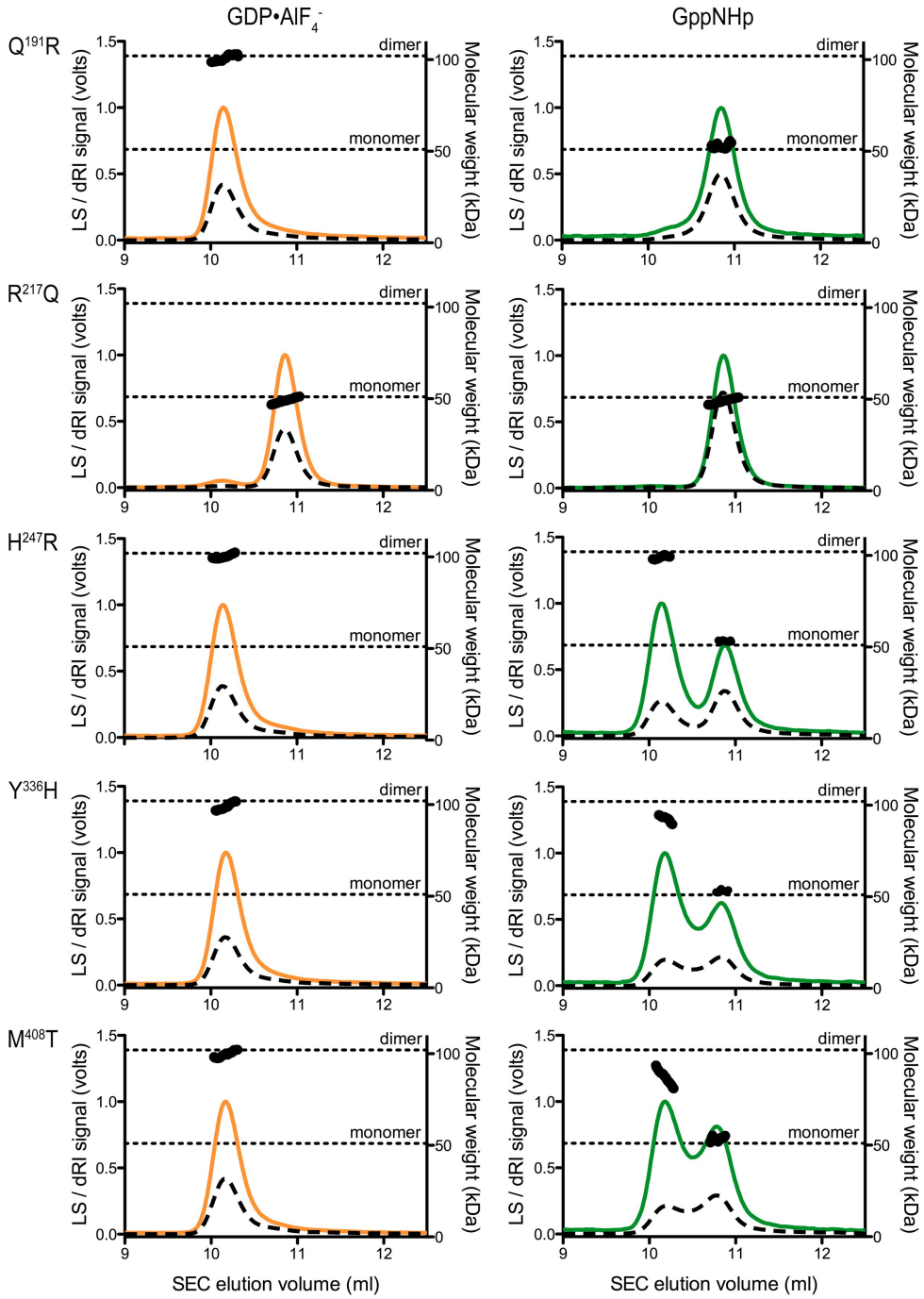

Figure 2.12. SEC-MALS data for selected HSP mutants. SEC-MALS of atlastin-1 $Q^{191}R$, $R^{217}Q$, $H^{247}R$, $Y^{336}H$, and $M^{408}T$ bound to GDP•AlF_x (Left) or GppNHp (Right). Plotted on the left Y axis, the signal from the 90°-scattering detector and refractive index detector is shown in a solid colored line and a black dashed line, respectively. On the right Y axis, average molecular weight as calculated every second across the protein elution peak is shown as black circles. Theoretical molecular weights based on primary sequence for the monomer and dimer are indicated as horizontal, dashed lines. Proteins (20 μM) were incubated with nucleotides (2 mM) prior to SEC-MALS analysis in a mobile phase lacking nucleotides.

CONCLUSIONS

In summary, the structural and functional analyses revealed a mechanistic conservation between atlastin and other dynamin superfamily proteins with regard to overall architecture, in particular the position of the respective stalk-like protrusions relative to their G domains, and nucleotide-dependent homodimerization. The apparent differences in the solution structures in different nucleotide-bound states, the distinct conformations observed in the two different crystal forms, and the unique behavior of several HSP-associated mutants lead one to speculate that the overall structure and function of atlastin is coupled to its GTP hydrolysis cycle. The indication that GppNHp and GDP•AlF_x induce distinct conformational and functional states is analogous to both Gα subunits and small GTPases where these differences are attributed to the GTP-bound ground state and transition state for GTP hydrolysis (42, 43).

The antiparallel orientation of the middle domains in one of the crystal structures (form 2) and the elongated, dimeric solution states suggests that atlastin monomers from opposite membranes may engage in this oligomerization. GTP hydrolysis and/or the transition state may trigger a conformational change in atlastin, facilitating the formation of three-way junctions and membrane fusion (14, 15). The association with highly curved membranes and interactions with other proteins will further contribute to these processes (14, 20). Such interactions could trigger allosteric changes across the middle domain modulating atlastin's GTPase activity, similar to the autoregulatory role of the PH domain in dynamin (7). Although we have not observed the second crystalline conformation (form 1) in solution, we speculate it may

be relevant in the native environment of the protein and could represent an end state (and/or inhibited, GDP-bound state).

Many mutations occurring in HSP patients impair oligomerization of atlastin, nucleotide hydrolysis, or both. Given the minor impact of several mutants on protein stability, it is likely that they retain the ability to interact with some (if not all) binding partners in the cell. Mixed dimer formation and engagement in dysfunctional complexes may affect the wild-type alleles, providing a rationale for the dominant phenotype of the mutations. Although many mutations coalesce in the region between the nucleotide-binding site and the intramolecular domain interface, their exact pathological mechanism remains elusive. One hypothesis awaiting further analysis is that these alterations may perturb communication between the G domain and middle domain during the nucleotide-dependent, functional cycle.

Other mutations associated with HSP that occur in regions outside of the crystallized fragment would be predicted to affect atlastin's stability in the membrane as well as its interactions with the reticulon and DP1 families (e.g., mutations near or in the transmembrane domains; $Y^{459}C$, $G^{469}A$, $G^{482}V$, $R^{495}W$) (14, 15). Furthermore, there are several mutations within the C-terminal domain of atlastin, including missense or nonsense mutations, that truncate the C terminus (A^{492}fsX522, E^{502}fsX522, I^{507}fsX522, $S^{519}N$), which would be expected to affect atlastin's interactions with other binding partners, such as spastin, as has been shown previously for I^{507}fsX522 (21).

REFERENCES

1. Praefcke GJK, McMahon HT (2004) The dynamin superfamily: universal membrane tubulation and fission molecules? *Nat Rev Mol Cell Biol* 5:133–147.

2. Gasper R, Meyer S, Gotthardt K, Sirajuddin M, Wittinghofer A (2009) It takes two to tango: regulation of G proteins by dimerization. *Nat Rev Mol Cell Biol* 10:423–429.

3. Prakash B, Praefcke GJ, Renault L, Wittinghofer A, Herrmann C (2000) Structure of human guanylate-binding protein 1 representing a unique class of GTP-binding proteins. *Nature* 403:567–571.

4. Chappie JS, Acharya S, Leonard M, Schmid SL, Dyda F (2010) G domain dimerization controls dynamin's assembly-stimulated GTPase activity. *Nature*.

5. Mettlen M, Pucadyil T, Ramachandran R, Schmid SL (2009) Dissecting dynamin's role in clathrin-mediated endocytosis. *Biochem Soc Trans* 37:1022.

6. Zhang P, Hinshaw J (2001) Three-dimensional reconstruction of dynamin in the constricted state. *Nat Cell Biol* 3:922–926.

7. Kenniston JA, Lemmon MA (2010) Dynamin GTPase regulation is altered by PH domain mutations found in centronuclear myopathy patients. *EMBO J*.

8. Chappie JS et al. (2009) An intramolecular signaling element that modulates dynamin function in vitro and in vivo. *Mol Biol Cell* 20:3561–3571.

9. Bashkirov PV et al. (2008) GTPase Cycle of Dynamin Is Coupled to Membrane Squeeze and Release, Leading to Spontaneous Fission. *Cell* 135:1276–1286.

10. Tuma PL, Collins CA (1994) Activation of dynamin GTPase is a result of positive cooperativity. *J Biol Chem* 269:30842–30847.

11. Warnock DE, Hinshaw JE, Schmid SL (1996) Dynamin self-assembly stimulates its GTPase activity. *J Biol Chem* 271:22310–22314.

12. Gao S et al. (2010) Structural basis of oligomerization in the stalk region of dynamin-like MxA. *Nature* 465:502–506.

13. Zhao X et al. (2001) Mutations in a newly identified GTPase gene cause autosomal dominant hereditary spastic paraplegia. *Nat Genet* 29:326–331.

14. Hu J et al. (2009) A Class of Dynamin-like GTPases Involved in the Generation of the Tubular ER Network. *Cell* 138:549–561.

15. Orso G et al. (2009) Homotypic fusion of ER membranes requires the dynamin-

like GTPase Atlastin. *Nature*.

16. Namekawa M et al. (2007) Mutations in the SPG3A gene encoding the GTPase atlastin interfere with vesicle trafficking in the ER/Golgi interface and Golgi morphogenesis. *Mol Cell Neurosci* 35:1–13.

17. Muriel M et al. (2009) Atlastin-1, the dynamin-like GTPase responsible for spastic paraplegia SPG3A, remodels lipid membranes and may form tubules and vesicles in the endoplasmic reticulum. *Journal of Neurochemistry*.

18. Rismanchi N, Soderblom C, Stadler J, Zhu P-P, Blackstone C (2008) Atlastin GTPases are required for Golgi apparatus and ER morphogenesis. *Hum Mol Genet* 17:1591–1604.

19. Zhu P-P et al. (2003) Cellular Localization, Oligomerization, and Membrane Association of the Hereditary Spastic Paraplegia 3A (SPG3A) Protein Atlastin. *Journal of Biological Chemistry* 278:49063–49071.

20. Park SH, Zhu P-P, Parker RL, Blackstone C (2010) Hereditary spastic paraplegia proteins REEP1, spastin, and atlastin-1 coordinate microtubule interactions with the tubular ER network. *The Journal of clinical investigation*.

21. Evans K et al. (2006) Interaction of two hereditary spastic paraplegia gene products, spastin and atlastin, suggests a common pathway for axonal maintenance. *Proc Natl Acad Sci USA* 103:10666–10671.

22. Sanderson CM et al. (2006) Spastin and atlastin, two proteins mutated in autosomal-dominant hereditary spastic paraplegia, are binding partners. *Hum Mol Genet* 15:307–318.

23. Fink JK (2006) Hereditary spastic paraplegia. *Curr Neurol Neurosci Rep* 6:65–76.

24. Smith BN et al. (2009) Four novel SPG3A/atlastin mutations identified in autosomal dominant hereditary spastic paraplegia kindreds with intra-familial variability in age of onset and complex phenotype. *Clinical Genetics* 75:485–489.

25. Mccorquodale Iii D et al. (2010) Mutation screening of spastin, atlastin, and REEP1 in hereditary spastic paraplegia. *Clinical Genetics*.

26. Zhu P-P, Soderblom C, Tao-Cheng J-H, Stadler J, Blackstone C (2006) SPG3A protein atlastin-1 is enriched in growth cones and promotes axon elongation during neuronal development. *Hum Mol Genet* 15:1343–1353.

27. Marley J, Lu M, Bracken C (2001) A method for efficient isotopic labeling of recombinant proteins. *J Biomol NMR* 20:71–75.

28. Otwinowski Z, Minor W (1997) Processing of X-ray diffraction data. *Meth Enzymol* 276:307–326.

29. Adams PD et al. (2002) PHENIX: building new software for automated crystallographic structure determination. *Acta Cryst (2002) D58, 1948-1954 [doi:101107/S0907444902016657]*:1–7.

30. Emsley P, Cowtan K (2004) Coot: model-building tools for molecular graphics. *Acta Cryst (2004) D60, 2126-2132 [doi:101107/S0907444904019158]*:1–7.

31. Petoukhov MV, Konarev PV, Kikhney AG, Svergun DI (2007) ATSAS 2.1-towards automated and web-supported small-angle scattering data analysis. *Applied Crystallography*.

32. Svergun D, Barberato C, Koch MHJ (1995) CRYSOL - a Program to Evaluate X-ray Solution Scattering of Biological Macromolecules from Atomic Coordinates. *J Appl Cryst (1995) 28, 768-773 [doi:101107/S0021889895007047]*:1–6.

33. Svergun DI (1992) Determination of the regularization parameter in indirect-transform methods using perceptual criteria. *Journal of Applied Crystallography* 25:495–503.

34. Svergun DI, Petoukhov MV, Koch MH (2001) Determination of domain structure of proteins from X-ray solution scattering. *Biophys J* 80:2946–2953.

35. Volkov V, Svergun D (2003) Uniqueness of ab initio shape determination in small-angle scattering. *Journal of Applied Crystallography* 36:860–864.

36. Kozin M, Svergun D (2001) Automated matching of high-and low-resolution structural models. *Journal of Applied Crystallography* 34:33–41.

37. Ghosh A, Praefcke GJK, Renault L, Wittinghofer A, Herrmann C (2006) How guanylate-binding proteins achieve assembly-stimulated processive cleavage of GTP to GMP. *Nature* 440:101–104.

38. Low H, Löwe J (2006) A bacterial dynamin-like protein. *Nature* 444:766–769.

39. Putnam CD, Hammel M, Hura GL, Tainer JA (2007) X-ray solution scattering (SAXS) combined with crystallography and computation: defining accurate macromolecular structures, conformations and assemblies in solution. *Quarterly reviews of biophysics* 40.

40. Koch MHJ, Vachette P, Svergun DI (2003) Small-angle scattering: a view on the properties, structures and structural changes of biological macromolecules in solution. *Quarterly reviews of biophysics* 36:147–227.

41. Praefcke GJK et al. (2004) Identification of residues in the human guanylate-binding protein 1 critical for nucleotide binding and cooperative GTP hydrolysis. *J Mol Biol* 344:257–269.

42. Sprang S (2000) Conformational Display: A role for switch polymorphism in the superfamily of regulatory GTPases. *Science's STKE* 2000.

43. Oldham W, E Hamm H (2006) Structural basis of function in heterotrimeric G proteins. *Quarterly reviews of biophysics* 39:117–166.

CHAPTER 3

STRUCTURAL BASIS FOR THE CONFORMATIONAL SWITCHING AND GTP LOADING OF THE LARGE G PROTEIN ATLASTIN[§]

ABSTRACT

Atlastin, a member of the dynamin superfamily, is known to catalyze homotypic membrane fusion in the smooth endoplasmic reticulum (ER). Recent studies of atlastin have elucidated key features about its structure and function; however, several mechanistic details, including the catalytic mechanism and GTP hydrolysis-driven conformational changes, are yet to be determined. Here, we present the crystal structures of atlastin-1 bound to GDP•AlF_4^- and GppNHp, uncovering an intramolecular arginine finger that stimulates GTP hydrolysis when correctly oriented through rearrangements within the G domain. Utilizing Förster Resonance Energy Transfer, we describe nucleotide binding and hydrolysis-driven conformational changes in atlastin and their sequence. Furthermore, we discovered a nucleotide exchange mechanism that is intrinsic to atlastin's N-terminal domains. Our results indicate that the cytoplasmic domain of atlastin acts as a tether and homotypic interactions are timed by GTP binding and hydrolysis. Perturbation of these mechanisms may be implicated in a group of atlastin-associated hereditary neurodegenerative diseases.

[§] The following sections are reproduced from: Byrnes, L.J., Singh, A., Szeto, K., Benvin, N.M., O'Donnell, J.P., Zipfel, W.R., and Sondermann, H. 2013. Structural basis for the conformational switching and GTP loading of the large G protein atlastin. EMBO J. **32** pp369-384, doi: 10.1038/emboj.2012.353, with modifications to conform to the required format. LJB and HS conceived the project. LJB, AS, KS, WRZ, and HS designed the experiments. LJB, AS, KS, NMB, and HS performed the experiments. LJB, AS, KS, JPO, WRZ, and HS analyzed the data. LJB and HS wrote the paper.

INTRODUCTION

Hereditary Spastic Paraplegia (HSP) is a progressive spastic weakness of the lower extremities due to the degeneration of axons in corticospinal motor neurons at their distal ends (1, 2). While it is a rare disease, affecting 2–7.4 in 100 000 people (1, 3-5), extensive genetic studies have revealed several hot spots associated with the disease, with >50% of cases caused by mutations in just three loci: Spastin-1, REEP-1, and atlastin-1 (5, 6). Atlastin-1/SPG3A mutations account for ~10% of autosomal dominant HSP cases; however, this locus is the primary site for mutations in children affected with the disease (7). Mutations in atlastin-1 have also been detected in patients suffering from hereditary sensory neuropathy (HSN), a related neurodegenerative disorder affecting lower motor neurons (8).

Atlastin-1 is found in neurons at the cis-Golgi, endoplasmic reticulum (ER), and axon growth cones, where it is part of a complex containing spastin, reticulons, and REEP proteins (9-12). Atlastins and reticulons are involved in generating and maintaining the tubular ER network (11-15), where atlastin promotes homotypic fusion of membranes, generating three-way junctions (11, 15). On a molecular level, atlastins are related to large G proteins such as dynamin, MxA, GBP1, and mitofusin, many of which are involved in membrane fission or fusion (16). Structural studies on near full-length dynamin, MxA, and GBP1 revealed remarkable similarities to atlastin regarding the molecular architecture of the G proteins (17-25). All the proteins of this family contain a globular G domain followed by an α-helical, stalk-like middle domain (Figure 3.1.A). For dynamin, the prototypical member of this family, GTP hydrolysis is coupled to conformational changes that alter the position of the stalk-like

domain (called the bundle signaling element or BSE) relative to the G domain dimer (22-24), yet full activation requires a membrane-dependent, higher order assembly (22-24, 26-32).

A prominent feature of several dynamin superfamily proteins is the oligomerization-dependent activation of their GTPase activity, which is in contrast to small GTPases that rely on the action of heterologous GTPase activating proteins (15, 33-35). Recent studies yielded the first crystal structures of atlastin (forms 1 and 2 with a 'disengaged' and 'engaged' middle domain, respectively, relative to their G domain; Figure 3.1.B), revealing two dimeric conformations that presumably represent pre- and post-fusion states and hint at an overall conserved mechanism (20, 21). These studies also suggested a model by which GTP binding tethers two opposing membranes via G domain dimerization, with GTP hydrolysis being coupled to intramolecular conformational changes that drive membrane fusion (36). However, the structures depict only GDP-bound states, hence, the exact catalytic mechanism for atlastin and the concurrent conformational switching upon GTP hydrolysis remained unknown. It has also been established that the middle domain is required for dimerization and GTPase activity (37-39), the reason for which is not obvious from the initial models. In addition, a recent report demonstrated, using single-particle electron microscopy, that atlastin-2 bound to the GTP-mimic GppNHp adopts both the presumed pre- and post-fusion conformations, the latter of which depends on an intramolecular salt bridge between the middle domain and the adjacent linker (37). The authors argued that GTP hydrolysis might not be the direct trigger for conformational changes leading to fusion. While this presents an apparent

contradiction to earlier studies (20, 21), we now present an alternative model based on novel crystal structures and approaches that report on dynamic changes and kinetics within the cytoplasmic, N-terminal module of human atlastin-1. Our studies address several fundamental questions regarding the intrinsic regulation of atlastin with relevance to the mechanism of membrane fusion, in particular: (1) the molecular basis for GTP hydrolysis; (2) the conformational changes and their timing along atlastin's GTPase cycle; and (3) the surprising discovery of an intrinsic, middle domain-mediated mechanism for GTP loading in atlastin.

MATERIALS AND METHODS

Protein expression and purification

The cytoplasmic domain (residues 1-446), G domain (1-339), middle domain (340-446), truncated middle domain (1-366), and C-terminal ECFP/EYFP fusions (atlastin1 1-446 followed by a short linker containing amino acid sequence GSTSTG followed by either ECFP or EYFP) of human atlastin-1 were amplified by standard PCR and cloned into a modified pET28a expression plasmid (Novagen) yielding N-terminally hexahistidine-tagged SUMO fusion proteins. The hexahistidine-tagged SUMO-moiety was cleavable using the protease Ulp-1 from *S. cerevisiae*. The cytoplasmic domain (1-446) used for crystallization of wild-type atlastin was cloned into pET21, yielding C-terminally hexahistidine-tagged protein, which was not cleaved during purification.

Proteins were overexpressed in *E. coli* BL21 (DE3) (Novagen) or T7 Crystal Express (NEB) cells, respectively. For the expression of native proteins, cells were

grown in Terrific Broth (TB) media supplemented with 50 μg/ml kanamycin (for expression from pET28) or 100 μg/ml ampicillin (for expression from pET21) at 37°C. At an optical density corresponding to an absorbance of 0.8-1.0 at 600 nm (OD_{600}), the temperature was reduced to 18°C, and protein production was induced with 0.5 mM IPTG. After 16 hours, cells were harvested by centrifugation, resuspended in NiNTA buffer A (25 mM Tris-HCl, pH 8.5, 500 mM NaCl and 20 mM imidazole), and flash-frozen in liquid nitrogen.

After cell lysis by sonication and removal of cell debris by centrifugation, clear lysates were loaded onto NiNTA Superflow (Qiagen) equilibrated in NiNTA buffer A. The resin was washed with 20 column volumes of NiNTA buffer A, and proteins were eluted three times with 2 column volumes of NiNTA buffer A supplemented with 500 mM imidazole. Proteins were buffer exchanged into desalting buffer (25 mM Tris-HCl, pH 7.5, 400 mM NaCl, 5mM β-mercaptoethanol), with proteins expressed in pET21 constructs immediately subjected to size exclusion chromatography. In the case of proteins expressed with a SUMO moiety, affinity tags were removed by incubation with the yeast protease Ulp-1 at 4°C overnight. Cleaved proteins were collected in the flow-through during NiNTA affinity chromatography, and were subjected to size exclusion chromatography on a Superdex 200 column (GE Healthcare) equilibrated in gel filtration buffer (25 mM Tris-HCl, pH 7.5, 100 mM NaCl). Proteins were concentrated on a Centricon ultrafiltration device (10 kDa cutoff; Millipore) to a final concentration of approximately 0.5-1 mM. Protein aliquots were flash frozen in liquid nitrogen and stored at -80°C.

Site-directed mutagenesis was carried out using Quikchange (Agilent) following the manufacturer's instructions, followed by validation through DNA sequencing.

Crystallization, data collection, and structure solution

Crystals were obtained by sitting drop vapor diffusion mixing equal volumes of protein (10–30mg/ml) and reservoir solution followed by incubation at 20°C. Initial crystals were obtained using atlastin-1 protein in gel filtration buffer in the presence of 2 mM GppNHp (Sigma) and 4 mM $MgCl_2$. In the case of GDP•AlF_4^-, crystals were obtained in the presence of 2 mM GDP (Sigma), 4 mM $MgCl_2$, 2 mM EGTA, 2 mM $AlCl_2$, and 20 mM NaF. Rod-shaped crystals belonging to space group $P2_12_12$ (atlastin-$1^{1–446}$-N^{440}T) grew in reservoir solution containing 0.2M lithium citrate tribasic tetrahydrate and 20% PEG-3350 (for both GppNHp and GDP•AlF_4^- crystals). For cryo-protection, crystals were soaked in reservoir solution supplemented with 25% glycerol. For proteins crystallizing in space group $P2_12_12_1$ (atlastin-$1^{1–446}$-Chis), the reservoir solution contained 0.1 M imidazole, pH 7.0 and 20% v/v Jeffamine ED-2001, pH 7.0 (GppNHp) or 0.2 M ammonium phosphate dibasic and 20% PEG-3350 (GDP•AlF_4^-). Crystals were cryo-protected by soaking in the crystallization solutions supplemented with 20% xylitol. Cryo-preserved crystals were flash-frozen and stored in liquid nitrogen. Data were collected on frozen crystals at 100 K.

Data reduction was carried out with the software package HKL2000 (40). Phases were obtained either by Single-wavelength Anomalous Dispersion (SAD) or Molecular Replacement (MR) methods by using the software package PHENIX (41)

with the isolated G and middle domains of atlastin-1 as separate search models for MR. Refinement in PHENIX (41) and COOT (42) yielded the final models. Data collection and refinement statistics are summarized in Table 3.1. Illustrations were made in Pymol (43).

Size-exclusion chromatography-coupled multi-angle light scattering

Purified protein (<2 mg/ml or 40 mM, injected concentration) was subjected to size-exclusion chromatography using a BioSep-SEC-S 3000 column (Phenomenex) equilibrated in MALS buffer (25 mM Tris–HCl, pH 7.5, 100 mM NaCl, 4 mM $MgCl_2$, and 2 mM EGTA). Where specified, wild-type or mutant atlastin-1 was incubated with GDP, GppNHp, or GDP•AlF_x (2 mM) for 30 min at room temperature prior to injection. The column was coupled to a static 18-angle light scattering detector (DAWN HELEOS-II) and a refractive index detector (Optilab T-rEX) (Wyatt Technology). Data were collected every second at a flow rate of 1 ml/min. Data analysis was carried out using the program ASTRA V, yielding the molar mass and mass distribution (polydispersity) of the sample. For normalization of the light scattering detectors and data quality control, monomeric BSA (Sigma) was used. Molecular weight distributions were determined by using the Multipeak Fitting Package in Igor Pro (WaveMetrics).

GTPase assay

GTPase activity was measured using the Enzchek Phosphate Assay kit (Molecular Probes) following the manufacturer's instructions. Measurements were

carried out in a 96-well plate (Nunc) in a total volume of 250 µl. Recombinant wild-type or mutant atlastin-1 (at concentrations 0, 0.25, 0.5, 1, 2, and 4 µM) was combined with 1 U/ml purine nucleoside phosphorylase (PNP), 200 µM 2-amino-6-mercapto-7-methylpurine riboside (MESG), and provided buffer (20mM Tris–HCl, pH 7.5, 1mM $MgCl_2$, 0.1mM sodium azide). The plate was incubated at room temperature for 10 min, after which reactions were started by addition of 400 µM GTP (or alternatively, 50 mM Tris–HCl pH 7.5 for controls). Plates were assayed at 37°C in a Powerwave XS microplate reader (BioTek). Absorbance at 360 nm was monitored in 30 s intervals for 30 min. Data were normalized to a phosphate standard curve, and initial velocities were calculated using the portion of the curve corresponding to the first 5% of consumed product. Data reported are means ± s.e.m. of three independent experiments.

Dye labeling of atlastin-1

Dye labeling using Alexa dyes 488-C_5 maleimide and 647-C_2 maleimide (Invitrogen) for donor and acceptor, respectively, was performed using the manufacturer's guidelines. In brief, protein at a final concentration of ~80 µM was mixed with a 15× molar excess of the dye molecule in a final buffer composition of 25 mM Tris–HCl, pH 7.4, 100 mM NaCl, and 0.5 mM TCEP. Protein was incubated with the reducing agent TCEP for ~15 min prior to mixing with dye. All reactions were topped off with nitrogen before sealing off the reaction tubes to reduce reactive oxygen species. Reactions were kept at room temperature for 2 h, followed by overnight incubation at 4°C, all in the absence of light. Reactions were quenched by

the addition of 50 mM β-mercaptoethanol. Excess dye was then removed using Millipore concentrators (30kDa cutoff) with several rounds of buffer exchange, followed by determination of degree-of-labeling (DOL). All reactions used for FRET measurements reached a DOL of 90–110%.

FRET measurements

FRET measurements were made by mixing 1 μM of donor atlastin-1 (ECFP tagged or Alexa 488 labeled) and 20 μM acceptor atlastin-1 (EYFP tagged or Alexa 647 labeled) in assay buffer (25mM Tris–HCl, pH 7.4, 100 mM NaCl, and 4 mM $MgCl_2$), with or without 2 mM GTP, GDP, or GppNHp. Measurements taken for GDP•AlF_4^- were done using 25 mM Tris–HCl, pH 7.4, 100 mM NaCl, 4 mM $MgCl_2$, 2 mM EGTA, 2 mM $AlCl_2$, and 20 mM NaF with or without 2 mM GDP. Measurements were taken on a UV–Vis spectrofluorometer (PTI Quantamaster 40), exciting at 445 nm (ECFP) or 493 nm (Alexa 488) and scanning emission spectra between 455 and 650 nm (ECFP/EYFP) or 505 and 800nm (Alexa 488/647). All measurements were performed in triplicate. FRET efficiencies were calculated by using the emission intensity of the apo state (no nucleotide) at 473 nm (emission peak of ECFP) or 516 nm (emission peak of Alexa 488) as the no-FRET scenario. The following equation was used to calculate the FRET efficiency for equilibrium experiments:

$$E = 1 - \frac{F_{DA}}{F_D}$$

where E is FRET efficiency, F_{DA} is the fluorescence intensity of the donor with the acceptor present, and F_D is the fluorescence intensity of the donor without the acceptor. Distance estimates were calculated using the equation:

$$E = \frac{1}{1 + \left(\frac{r}{R_0}\right)^6}$$

where E is the FRET efficiency, calculated above, r is the actual distance (to be calculated), and R_0 is the Förster distance for a particular FRET pair. For ECFP/EYFP, R_0 is 47 Å, and for Alexa 488/647 is 56 Å.

Kinetic FRET data were recorded using a stopped-flow instrument (Kintek SF-2004) with submillisecond mixing dead times. A mixture of donor and acceptor atlastin-1 (both at 1 μM) in assay buffer were mixed with either buffer alone or buffer supplemented with nucleotide (2 mM GDP, GTP, GppNHp, or GTPγS) using the stopped-flow drive syringes. In the case of GDP•AlF_x, the protein donor/acceptor mixture was in a buffer containing 25 mM Tris–HCl, pH 7.4, 100 mM NaCl, and 4 mM $MgCl_2$, 2 mM EGTA, 2 mM $AlCl_2$, and 20 mM NaF. This was then mixed with this buffer supplemented with 2 mM GDP. The two solutions were mixed at a ratio of 1:1, at a flow rate of 8 ml/s in a total cell volume of 30 μl. The cell was illuminated by light from a xenon arc lamp, with a monochromator used to select a narrow band around 445 nm (the excitation of ECFP) or 493 nm (the excitation of Alexa 488). Fluorescence signals from ECFP/EYFP or Alexa 488/647 were recorded using two independent photomultiplier tubes with appropriate filters (Chroma) in place (B460-490, D535/25 for ECFP/EYFP; D525/50, HQ645/75 for 488/647).

Kinetic modeling of fast-mixing FRET

FRET simulations were programmed and performed using MATLAB R2010b (Mathworks). First, time-dependent binding was modeled by simple second-order kinetics for dimerization constrained by the mass conservation law. Discrete time steps of 10 ms were used to match instrumentation resolution. The bound-state model for the dimer consisted of two quasi-stable configuration states: the initial dimerization state D_1 and a relaxed dimer state D_2. Transitions between these states were governed by a relaxation rate constant k_{12}, the transition time t_{12}, and a set of transition states D_{12}. Finally, by assuming the proximity of conjugate labels within dimers at each configuration and transition state, the Förster equation was used to determine FRET efficiencies, and to calculate the total simulated FRET signal at each time step. A full description of equations used and assumptions made are described in Appendix A.

N-Methylanthraniloyl (Mant)-nucleotide binding

On and off rates of mant nucleotides (mant-GppNHp, mant-GDP, or mant-GTP) were determined by measuring the change in fluorescence of the mant nucleotide over time upon mixing with atlastin-1 constructs. Using a Kintek stopped-flow apparatus (Kintek SF-2004), a final concentration of 2.5 μM mant-GDP, mant-GTP, or mant-GppNHp (Invitrogen) was mixed with increasing concentrations of atlastin-1 (10–50 μM). Mant fluorescence (λ_{exc} = 366 nm, emission filter HQ460/40M; Chroma) was measured and the first 500ms of data was fit to a single-exponential decay curve. Observed rate constants from exponential fits were plotted versus protein concentration, with the resulting slope of the linear fit corresponding to k_{on}, and the y

intercept to k_{off}. In parallel experiments, the off rate (k_{off} diss.) was also directly measured by preloading atlastin-1 proteins with mant nucleotide and chasing with a high concentration (2.5 mM) of unlabeled nucleotide (GDP). The first 500ms of the resulting fluorescence decay curve was fit to a single-exponential decay, whose observed rate constant corresponds directly to the off rate (k_{off}). All fits were performed using Prism 5 (GraphPad Software Inc.). Rates obtained from both techniques are listed in Table 3.2.

RESULTS AND DISCUSSION

Crystallization of atlastin-1 bound to GppNHp and GDP-AlF_4^-

We determined two sets of crystal structures for the N-terminal, cytoplasmic module of human atlastin-1 comprising the G and middle domains (residues 1–446), bound to a transition state analogue GDP•AlF_4^- or non-hydrolysable GTP-mimic GppNHp (Table 3.1.). For the first set, we used the HSP disease mutant variant $N^{440}T$ (space group $P2_12_12$; 4 molecules/asymmetric unit), while the second set made use of the wild-type protein containing a C-terminal hexahistidine tag (space group $P2_12_12_1$; 2 molecules/asymmetric unit). Crystallization conditions differed between the mutant and wild-type proteins, but for each variant the conditions were nearly identical for both nucleotide-bound states. The different conditions and constructs resulted in unique crystal packing interactions for $N^{440}T$ and wild-type atlastin-1 variants, respectively (Figures 3.2. and 3.3.). Nevertheless, the conformation of the protomers and dimeric assemblies within the crystals were virtually identical in all four crystal structures (Table 3.3.), with the exception of the identity of the bound nucleotide and

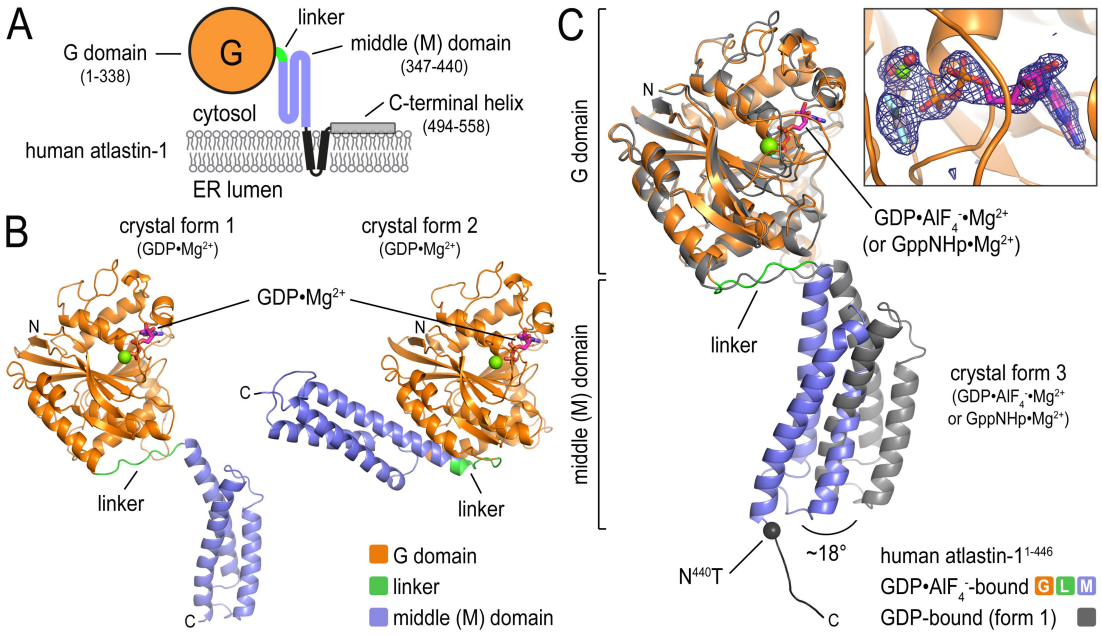

Figure 3.1. Structures of atlastin-1. (A) Topology of atlastin-1. The globular G domain (orange) is connected to the middle domain (blue) by a short linker (green). This N-terminal, cytoplasmic unit is followed by two transmembrane a helices (black) and a C-terminal amphipathic helix (grey), which has been shown to interact with the lipid membrane. (B) Protomer structures of crystal forms 1 and 2. The GDP-bound structures of atlastin-$1^{1–446}$ were aligned relative to their G domains (Byrnes and Sondermann, 2011). Nucleotide and Mg^{2+} are shown as sticks and spheres, respectively. (C) Protomer structures of crystal form 3. The GDP•AlF_4^--bound form 3 structure of atlastin-$1^{1–446}$-$N^{440}T$ was superimposed on the GDP-bound form 1 structure with the G domain as the reference. The form 1 structure is shown in grey and the form 3 structure is colored according to (A). Position of missense mutation in form 3 structure is indicated and its Cα is shown as a black sphere. An $F_o - F_c$ omit map for the nucleotide (inset) is contoured at 4.0 sigma.

the extreme C-termini that contain either the $N^{440}T$ mutation or the hexahistidine tag (and are involved in specific crystal lattice contacts) (Figures 3.2. and 3.3.). The crystallographic data suggest nucleotide-bound dimers as the biologically relevant unit, which is supported by size-exclusion chromatography-coupled static multi-angle light scattering (SEC-MALS), a method for determining the absolute molecular weight of particles in solution. In these experiments, there is no evidence of higher order oligomerization beyond dimers for the soluble, wild-type protein or the $N^{440}T$ mutant

Figure 3.2. Crystal structure of atlastin-1$^{1-446}$-N^{440}T form 3 crystal structure bound to GppNHp or GDP•AlF$_4^-$. (A) Overview of asymmetric unit. Atlastin-1$^{1-446}$-N^{440}T crystallizes as a tetramer in the asymmetric unit. An interaction of the C-terminal tail of one protomer with the G domain of an adjacent molecule is shown in the inset. (B) Detailed view of interactions of the C-terminal tail with an adjacent G domain. Residues 440-446 (grey) from molecule B and residues from the G domain of molecule C (yellow) that interact with them are shown as sticks and labeled. An $F_o - F_c$ omit map for the tail motif is contoured at 3.5 sigma. (C) Superposition of crystal form 1 and 3. The respective G domains of crystal form 1 and 3 were superimposed to assess whether tail packing interactions coincide with conformational changes in the G domain. No significant changes were observed. (D) Nucleotide binding pocket of form 3 crystal structures. The protein is shown in cartoon presentation, GDP•AlF$_4^-$ (upper panel) or GppNHp (lower panel) are shown as sticks, and Mg^{2+} and waters are shown as green and red spheres, respectively. Nucleotide $F_o - F_c$ omit map is contoured at 4.0 sigma. (E) Catalytic residues in the nucleotide binding pocket of form 3 crystal structures. The protein is shown in cartoon presentation except for residues that interact with the phosphates of the nucleotide, which are shown as sticks. GDP•AlF$_4^-$ (upper panel) or GppNHp (lower) are shown as sticks, and Mg^{2+} is shown as spheres.

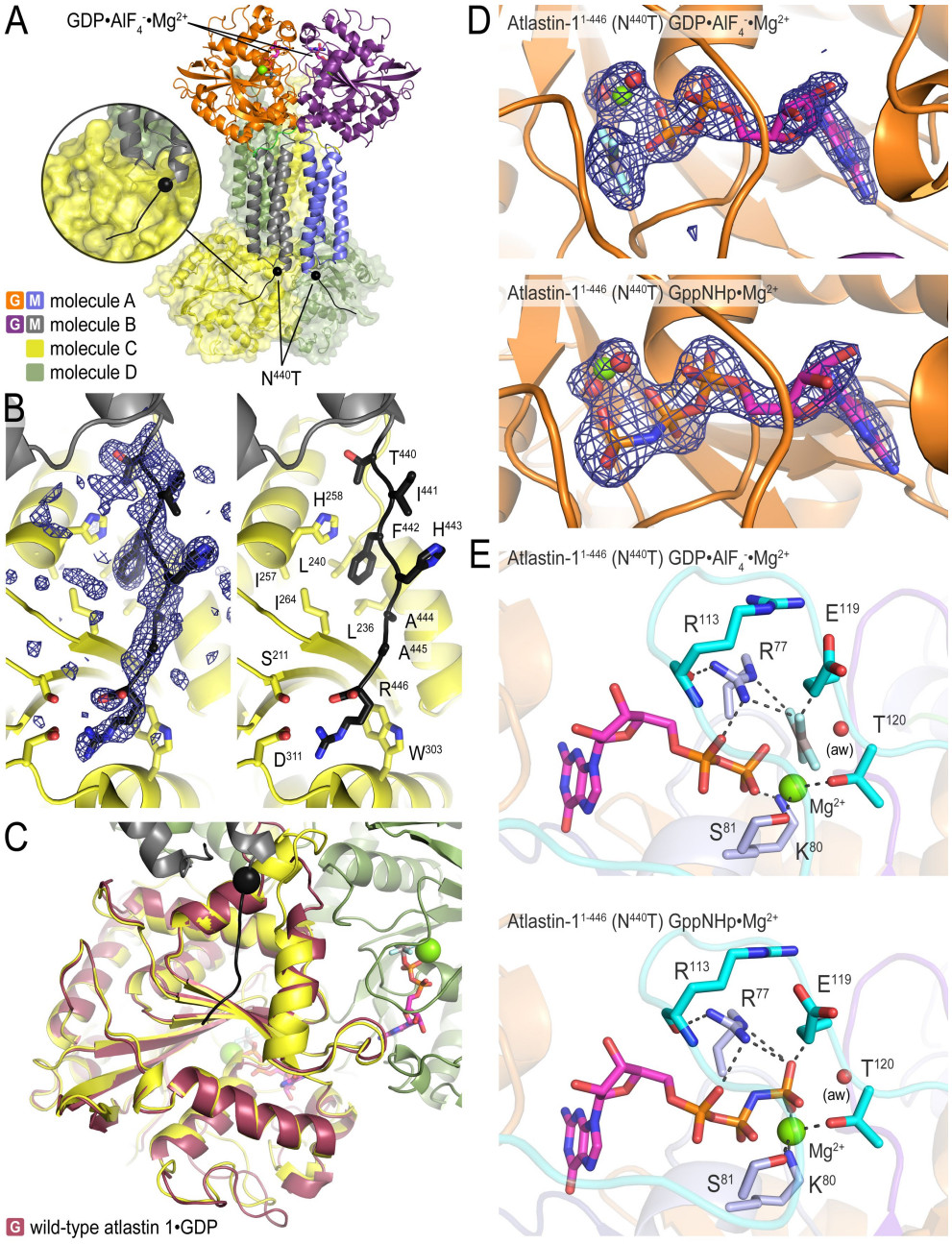
A
GDP•AlF4-•Mg2+
G M molecule A
G M molecule B
molecule C
molecule D
N440T
B
T440
I441
H258
F442
H443
L240
I257
I264
L236
A444
A445
S211
R446
D311
W303
C
G wild-type atlastin 1•GDP
D
Atlastin-1 1-446 (N440T) GDP•AlF4-•Mg2+
Atlastin-1 1-446 (N440T) GppNHp•Mg2+
E
Atlastin-1 1-446 (N440T) GDP•AlF4-•Mg2+
R113
E119
R77
T120
(aw)
Mg2+
S81
K80
Atlastin-1 1-446 (N440T) GppNHp•Mg2+
R113
E119
R77
T120
(aw)
Mg2+
S81
K80

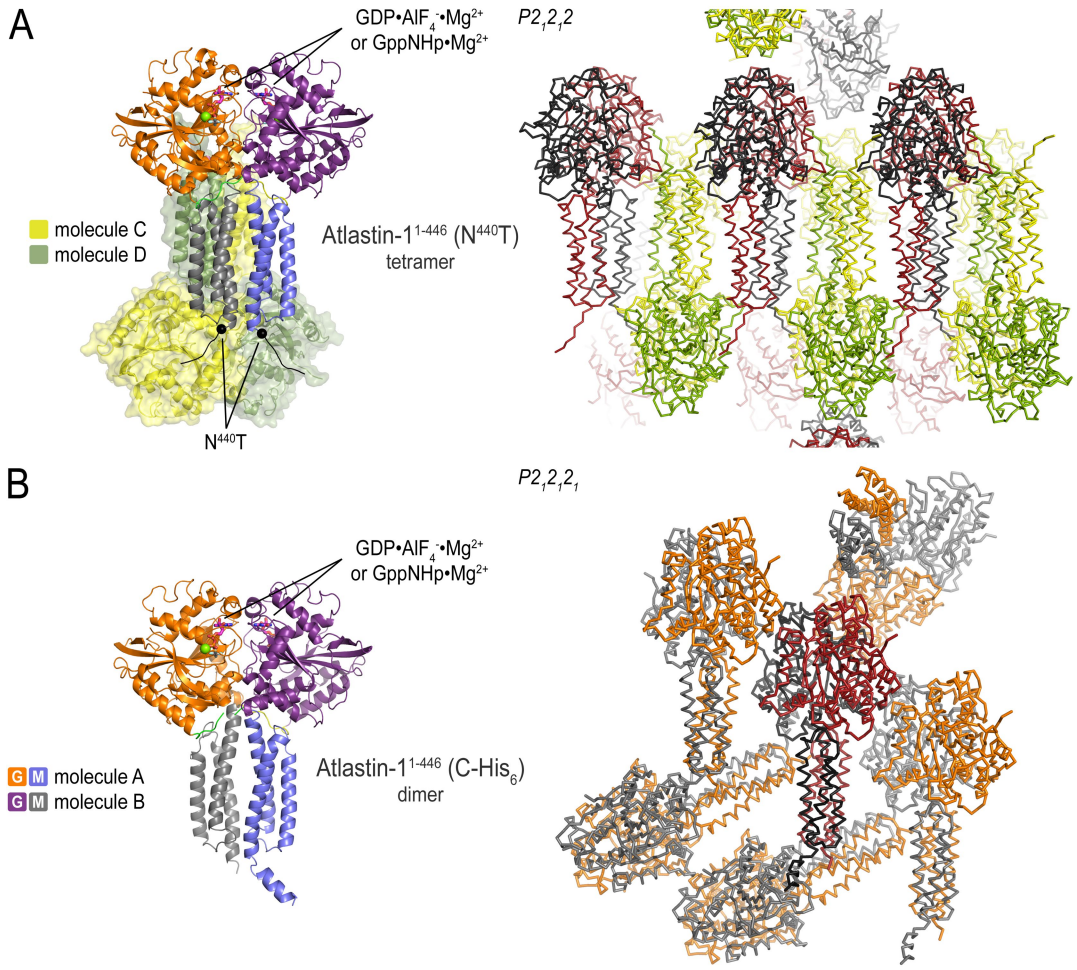

Figure 3.3. Crystal packing interactions. (A) Asymmetric unit and crystal packing of atlastin1$^{1\text{-}446}$-N^{440}T bound to GppNHp or GDP•AlF_4^-. The asymmetric unit contains 4 protomers, forming an anti-parallel dimer of dimers. (B) Asymmetric unit and crystal packing of atlastin1$^{1\text{-}446}$-C-His_6 bound to GppNHp or GDP•AlF_4^-. The asymmetric unit contains 2 protomers that form a very similar dimer as observed in atlastin1$^{1\text{-}446}$-N^{440}T structures bound to the same nucleotides.

variant when bound to GppNHp or GDP•AlF_4^- (Figure 3.4.). We chose the atlastin N^{440}T mutant bound to GDP•AlF_4^- for our illustration of this particular state, yet the crystallographic results apply to all four structures considering the striking similarities between them. We refer to this state as crystal form 3.

The structures reveal several previously unseen features that provide novel insights into the catalytic mechanism of atlastin-mediated membrane fusion, which

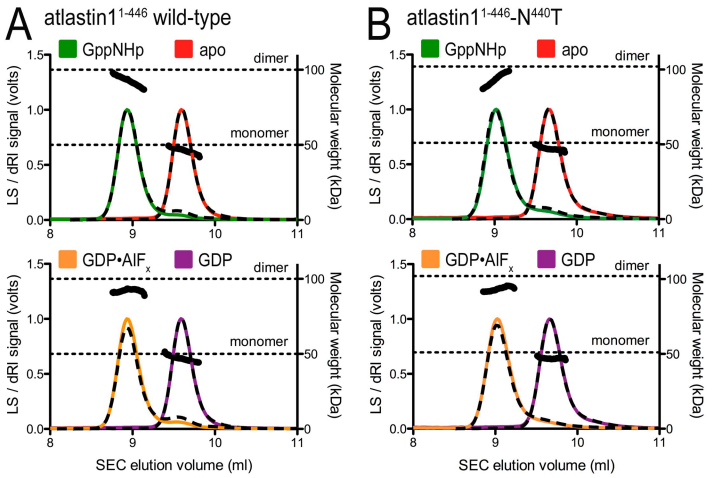

Figure 3.4. Atlastin-1$^{1\text{-}446}$-N^{440}T oligomerization in solution. (A) SEC-MALS data for wild-type Atlastin-1$^{1\text{-}446}$. The signal from the 90°-light scattering detector and refractive index detector are shown as colored, solid lines (apo, red; GppNHp-bound, green; GDP-bound, purple; GDP•AlF$_x$-bound, orange) and black, dashed lines respectively (left Y axis). Average molecular weight calculations across the protein peak are shown as black circles (right Y axis). The theoretical molecular weight (based on primary sequence) for the monomer and dimer are shown as horizontal dashed lines. Proteins (30-40 μM) were incubated with nucleotides (2 mM) at least 30 min prior to SEC-MALS analysis. (B) SEC-MALS data for the N^{440}T mutant introduced into atlastin-1$^{1\text{-}446}$.

will be discussed in detail below. Notably, we observe clear density for the γ-phosphate or AlF_4^- moiety, in the GppNHp- and GDP•AlF_4^--bound structures, respectively (Figure 3.1.C). Dimerization in solution is only observed in the presence of GppNHp or GDP•AlF_4^-, but not in the apo state or when bound to GDP (21), indicating that we crystallized a physiologically relevant conformation. In addition, we observe conformational changes of the G domain's switch regions and G domain dimer interface associated with GTP analogue binding. Overall, the form 3 crystal structure is most similar in conformation to the previously determined, GDP-bound form 1 structure, characterized by the middle domain being dislodged from the G domain, with one difference being an 18°-rigid-body rotation of the middle domain relative to the G domain (Figure 3.1.C).

Table 3.1. X-ray data collection and refinement statistics.

	atlastin-1 1-446, $N^{440}T$ GDP•AlF_4^-	**atlastin-1 1-446, $N^{440}T$ GppNHp**	**atlastin-1 wildtype, $CHis_6$ GDP•AlF_4^-**	**atlastin-1 wildtype, $CHis_6$ GppNHp**
Data collection				
X-ray source	CHESS A1	CHESS A1	CHESS A1	CHESS A1
Wavelength (Å)	0.9771	0.9771	0.9771	0.9771
Space group	$P2_12_12$	$P2_12_12$	$P2_12_12_1$	$P2_12_12_1$
Unit cell parameters				
a, b, c, (Å)	129.0, 267.1, 62.1	132.0, 268.1, 62.4	49.6, 116.4, 185.4	49.7, 115.8, 181.1
α, β, γ (°)	90, 90, 90	90, 90, 90	90, 90, 90	90, 90, 90
Resolution range (Å)[a]	50-2.3 (2.38-2.30)	50-2.6 (2.69-2.60)	50-2.1 (2.18-2.09)	50-2.2 (2.28-2.20)
No. of reflections				
Total	743,898 (45,513)	540,312 (44,595)	512,721 (43,745)	334,053 (9,968)
Unique	92,313 (7,714)	69,639 (6,656)	63,782 (6,730)	47,929 (2,167)
Completeness (%)	95.3 (81.1)	99.7 (97.4)	98.9 (96.8)	90.3 (41.7)
Redundancy	14.6 (3.0)	7.8 (6.7)	8.0 (6.5)	7.0 (4.6)
I/σ (I)	35.6 (10.5)	12.3 (3.1)	23.3 (4.1)	16.1 (1.9)
R_{meas} (%)	12.0 (50.4)	16.0 (61.1)	8.1 (47.4)	10.1 (59.3)
Refinement				
R_{work}/R_{free} (%)	20.6/25.6	20.1/23.6	19.9/24.9	17.3/21.8
r.m.s. deviations				
Bond length (Å)	0.008	0.014	0.008	0.006
Bond angles (°)	1.19	1.68	1.23	0.98
No. of atoms	14,506	14,015	7,459	7,192
Protein	13,486	13,480	6,730	6,762
Ligands	212	132	68	66
Water	704	403	661	364
Ave. B-factors (Å^2)				
Protein	27.8	28.2	30.7	41.5
Water	32.8	24.5	34.0	40.6
Ramachandran (%)				
Favored	99	98	98	98
Outliers	0	0	0	0.1

[a]Values in brackets are for the highest resolution bin.

Table 3.2. Nucleotide binding to human atlastin-1.

Protein	Nucleotide	k_{on} (1/μM s)	k_{off} (1/s)	$k_{off}^{diss.}$ (1/s)	K_d (μM)
Atlastin-1^{1-446} wt	GDP	0.40±0.015	4.80 ±0.384	2.31 ±0.171	5.77 ±0.479
	GTP	0.32±0.021	4.05±0.594	3.72±0.287	11.63±1.18
	GppNHp	0.51±0.079	19.36±2.23	20.63±3.285	40.45±8.99
Atlastin-11-446 $R^{77}A$	GDP	0.34±0.013	5.92±0.302	2.77±0.170	8.14±0.589
	GTP	0.64±0.030	4.38±0.828	8.02±0.166	12.53±0.642
	GppNHp	0.70±0.093	5.08±2.73	4.25±1.465	6.07±2.243
Atlastin-1^{1-339} wt	GDP	0.20±0.009	7.21±0.214	4.53±0.592	22.65±3.13
	GTP	ND	ND	ND	ND
	GppNHp	ND	ND	ND	ND
Atlastin-1^{1-446} wt	GDP	0.108±0.010	8.30±0.245	6.55±0.673	60.65±8.39
+	GTP	0.055±0.040	9.34±1.24	7.30±4.47	132.7±126.2
Atlastin-$1^{340-446}$ wt	GppNHp	ND	ND	ND	ND
Atlastin-1^{1-446} wt	GDP	0.086±0.010	9.07±0.252	8.12±0.674	94.42±13.49
+	GTP	ND	ND	ND	ND
Atlastin-$1^{340-446}$ $M^{347}E$	GppNHp	ND	ND	ND	ND
Atlastin-1^{1-366} wt	GDP	0.128±0.020	8.65±0.520	6.36±0.551	49.69±8.88
	GTP	0.153±0.041	7.93±1.11	7.12±2.865	46.54±22.50
	GppNHp	ND	ND	ND	ND
Atlastin-1^{1-446} $M^{347}E$	GDP	0.186±0.010	5.63±0.165	4.13±0.108	22.2±1.33
	GTP	0.128±0.027	4.29±0.661	4.21±1.00	32.9±10.45
	GppNHp	ND	ND	ND	ND

Abbreviations: ND, not detected; wt, wild type. [a]mant derivatives were used to determine on and off rates using stopped-flow fluorescence spectroscopy.

Table 3.3. Comparison of G and middle domains in atlastin-1 crystal structure.

Protomer RMSD:

	C-His GppNHp	C-His GDP•AlF_4^-	N^{440}T GppNHp	N^{440}T GDP•AlF_4^-
C-His GppNHp	×	0.209	0.268	0.271
C-His GDP•AlF_4^-	0.209	×	0.276	0.265
N^{440}T GppNHp	0.268	0.276	×	0.157
N^{440}T GDP•AlF_4^-	0.271	0.265	0.157	×

Dimer RMSD:

	C-His GppNHp	C-His GDP•AlF_4^-	N^{440}T GppNHp	N^{440}T GDP•AlF_4^-
C-His GppNHp	×	0.220	0.301	0.320
C-His GDP•AlF_4^-	0.220	×	0.335	0.310
N^{440}T GppNHp	0.301	0.335	×	0.163
N^{440}T GDP•AlF_4^-	0.320	0.310	0.163	×

Extensive dimerization in the GppNHp and transition state-bound structure

Distinct crystallographic dimers of GDP-bound atlastin-1 were apparent in the previously determined structures (form 1, 'relaxed-parallel'; form 2, 'extended'; Figure 3.5.A) (20, 21). Both had dimerized G domains, but they differed in the spatial arrangement of their middle domains. In the form 2 dimer, the middle domains fold back onto and are engaged with their respective G domains, with the C-termini pointing in opposite directions. In contrast, the protomers in the form 1 dimer are crisscrossed with the middle domains running in parallel without interacting with each other. Despite the new form 3 dimer having similar topology to the original GDP-bound form 1, the interfaces are quite different. In general, the interfacial area is larger in the structures of atlastin bound to GppNHp and GDP•AlF_4^- than in the GDP-bound models (3852 versus 2797 $Å^2$), both considering the G domain dimerization as well as the interactions between the middle domains (G domain dimer: 1886 versus 1226 $Å^2$; linker/ middle domain dimer: 1257 versus 406 $Å^2$). The middle domains in the parallel dimers interact at the crossover point, which involves the linker between the G and middle domains (Figure 3.5.). In addition, the interfacial surface extends to the first and third helix of the middle domains in the form 3 dimer (Figure 3.5.B), forming a tight-parallel state with respect to middle domain packing and orientation, respectively. The more extensive buried surface area in the tight-parallel form 3 dimer is consistent with atlastin's ability to dimerize in solution in the presence of GppNHp and GDP•AlF_4^- (Figure 3.4.A; (21)).

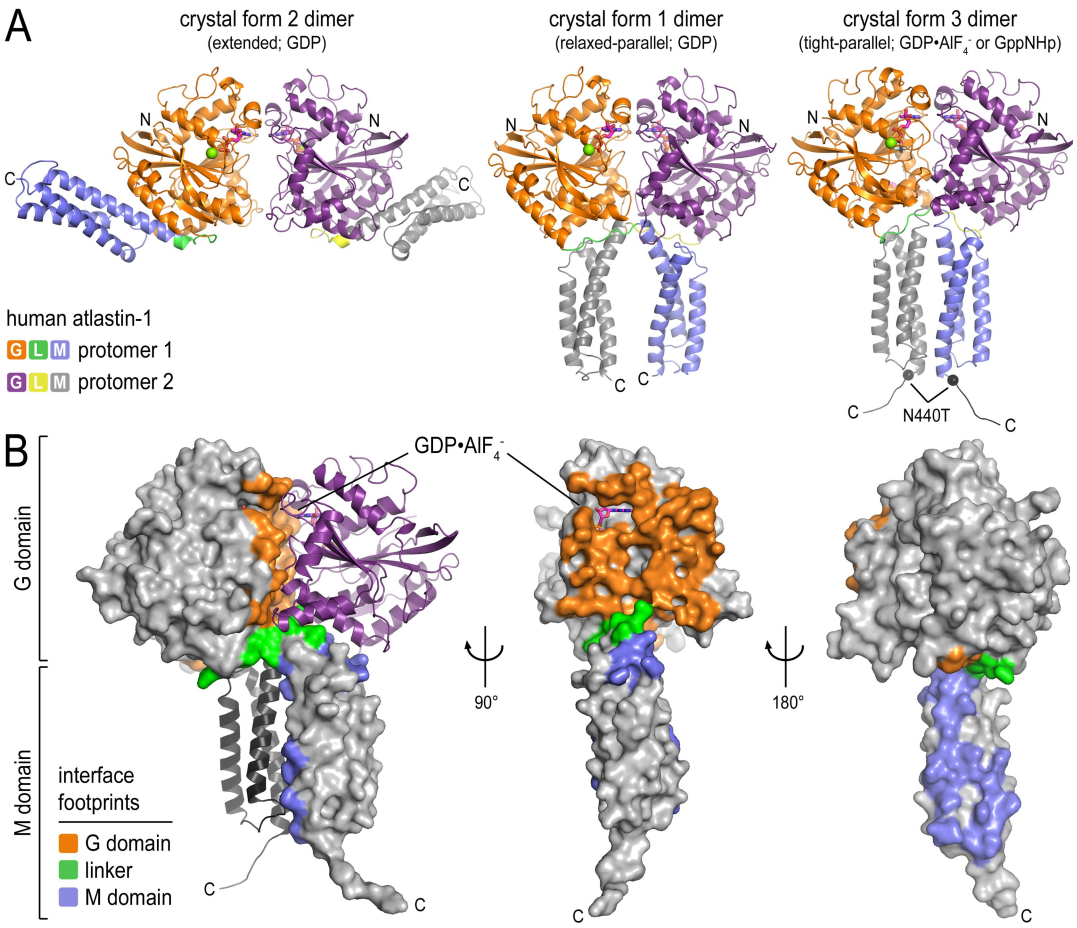

Figure 3.5. Crystallographic dimers of atlastin-1$^{1–446}$. (A) Atlastin-1 dimers. Crystallographic dimers observed in crystal form 2 (extended, $P2_12_12_1$ symmetry, left), form 1 (relaxed-parallel, $P6_522$ symmetry, middle), and form 3 (tight-parallel, $P2_12_12$ symmetry, right) are shown. Bound nucleotides and metal ions are shown as sticks and spheres, respectively. (B) Crystal form 3 dimer interface. Interface residues are shown in color on the surface of one half of the dimer.

The catalytic mechanism of atlastin-1

As with other G proteins, binding of GTP and transition state analogues, GppNHp or GDP•AlF_4^-, respectively, has profound effects on the conformation of the switch regions within the G domain of atlastin (Figure 3.6.). While the GDP-bound G domains adopt a somewhat open conformation with regard to the nucleotide-binding pocket, switch motifs G2 (switch 1) and G3 (switch 2) in the newly determined

structures undergo major conformational changes, folding over the phosphate and AlF_4^- moieties (Figure 3.6.A). The conformational change positions R^{77} of the G1 motif (P-loop) above the phosphate moiety, with the guanidinium group interacting with the α- and γ-phosphate (or AlF_4^-) of the nucleotide (Figure 3.6.B), establishing its role as a catalytic arginine finger. R^{77} is conserved in the atlastin and GBP families of dynamin-related proteins, but not in dynamins, mitofusins, MxA, or Sey1p, a functional atlastin paralogue in yeast (Figure 3.6.A; (11)). This observation suggests that GBP and atlastin are more closely related and use an intramolecular arginine finger, whereas Sey1p employs a catalytic mechanism potentially involving an accessory metal ion and residues of an adjacent G domain within a dimeric assembly, as has been described for dynamin (19).

It is worth noting that in the GDP-bound structures, the side chain of R^{77} is surface exposed and forms a salt bridge with a glutamate residue of an adjacent G domain, and hence is central to the G domain dimer interface in these structures (20, 21). In our previous study, we introduced a charge-reversal mutation at position R^{77} ($R^{77}E$) to probe its involvement in dimerization of the N-terminal, cytoplasmic module used for crystallization. We noticed a markedly destabilized GppNHp-bound dimer and no dimerization in the presence of GDP•AlF_x (21). The mutant protein is also devoid of enzymatic activity and binds nucleotide poorly (20, 21). Here, we introduced a more subtle mutation by replacing R^{77} with alanine. In contrast to the $R^{77}E$ mutant, simple removal of the side chain ($R^{77}A$) has little effect on nucleotide-dependent dimerization in light scattering-based assays (Figure 3.6.C). Both wild-type

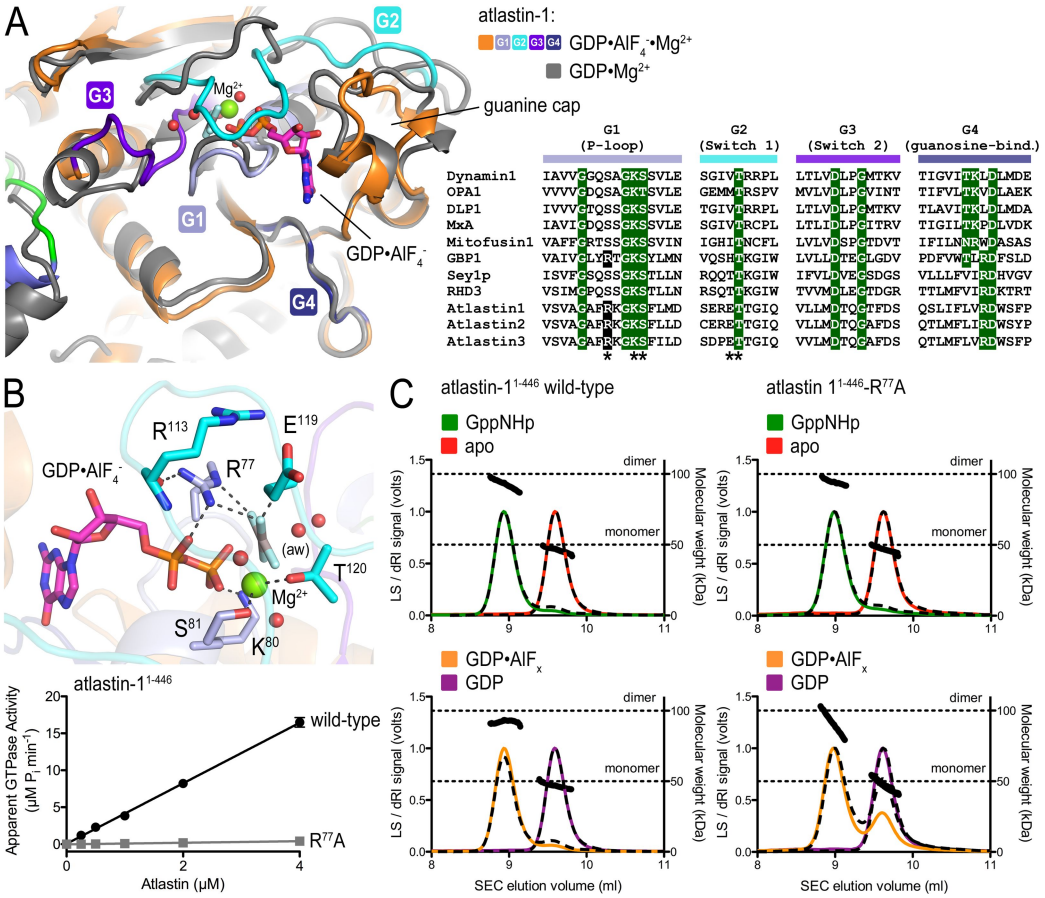

Figure 3.6. Catalytic mechanism of atlastin-1. (A) Conformational changes upon GTP analogue binding. The conformational changes in the nucleotide binding site between GDP-bound form 1 (grey) versus GDP•AlF_4^--bound form 3 (colored) are shown after superpositioning of the respective G domains. Nucleotide binding and switch motifs (motifs G1–G4) of the form 3 crystal structure are colored in shades of blue. On the right, a sequence alignment of several dynamin superfamily members shows conserved regions involved in nucleotide binding and hydrolysis. Strictly conserved residues are highlighted in green. Residues shown in (B) are marked with an asterisk. (B) Residues involved in nucleotide hydrolysis. The nucleotide binding pocket of crystal form 3 (upper) is shown, with residues making direct or indirect contacts with the phosphate groups of the nucleotide analogue are shown as sticks. Mg^{2+} is shown as a green sphere. The attacking water molecule (labeled 'aw') and Mg^{2+}-coordinating water molecules are shown as red spheres. Mutation of R^{77} to alanine abolishes GTPase activity (lower panel). The GTPase activity was determined by measuring the production of inorganic phosphate over time at various protein concentrations. (C) Nucleotide-dependent oligomerization of atlastin-$1^{1–446}$-R^{77}A SEC-MALS data for wild-type (left panels) and mutant (R^{77}A, right panels) atlastin-$1^{1–446}$ is shown. The signal from the 90°-light scattering detector and refractive index detector is shown as colored, solid lines (apo, red; GppNHp bound, green; GDP bound, purple; GDP•AlF_x bound, orange) and black, dashed lines, respectively (left Y axis). Average molecular weight calculations across the protein peak are shown as black circles (right Y axis). The theoretical molecular weight (based on primary sequence) for the monomer and dimer is shown as horizontal dashed lines. Proteins (30–40 μM) were incubated with nucleotides (2 mM) at least 30 min prior to SEC-MALS analysis.

atlastin and the $R^{77}A$ mutant variant form dimers in the presence of GppNHp and GDP•AlF_x, but are monomeric in GDP or in the absence of any nucleotide. Yet, $R^{77}A$ mutant protein has negligible GTPase activity of 0.1M μM P_i/min/μM when compared to 4.1mM μM P_i/min/μM for wild type (Figure 3.6.B), corroborating the role of R^{77} as atlastin's arginine finger. Based on the structural and mutagenesis data, one cannot rule out the possibility that R^{77} may have a dual function as an interfacial residue as well as a catalytic residue.

Thus far, we established that crystal form 3 depicts a catalytically competent, dimeric state of atlastin. Together with the observation of form 1-like, relaxed-parallel atlastin-2 dimers bound to GppNHp in electron micrographs (37), these new structures deviate from our modeling of small-angle X-ray scattering (SAXS) data that indicated GppNHp- and transition state analogue-bound atlastin adopting an extended conformation in solution, more similar to the crystal form 2 dimer (21). Yet, the fits between the crystallographic models and the solution scattering data were imperfect, suggesting either the presence of an alternative conformation or an ensemble of conformations in solution. Indeed, modeling of the SAXS data with multiple conformations (e.g., form 1, 2, and 3 dimers) improves the fits significantly, and points to a conformational heterogeneity of GppNHp- and GDP•AlF_4^--bound atlastin-1 (data not shown).

Measuring middle domain dimerization in atlastin via Förster Resonance Energy Transfer

While we revealed the catalytic core of atlastin, it is less clear what functional state the new crystal form 3 structure depicts and what role GTP hydrolysis plays during membrane fusion. The aforementioned studies focused on states that were bound to non-hydrolysable nucleotide analogues, limiting the insight into the molecular consequences of catalysis. To further investigate the solution conformation of atlastin and to later measure the kinetics of conformational changes within the dimer, we developed a Förster Resonance Energy Transfer (FRET)-based assay. Based on the crystal structures, we would predict that the extended form 2 dimer would not support FRET between fluorescent probes fused to the distal tips of the middle domains, while in the parallel dimers (forms 1 and 3) the fluorophores would come into close proximity allowing FRET to occur. We fused ECFP or EYFP to the C-terminus of the middle domain using a short linker segment to increase the rotational freedom of the fluorescent proteins (human atlastin-1, residues 1–446; linker: GTSTSG). Fusion proteins showed dimerization propensity similar to the parent proteins without the fluorescent moiety when analyzed by SEC-MALS, with dimerization occurring in the presence of GppNHp and GDP•AlF_x, but not in GDP or in the absence of any nucleotide (Figure 3.7.B). In addition, GTPase rates were almost identical (Figure 3.7.C) indicating proper functionality of the proteins used in the FRET assays.

First, we measured FRET at equilibrium in the presence of different nucleotides (Figure 3.7.D and E). Based on previous data, we predicted that no FRET

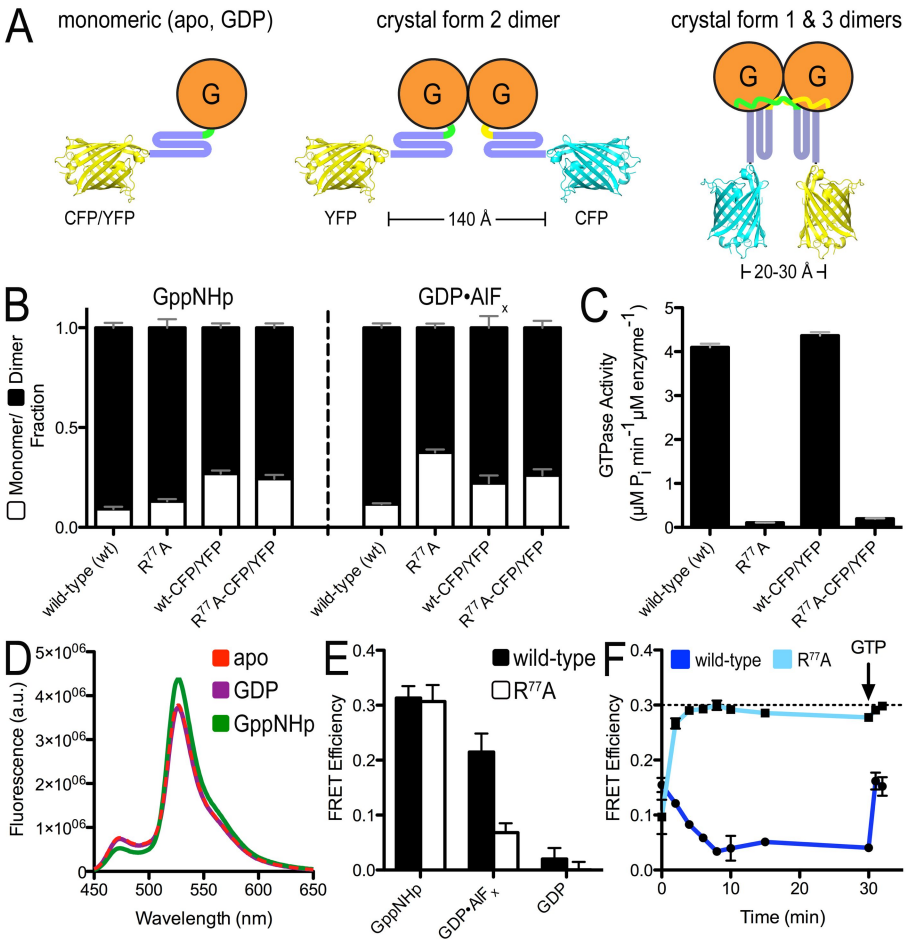

Figure 3.7. Atlastin-1 middle domain FRET using C-terminal ECFP/EYFP fusions. (A) Experimental design of measuring middle domain dimerization. Cartoon depiction of fluorescent protein-labeled atlastin-$1^{1–446}$ in various crystallographic dimer conformations. Estimated length measurements are based on the crystal structures shown in Figure 3.5.A. (B) Nucleotide-dependent dimerization of atlastin-$1^{1–446}$-ECFP/ EYFP-fusion proteins. Molecular weight fractions for GppNHp- or GDP•AlF_4^--bound atlastin-1 were determined by SEC-MALS and fitted using the Multipeak Fitting Package in Igor Pro. Error bars correspond to calculated errors in the fitting function parameters. (C) GTPase activity atlastin-$1^{1–446}$-ECFP/EYFP-fusion proteins. GTPase activity was determined by measuring the production of inorganic phosphate over time upon GTP hydrolysis at various protein concentrations. (D) Emission spectra of atlastin-$1^{1–446}$-ECFP/atlastin-$1^{1–446}$-EYFP mixtures at equilibrium. Protein (20μM total, 1:20 ratio of donor to acceptor) was mixed with either buffer or nucleotide for at least 20min prior to measurement, and was excited at 445 nm (apo, red dashed line; GDP, purple; GppNHp, green). (E) FRET efficiencies. FRET efficiencies of wild-type (black) and $R^{77}A$ mutant (white) atlastin-$1^{1–446}$-ECFP/EYFP in the presence of various nucleotides were calculated as stated in Materials and methods. (F) FRET efficiency versus time of wild type and mutant $R^{77}A$ in the presence of GTP. Either wild-type (dark blue) or mutant $R^{77}A$ (light blue) atlastin-$1^{1–446}$-ECFP/EYFP were mixed with an excess of GTP. Emission spectra were measured immediately after mixing, every 2 min up to 10 min, at 15 min, and at 30 min. The sample was then spiked with additional GTP, mixed, and measured again. Lamp shutters were closed in between measurements. A black dashed line represents the FRET efficiency of wild-type FRET pair in the presence of GppNHp at equilibrium.

would occur in the presence of GDP or absence of any nucleotide and there would be an increase in FRET efficiency in the presence of GTP or GTP analogues, although it was not clear to what extent or time-scale. Indeed, no change in either donor (ECFP) or acceptor (EYFP) fluorescence was detected between the apo state and the GDP-bound state (FRET efficiency of <0.02%). For incubations in the presence of GppNHp or GDP•AlF_x, we observed a decrease in donor fluorescence intensity and concomitant increase in acceptor fluorescence intensity, indicating robust FRET, with the FRET efficiency being comparable in both samples (30% in GppNHp and 22% in GDP•AlF_x). Using the FRET efficiencies obtained from the measurements in the presence of GppNHp and GDP•AlF_x, average distances of 54 and 57 Å were determined, respectively. In general, the FRET efficiency depends on the distance between the donor and acceptor fluorophores but also on the fraction of proteins in an FRET-competent state, and we cannot distinguish between the relative contributions with the current assay. Nevertheless, the apparent distances establish that the middle domains come into close proximity, at least for a fraction of the population, within atlastin dimers in solution.

Middle domain-mediated FRET was higher in GDP•AlF_x and GppNHp, or for the catalytically inactive $R^{77}A$ mutant in GTP than that observed for wild-type atlastin-1 in the presence of GTP (Figure 3.7.F). Since GTP will be hydrolyzed efficiently by atlastin-1 over the course of the assay, a lower FRET efficiency can be explained by sample heterogeneity and by exhaustion of the available GTP pool and a build-up of GDP, which does not support dimerization and therefore FRET. This argument was corroborated by the observation that FRET decreased over time in

solution containing GTP and reached a minimum after about 10 min under the chosen conditions (Figure 3.7.F). Addition of GTP at a later time point brought the signal up again to the initial value. The aforementioned differences in apparent FRET maxima may be due to fast rates of hydrolysis and the fact that GTP-bound wild-type atlastin likely populates different conformations than the catalytically inactive mutant. It may also indicate that the FRET-competent state is rather short-lived for a nucleotide hydrolyzing system.

Kinetics of middle domain dimerization

The equilibrium FRET data suggest that at least a fraction of atlastin resides in the more compact conformation, characterized by parallel middle domains (crystal form 1 or 3), when bound to GppNHp or GDP•AlF_4^- (Figure 3.7.). In addition, it appears that the states interconvert over time, suggesting that the protein may populate several conformations. To determine the kinetics of this conformational switch, we turned to rapid-mixing fluorescence measurements. An equimolar mixture of ECFP- and EYFP-fusion proteins (0.5μM each, final concentration) was mixed with buffer or buffer containing an excess concentration of nucleotide (1mM final concentration) using the syringe drive from a submillisecond-dead time stopped-flow instrument, and the subsequent changes in donor and acceptor fluorescence were monitored simultaneously over time.

Both donor and acceptor fluorescence traces showed little to no change when the FRET pair was mixed with either buffer alone or GDP-containing buffer. However, after mixing with GTP, GppNHp, GTPγS, or the transition state analogue

GDP•AlF_x, the proteins exhibited concurrent, inverse changes of donor and acceptor fluorescence intensity, indicating FRET (Figures 3.8.A and 3.9.A). When incubated with GppNHp, GTPγS, or GDP•AlF_x, fluorescence intensities change gradually over about a 10-min period. In contrast, when the FRET pair is mixed with GTP, there is a rapid decrease in donor fluorescence and simultaneous increase in acceptor fluorescence, with maximal FRET being reached after only ~2s. Subsequently, the system relaxes to an intermediate FRET level before it drops off after several minutes when the GTP pool is consumed (Figures 3.7.F and 3.8.A). Since the on-rates of nucleotide binding for both GTP and GppNHp are approximately the same (Table 3.2.), this sharp difference in timescale can be explained by a driving force incurred by GTP hydrolysis. In addition, the unique appearance of the minimum/maximum observed in the donor/acceptor time trace with GTP can possibly be rationalized by an initial synchronization of the GTP hydrolysis reaction, where the dimer takes on a very close conformation (i.e., the tight-parallel form 3 conformation; Figure 3.5.A) followed by a more relaxed FRET state (i.e., the relaxed-parallel form 1 conformation; Figure 3.5.A), possibly coupled with post-hydrolysis events such as phosphate release.

Although dimerization of the catalytically inactive mutant $R^{77}A$ has been observed in light scattering and steady-state FRET experiments, the kinetics appear to be rather slow (Figure 3.8.A, right panel), indicating a crucial role of the arginine finger in the catalytic mechanism and conformational switching. Interestingly, binding on-rates of fluorescently labeled nucleotides are comparable for wild-type and $R^{77}A$

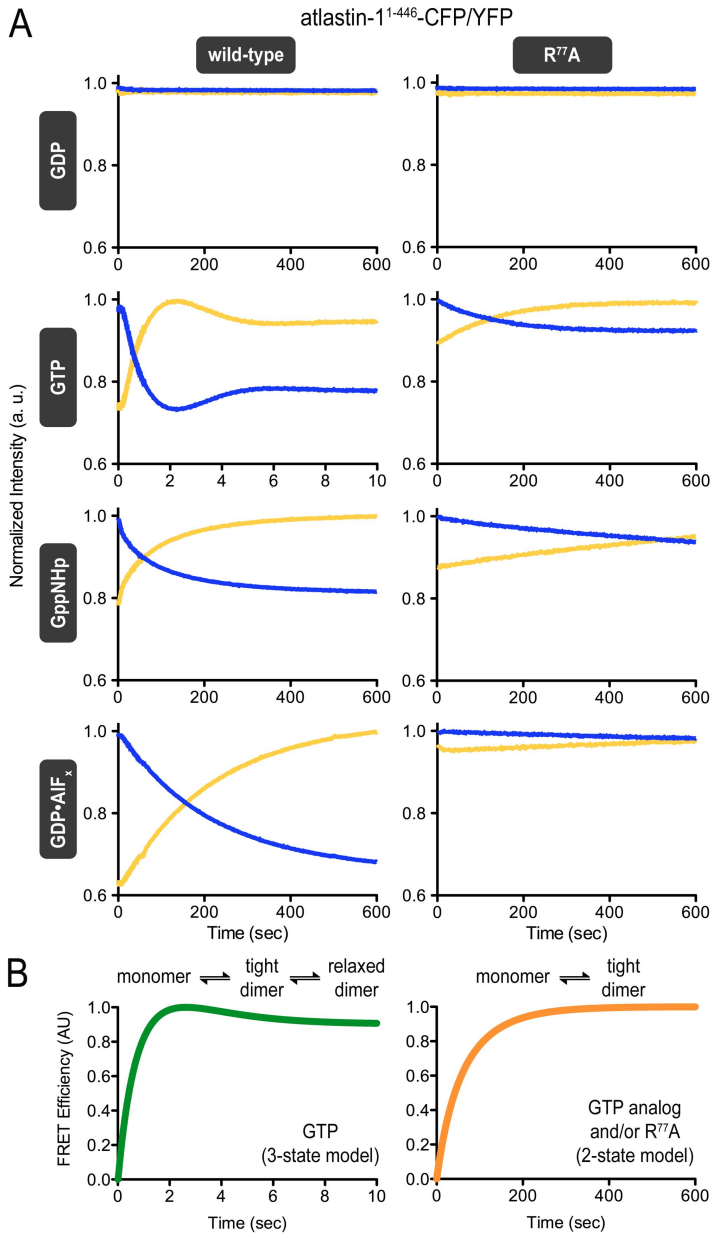

Figure 3.8. Kinetics of atlastin-1 middle domain FRET. (A) Stopped-flow FRET measurements. A mixture of atlastin-$1^{1–446}$-ECFP/EYFP fusion proteins (1 μM each) was prepared in the absence of nucleotide, and mixed 1:1 with either buffer (apo) or nucleotide-containing buffer (GDP, GTP, GppNHp, or GDP•AlF_x; concentration: 2 mM) using a stopped-flow apparatus. A xenon arc lamp was set to 445 nm excitation, and two photomultiplier tubes with appropriate filters in place were used to measure emission output over time. (B) Simulations of FRET data. A three-state system was used for a hydrolysis competent reaction (left, green), whereas a two-state system (right, orange) was applied to model nucleotide-dependent processes in the absence of GTP hydrolysis. Both simulations start with a monomeric assembly, which is then allowed to interconvert to a tight-parallel (form 3-like) dimer. In the hydrolysis competent case, this dimer is then allowed to interconvert to a relaxed-parallel (form 1-like) dimer.

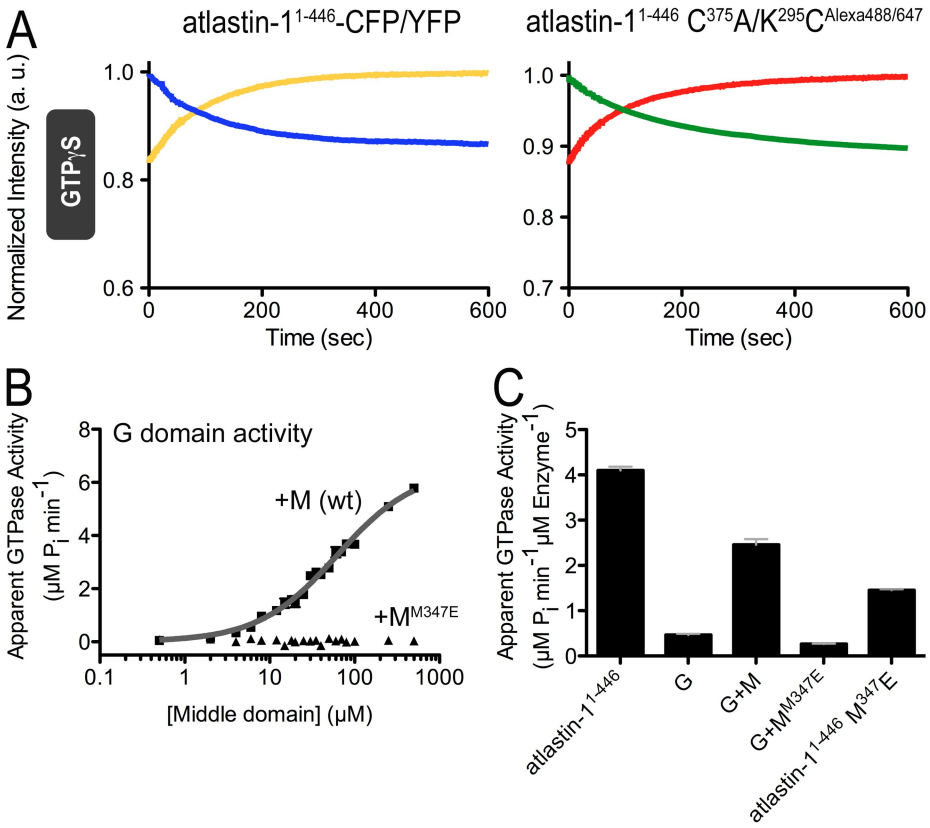

Figure 3.9. FRET in an alternative GTP analog and middle domain interaction characterization. (A) Middle and G domain time-resolved FRET following mixing with the GTP analog GTPγS. A mixture (1μM final) of atlastin-$1^{1\text{-}446}$-ECFP/EYFP fusion proteins (left panel) or Alexa 488 and 647-labeled atlastin-$1^{1\text{-}446}$ (right panel) was prepared in the absence of nucleotide, and mixed 1:1 with nucleotide-containing buffer (GTPγS; 2 mM) using a stopped-flow apparatus. Experimental details are as stated in Figures 3.8A and 3.11. Time scale of FRET change was monitored over 10 min, and proceeds with similar kinetics to the GTP analog GppNHp (see Figures 3.8.A and 3.11. for comparison). (B) Middle domain titration increases G domain activity. With a G domain concentration of 2 μM, middle domain concentrations (either wild-type [squares] or point mutant $M^{347}E$ [triangles]) were varied from 0.5 μM to 500 μM and the resulting change in activity compared to G domain alone was plotted versus the concentration of middle domain added on a $\log_{10}$ scale. The data were fit to a one-site saturated binding equation with a variable hill coefficient (fit shown in grey for wild-type; no fit could be determined for $M^{347}E$ data). The fit resulted in an apparent K_d of 62.2±6.6 μM and a hill coefficient of 0.931±0.048. Experiments were conducted in triplicate. We report the means with the error bars representing SEM. (C) Middle domain point mutation $M^{347}E$ reduces the GTPase activity of the N-terminal cytoplasmic domains of atlastin-1 (residues 1-446). The $M^{347}E$ mutation was introduced into the soluble atlastin-$1^{1\text{-}446}$ construct, and its GTPase activity was determined by measuring the production of inorganic phosphate over time upon GTP hydrolysis at various protein concentrations.

atlastin-1$^{1–446}$ (Table 3.2.), and occur at a faster timescale than dimerization for reactions that do not undergo catalysis.

Using simple kinetic equations and our structural information (see Materials and methods and Appendix A), the time-resolved FRET data could be modeled using a molecular simulation, replicating the main features of the time-resolved FRET experiments (Figure 3.8.B). A two-state model describes well the data observed in the absence of hydrolysis. Addition of a third state representing a relaxed FRET constellation reproduces the appearance of a peak in the FRET data followed by a drop-off of the signal. These simulations corroborate our experimental observations, indicating that our interpretations provide a feasible framework.

Correlation between G and middle domain dimerization kinetics

Thus far, we defined the catalytic core of atlastin-1 and showed that nucleotide hydrolysis drives middle domain dimerization. Yet, considering the structural and FRET data, the question arises as to whether G domain dimerization precedes middle domain dimerization or occurs at a similar timescale. The two different scenarios have distinct implications for the molecular mechanism of atlastin-mediated membrane fusion and the role of GTP hydrolysis in the functional cycle. In the former model, GTP binding to atlastin would tether two opposing membranes via G domain dimerization, with the middle domains contributing to the interaction only subsequently following GTP hydrolysis, bringing the opposing membranes into closer proximity. In the alternative model, GTP hydrolysis would act as the timer for the formation of a tight tethering dimer, involving G and middle domains simultaneously.

Determining the sequence of G and middle domain dimerization will allow us to distinguish between these models.

To measure G domain dimerization, we mutated the sole cysteine in the middle domain ($C^{375}A$) and introduced a cysteine in the G domain at a non-conserved and solvent-exposed position ($K^{295}C$), which, based on all three dimeric crystal structures, would support FRET when labeled with appropriate fluorophores (Figure 3.10.A and B). These atlastin-1 mutants showed similar dimerization and GTPase characteristics as the wild-type proteins (Figure 3.10.C and D). Alexa dyes 488-C_5 maleimide (FRET donor) and 647-C_2 maleimide (FRET acceptor) were reacted with this mutant protein. FRET efficiency was measured based on changes in the donor fluorescence. Although we report a minor FRET signal in the case of GDP (efficiency of <10%), the drop in donor fluorescence was not accompanied by a rise in acceptor fluorescence (Figure 3.10.E). We interpret this result as a no-FRET state, consistent with the lack of dimerization in independent assays (e.g., Figure 3.4.). Importantly, in the presence of GppNHp and GDP•AlF_x, we observed a significant drop in donor fluorescence, with a concomitant rise in acceptor emission, indicating robust FRET. The extent of FRET was comparable in both samples (51% in GppNHp and 56% in GDP•AlF_x; Figure 3.10.F), corresponding to apparent distances of 55 and 54 Å, respectively. The discrepancy to the measured distance of ~32 Å (between Cβ positions of K^{295}) based on the crystal structures may be rationalized considering the linker length of the fluorophore (a C_5 linker for Alexa 488 and a C_2 linker for Alexa 647, which correspond to an additional ~8 and ~3 Å, respectively) and/or a minor fraction of monomeric protein.

Figure 3.10. Atlastin-1 G domain FRET using Alexa 488/647 dye-labeled proteins. (A) Experimental design of measuring G domain dimerization. Cartoon depiction of fluorescently labeled atlastin-$1^{1–446}$ in various crystallographic dimer conformations. Estimated distances between Cβ atoms of K^{295}, which is mutated to a cysteine for site-specific labeling, are based on the crystal structures shown in Figure 3.5.A. (B) SDS–PAGE of dye-labeled atlastin-$1^{1–446}$. Atlastin-1 mutants were first labeled with Alexa 488-C_5 Maleimide as described in Materials and methods. Two gels run side-by-side were loaded with 2.5 μg of indicated atlastin-1 proteins. One gel was stained with Coomassie brilliant blue (protein dye). The second, unstained gel was imaged upon excitation of the fluorophore. (C) Nucleotide-dependent dimerization of dye-labeled atlastin-$1^{1–446}$ proteins. SEC-MALS experiments were carried out and analyzed as in Figure 3.7.B. (D) GTPase activity of atlastin-$1^{1–446}$ mutant proteins used for dye labeling. GTPase activity was determined as shown in Figure 3.7.C. (E) Emission spectra of dye-labeled atlastin-$1^{1–446}$ mixtures at equilibrium. Alexa Protein (20 μM total, 1:20 ratio of donor to acceptor) was mixed with either buffer or nucleotide for at least 20 min prior to fluorescence measurement (apo, red dashed line; GDP, purple; GppNHp, green). (F) FRET efficiencies. FRET efficiencies of wild-type (black) and $R^{77}A$ mutant (white) calculated for dye-labeled atlastin-$1^{1–446}$ donor/acceptor mixtures in the presence of various nucleotides were carried out as stated in Materials and methods. (G) G domain-mediated FRET efficiency versus time of wild type and mutant $R^{77}A$ in the presence of GTP. Either wild-type (dark green) or mutant $R^{77}A$ (light green), dye-labeled atlastin-$1^{1–446}$ was mixed with an excess of GTP essentially as in (E). Emission spectra were measured right after mixing, every 2 min up to 10 min, at 15 min, and at 30 min. The sample was then spiked with additional GTP, mixed, and measured immediately. Lamp shutters were closed in between measurements. A black dashed line represents the FRET efficiency of wild-type FRET pair in the presence of GppNHp at equilibrium.

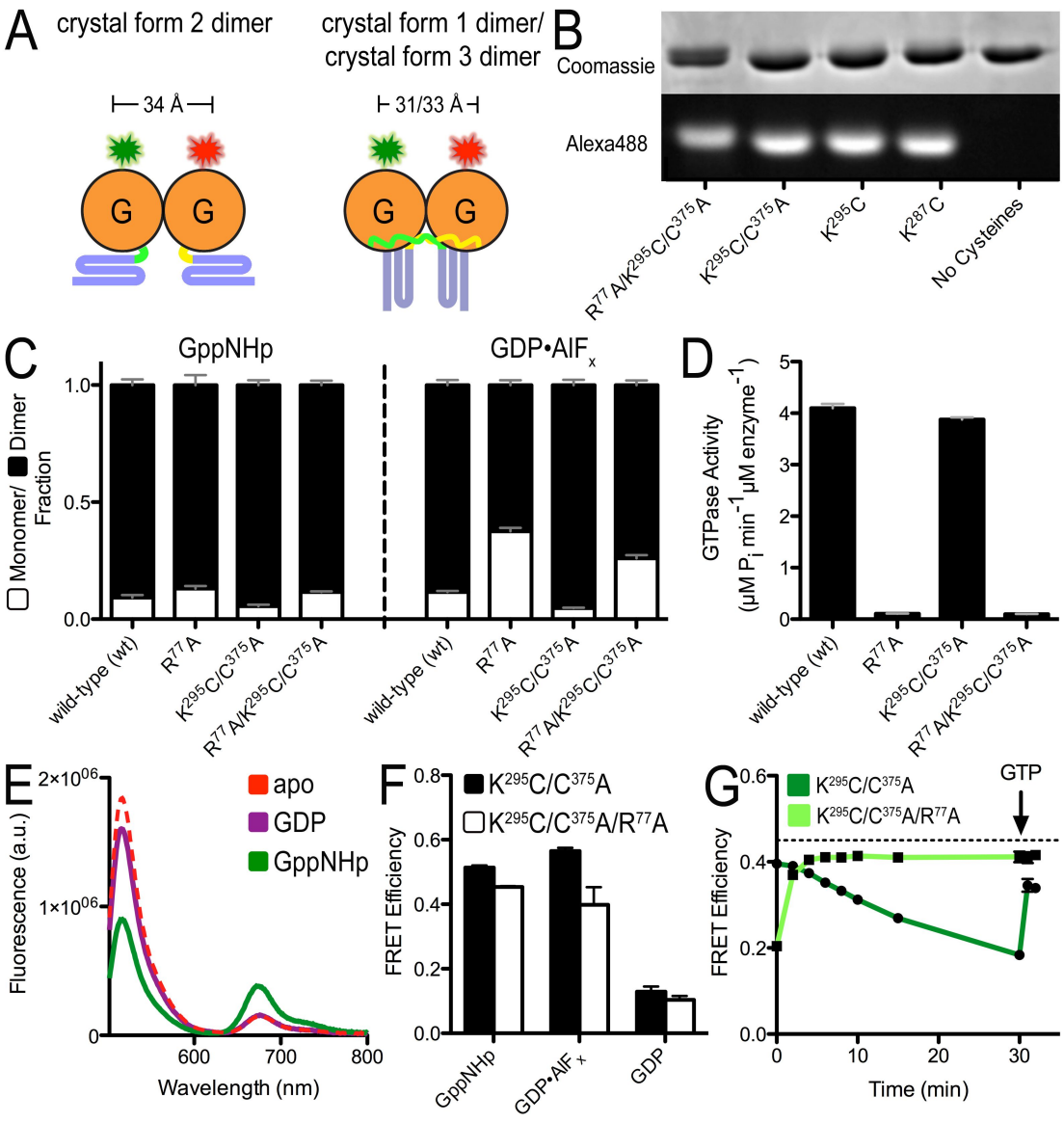
A
crystal form 2 dimer
crystal form 1 dimer/
crystal form 3 dimer
34 Å
31/33 Å
G
G
G
G
B
Coomassie
Alexa488
R77A/K295C/C375A
K295C/C375A
K295C
K287C
No Cysteines
C
GppNHp
GDP•AlFx
Monomer/ Dimer Fraction
1.0
0.5
0.0
wild-type (wt)
R77A
K295C/C375A
R77A/K295C/C375A
D
GTPase Activity
(μM Pi min-1 μM enzyme-1)
5
4
3
2
1
0
E
2×10^06
1×10^06
0
apo
GDP
GppNHp
Fluorescence (a.u.)
600
700
800
Wavelength (nm)
F
K295C/C375A
K295C/C375A/R77A
FRET Efficiency
0.8
0.6
0.4
0.2
0.0
GppNHp
GDP•AlFx
GDP
G
GTP
FRET Efficiency
0.6
0.4
0.2
0.0
0
10
20
30
Time (min)

In contrast to middle domain-mediated FRET that never achieved the same efficiencies in the presence of GTP as it did when mixed with GppNHp or the transition-state analogue (Figure 3.7.E and F), GTP binding to G domain-labeled atlastin-1 peaked at a comparable maximum value as all other dimerization-supporting conditions before FRET decreased again due to GTP hydrolysis (Figures 3.10.F and G). As before, the drop-off could be reversed by the addition of GTP (Figure 3.10.G). On the other hand, GTP-induced FRET via G domain dimerization of a catalytically inactive atlastin-1 variant ($R^{77}A$) rose to a maximum value over the course of 5 min and remained unchanged, approaching the steady-state FRET efficiency of catalytically competent atlastin-1 in the presence of GppNHp (Figure 3.10.G). Taken together, these observations suggest that G domains adopt an invariable, stable dimer, unlike the middle domains that appear to exist in equilibrium between different dimeric arrangements or populations.

Next, we assessed the kinetics of G domain dimerization, and compared it to those of middle domain-supported FRET. Interestingly, fluorescence changes in both the G domain and middle domain FRET pairs followed similar kinetics, with fast rises in FRET when mixed with GTP (second timescale), and slower kinetics when the catalytically dead mutant was used and/or in the presence of GDP•AlF_x, GppNHp, and GTPγS (minute timescale) (Figure 3.9. and 3.11.). Similarly to the middle domain dimerization kinetics, G domain dimerization is overall slower for the inactive $R^{77}A$ mutant compared to the catalytically active parent protein. Since nucleotide binding kinetics and affinities are similar for active and inactive proteins (Table 3.2.), it is likely that the arginine finger is involved in dimerization and/or allosteric switching of

atlastin-1.

These results indicate that the GTPase activity of atlastin is required to drive a conformational change allowing concomitant G and middle domain dimerization. Rather than bringing opposing membranes into close proximity via sequential steps, the entire N-terminal, cytoplasmic module acts as the tethering unit. Consequently, the tight-parallel dimer structures bound to GTP analogues (crystal form 3; Figure 3.5.) are likely depicting a post-hydrolysis state.

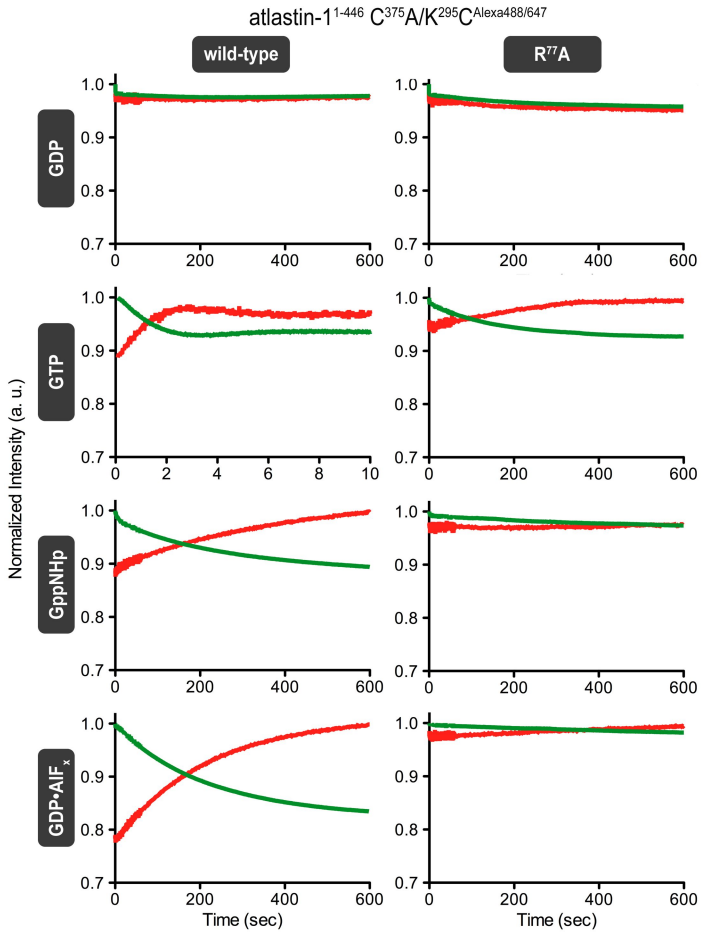

Figure 3.11. Rapid-mixing, stopped-flow kinetics of G domain-mediated FRET. Alexa 488 and 647-labeled atlastin-$1^{1–446}$ mixtures were prepared in a 1:1 ratio of donor to acceptor in a nucleotide-free buffer. Samples were mixed 1:1 with either buffer (apo) or buffer containing the indicated nucleotides (2 mM) using a stopped-flow apparatus. A xenon arc lamp was set to 493 nm excitation, and two photomultiplier tubes with appropriate filters in place were used to measure emission output over time.

The middle domain promotes GTP loading at the G domain and supports dimerization

If indeed the middle domain is released from the G domain prior to or concomitant with dimerization upon GTP hydrolysis, what is the relevance of the form 2 crystal structure, in which the middle domain folds back onto the G domain? Other observations not explained by the current model include the impaired GTPase activity of the isolated G domain, its inability to dimerize in the presence of any nucleotide, and its failure to act as a competitive inhibitor in membrane fusion (38, 39). Likewise, mutations that are predicted to impact the fold of the middle domain generate a non-functional protein, yet the exact mechanism remained elusive (37, 39).

A comparison of form 2 and 3 crystal structures highlights differences in the linker region and immediate docking site of the middle domain on the G domain, foremost the conformation of a central helix (residues 184–204; Figure 3.12.A). This helix is bent in form 2, providing a cradle for the middle domain, but is straight in form 3 occluding the middle domain-docking site. Spatially, it is adjacent to the nucleotide binding regions, which may indicate an overall regulatory role. We speculated that it might impact nucleotide binding, which could explain the aforementioned gaps in our mechanistic understanding. To test this hypothesis, we conducted nucleotide-binding assays using mant-labeled derivatives that change fluorescence upon interacting with protein (mant-GDP, mant-GTP, and mant-GppNHp). We noted that the isolated G domain binds mant-GDP readily with

Figure 3.12. Middle domain-mediated control of atlastin's GTPase activity. (A) Comparison of the G-middle domain interface in form 2 and form 3 crystal structures. The G domain of atlastin-1 is shown in orange except for switch regions (shades of blue) and residues 184–204 (dark red), which form a helix that changes its conformation between the form 2 and form 3 (or form 1) structures. In the GDP-bound form 2, the helix is bent to accommodate the first helix of the middle domain (blue with linker in green), while in the GDP•AlF_4^--bound form 3 (and GDP-bound form 1) structure, the helix straightens out, preventing this interaction. Nucleotide positions are indicated and shown as fuzzy spheres. (B) The G-middle domain interface in the form 2 crystal structure. The area of the structure boxed in red is shown, with the same coloring introduced in (A). Positions of point mutants used in (C) and (E) and the last residue of the truncated atlastin-1 construct (atlastin-$1^{1–366}$) are shown as sticks. (C) GTPase activity. The catalytic activity of atlastin-1 constructs 1–446, 1–339 (G), and 1–366 were measured. In addition, the effect of the isolated middle domain (M; residues 340–446) on the activity of the G domain was determined. Structure-guided mutants of the middle domain were included as well. (D) Effect of the middle domain on the nucleotide-dependent oligomerization of the G domain. SEC-MALS data for the isolated G domain (atlastin-$1^{1–339}$; left panel) alone or with addition of a 10× molar excess of the isolated middle domain (atlastin-$1^{340–446}$; right panel) in the presence of GppNHp are shown. The signal from the 90°-light scattering detector and refractive index detector is shown as colored, solid lines (G domain alone, green; G and M domains mixed, blue) and black, dashed lines, respectively (left Y axis). Average molecular weight calculations across the protein peak are shown as black circles (right Y axis). The theoretical molecular weight (based on primary sequence) for the monomer and dimer of the G domain, as well as the middle domain in the right panel, is shown as horizontal dashed lines. Proteins (30–40 μM) were incubated with nucleotides (2mM) at least 30min prior to SEC-MALS analysis. (E) Quantification of nucleotide-dependent dimerization of atlastin-1's G domain. SEC-MALS data for the indicated atlastin-1 constructs in the absence or presence of isolated middle domain variants are shown. Data for samples incubated with GppNHp or GDP•AlF_x are shown. The experimental approach and presentation was as in Figure 3.7.B.

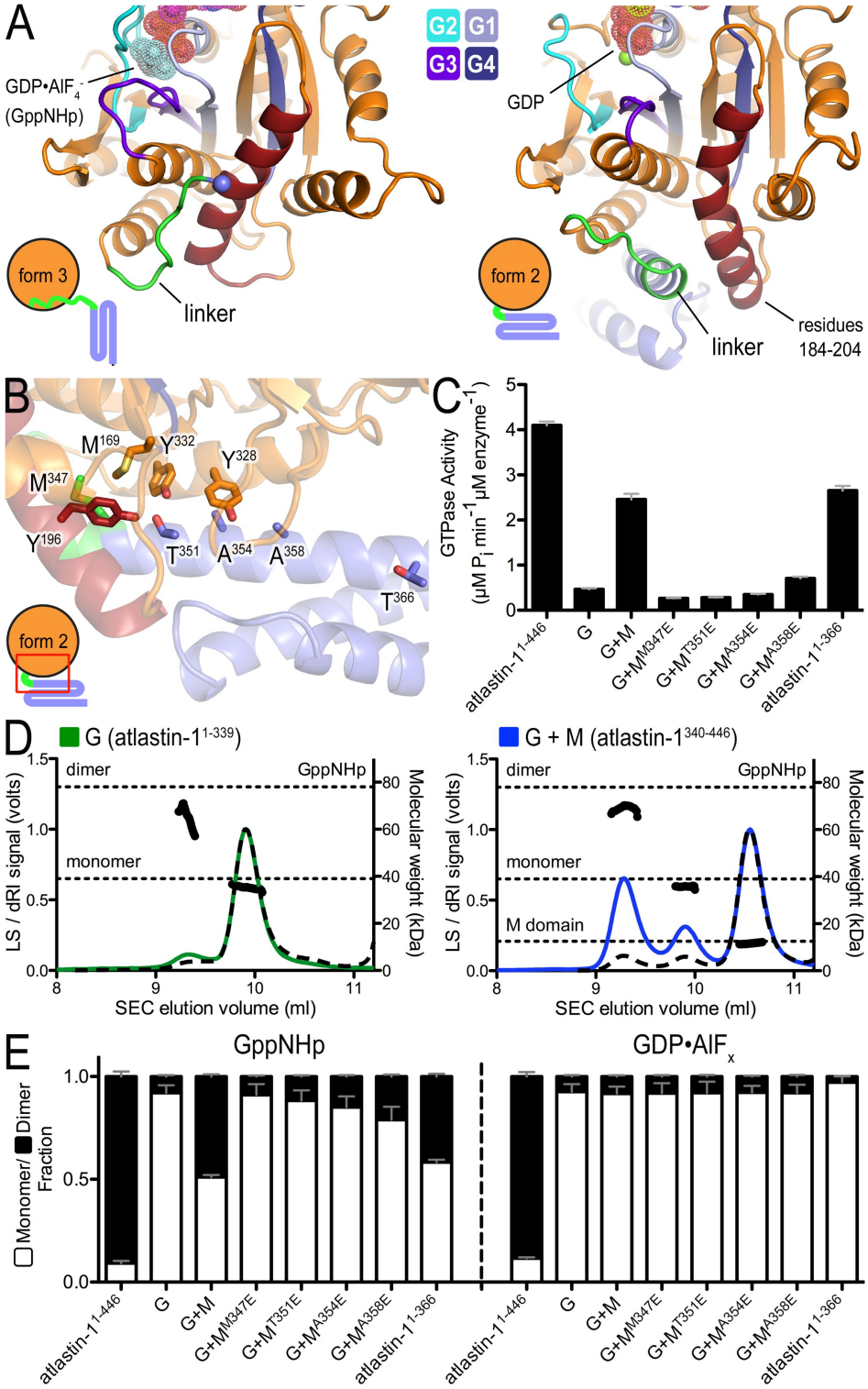
A
GDP•AlF4-
(GppNHp)
form 3
linker
G2 G1
G3 G4
GDP
form 2
linker
residues
184-204
B
M169
Y332
Y328
M347
Y196
T351
A354
A358
T366
form 2
C
GTPase Activity
(μM Pi min-1 μM enzyme-1)
atlastin-1 1-446
G
G+M
G+MM347E
G+MT351E
G+MA354E
G+MA358E
atlastin-1 1-366
D
G (atlastin-1 1-339)
G + M (atlastin-1 340-446)
dimer
monomer
M domain
GppNHp
LS / dRI signal (volts)
Molecular weight (kDa)
SEC elution volume (ml)
E
GppNHp
GDP•AlFx
Monomer/ Dimer Fraction

comparable kinetics as the construct also containing the middle domain (Table 3.2.). Yet, only the latter binds mant-GTP and the GTP-analogue mant-GppNHp, suggesting an influence of the middle domain on GTP loading.

As further corroboration, we used the separate G and middle domains (atlastin-$1^{1–339}$ and atlastin-$1^{340–446}$, respectively). In addition, we made a construct comprising the G domain and a short stretch of the first middle domain helix, which is buttressed by the G domain in our form 2 crystal structure (atlastin-$1^{1–366}$; Figure 3.12.B). First, we asked whether the middle domain has an effect on nucleotide binding of the isolated G domain, when it is added in trans. While the isolated G domain failed to bind mant-GTP (and mant-GppNHp) under the conditions used here, we observed a rescue of mant-GTP binding when the isolated middle domain was present, albeit with weaker affinity than the intact cytoplasmic unit (atlastin-$1^{1–446}$). A similar result was obtained with the protein that contained the truncated middle domain (atlastin-$1^{1–366}$), confirming the middle domain's role in GTP loading (Table 3.2.).

We predicted that efficient GTP loading is a prerequisite for GTPase activity, and hence we would expect an effect of the middle domain on catalysis. While the isolated G domain has close to background activity, similar to its *Drosophila* counterpart (38), co-incubation with the middle domain (10× molar excess over the G domain) yielded an activity of about five times the initial value (Figure 3.12.C). The middle domain truncation mutant leaving the G domain interaction region intact (atlastin-$1^{1–366}$) was also able to similarly rescue GTPase activity. No stimulation effect was seen when the middle domain was added to the entire N-terminal

cytoplasmic domain of atlastin, which includes the middle domain in the same polypeptide chain and has robust activity (data not shown).

Next, we asked whether the G-middle domain interface, which is unique to the form 2 crystal structure, is involved in the activation of the G domain, possibly as an allosteric site for nucleotide loading control (Figure 3.12.B). We introduced several single-point mutations into the isolated middle domain along this interface. Remarkably, mutant middle domains with changes across this largely hydrophobic surface were significantly impaired in the activation of the GTPase that was observed with addition of wild-type middle domain, and interestingly this effect was lessened the further from the top of the middle domain the mutant was located (Figure 3.12.B and C). Using middle domain titration experiments and the GTPase activity of the isolated G domain as the readout, we estimated that the wild-type middle domain associates with the G domain with an apparent affinity of 62.2 μM, whereas no stimulation was observed with a middle domain mutant ($M^{347}E$) across the entire concentration gradient (Figure 3.9.B). Likewise, the same mutation introduced into the construct comprising both G and middle domains affected nucleotide binding (Table 3.2.) and GTPase activity (Figure 3.9.C), corroborating the findings with the isolated domains.

Since GTP binding (and hydrolysis) facilitates G domain dimerization (see above), we assessed the dimerization propensity of the isolated domain in the absence and presence of the middle domain or its point mutants. When subjected to SEC-MALS-based analysis, the G domain alone elutes predominantly in a monomeric state in the presence of GppNHp (~8% dimer fraction) or GDP•AlF_x (no detectable dimer)

(Figures 3.12.D and E). In samples with 10× molar excess of wild-type middle domain, a large fraction of the G domain formed dimers in GppNHp (~49%), but not in GDP•AlF_x. Similar to their decreased effect on GTPase stimulation, middle domains with mutations in the G domain interface failed to induce G domain dimerization (Figure 3.12.E). Again, mutants further along the middle domain affected dimerization slightly less than those at the top of the middle domain. Notably, the dimer seen on the SEC-MALS trace corresponds to a G domain dimer alone, suggesting that the middle domain interaction with the G domain is rather transient and, based on our structural analysis, possibly incompatible with the GTP-bound conformation of the G domain (Figure 3.12.A).

In summary, we demonstrated a dual role for the middle domain in the reaction cycle of human atlastin-1 (Figure 3.13.). Initially, it is required for the efficient binding of GTP to the G domain via an intramolecular interaction, presumably by allosterically altering the conformation or dynamics of the switch regions, which could render the G domain more promiscuous for nucleotide binding (Table 3.2.). This role is important for atlastin's GTPase activity and dimerization of the G domains. Upon GTP binding, the middle domain dislodges from the G domain, likely involving a conformational change within the G domain imposing a steric clash with the middle domain. The middle domain then contributes to homotypic dimerization of atlastin. This transition is faster upon GTP hydrolysis, suggesting that hydrolysis could potentially occur in the context of a monomeric G domain. This notion is supported not only by the different timescales at which nucleotide binding and dimerization occur in the absence of hydrolysis, but also by the absence of apparent cooperativity in

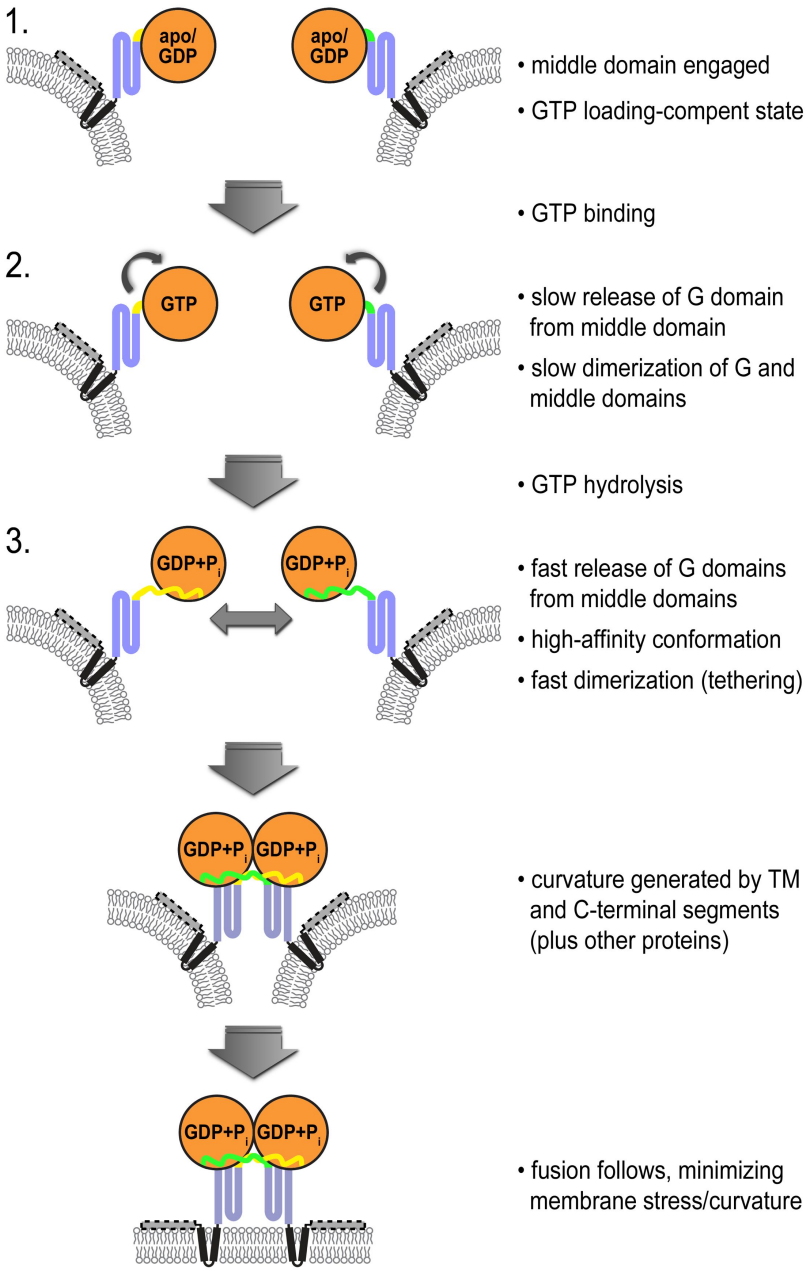

Figure 3.13. Model for atlastin-mediated membrane fusion. Atlastin begins in a form 2-like, GTP-loading-competent state with the middle domain engaging the G domain. GTP binding and hydrolysis drive rapid disengagement of the middle domain from the G domain, immediately followed by G and middle domain dimerization. Once in this tethering complex, membrane curvature and stress caused by atlastin's transmembrane domains and C-terminal amphipathic helix would allow fusion to occur spontaneously. Phosphate release follows, with relaxation and subsequent disassembly of the dimer. Other proteins that may interact with atlastin and contribute to membrane curvature, such as reticulons, are not shown.

the GTPase kinetics. GTPase rates appear slower than GTP binding and atlastin dimerization in GTP. Rather than indicating a requirement of G domain dimerization for enzymatic activity, the somewhat slower GTPase rate compared to both nucleotide binding and protein dimerization can be explained by the fact that we measure phosphate release in the activity assay, which may be rate limiting. We predict that the actual rate of hydrolysis is faster than the apparent rate we measured (Figure 3.6.B). As a side note, non-hydrolysable nucleotides or transition state analogues and likewise the catalytically inactive $R^{77}A$ mutant may only capture parts of the reaction cycle, while experiments under GTP-hydrolyzing conditions provide insight into the entire functional cycle and its timing.

CONCLUSIONS

While they have some common features, membranes of different cellular organelles are specialized environments that support particular biological functions. The ER is a prime example of this specialization, as lipids form an interconnected system of cisternae, vesicles, and tubules, which provides a highly compartmentalized structure for a multitude of biochemical processes. Its unique reticular structure has functional relevance, as mutations in atlastin-1, a protein involved in maintaining the ER's morphology by mediating homotypic membrane fusion (11, 15), are associated with hereditary, neurodegenerative disorders (6, 8). Interestingly, the majority of mutations cluster around the nucleotide binding site, and extend towards the site of intra-molecular interaction between the G and middle domains in the crystal form 2 dimer (20, 21). This observation in conjunction with our current data could indicate a

compromised allosteric network, which we would predict to couple middle domain interaction, GTP binding, and hydrolysis.

Our results suggest that membrane fusion follows a tethering step, involving the N-terminal cytoplasmic G and middle domains, which dimerize upon GTP binding and hydrolysis. This tight pairwise interaction would bring opposing membranes or membrane tubules into close proximity, the distance of which is critical since an increase in the length of the linker between the N-terminal module and the transmembrane segments impairs fusion (39). Once membranes are in close proximity, increased membrane curvature and stress mediated by the transmembrane helices and the amphipathic C-terminus of atlastin facilitate membrane fusion (38, 44, 45). By analogy to molecular mechanisms described for dynamin-mediated membrane fission (22, 29), membrane fusion may proceed spontaneously, probably upon release or relaxation of the tether. In that sense, the underlying principles of dynamin-mediated vesicle scission and atlastin-mediated membrane fusion appear to follow a conserved mechanism via G domain-regulated processes and implementation of protein domains or complexes that increase membrane curvature. While there are many parallels to be drawn between members of the dynamin superfamily, their differences pertain to their intrinsic control (e.g., self-assembly and catalytic mechanism), fine-tuning of the reaction (e.g., cooperativity and nucleotide exchange), and basic requirements that differ between fusion and fission. For example, unlike in atlastin, the isolated G domain of human GBP1 dimerizes readily in the presence of GTP and its analogues (18). Interestingly, GBP1 also shows cooperativity with regard to nucleotide hydrolysis, which relies on G domain dimerization, while atlastin apparently lacks this

mode of higher order regulation. Also, while membrane fission can originate from one membrane, fusion relies on bringing two opposing membranes into close proximity. While we cannot formally rule out a mechanism by which the N-terminal domains of atlastin dimerize on the same membrane (e.g., to further increase membrane curvature leading to the formation of three-way junctions in the ER), the observation that full-length, *Drosophila* atlastin is sufficient to facilitate proteoliposome fusion indicates a canonical fusion reaction (15). It remains to be seen whether other G proteins employ similar mechanism as we described here for atlastin, or if they are subject to unique modes of control.

REFERENCES

1. Fink JK (2006) Hereditary spastic paraplegia. *Curr Neurol Neurosci Rep* 6:65–76.

2. Salinas S, Proukakis C, Crosby A, Warner TT (2008) Hereditary spastic paraplegia: clinical features and pathogenetic mechanisms. *The Lancet Neurology* 7:1127–1138.

3. Polo JM, Calleja J, Combarros O, Berciano J (1991) Hereditary ataxias and paraplegias in Cantabria, Spain. An epidemiological and clinical study. *Brain* 114 (Pt 2):855–866.

4. Filla A et al. (1992) Prevalence of hereditary ataxias and spastic paraplegias in Molise, a region of Italy. *J Neurol* 239:351–353.

5. Depienne C, Stevanin G, Brice A, Dürr A (2007) Hereditary spastic paraplegias: an update. *Curr Opin Neurol* 20:674–680.

6. Zhao X et al. (2001) Mutations in a newly identified GTPase gene cause autosomal dominant hereditary spastic paraplegia. *Nat Genet* 29:326–331.

7. Namekawa M et al. (2006) SPG3A is the most frequent cause of hereditary spastic paraplegia with onset before age 10 years. *Neurology* 66:112–114.

8. Leonardis L, Auer-Grumbach M, Papić L, Zidar J (2012) The N355K atlastin 1 mutation is associated with hereditary sensory neuropathy and pyramidal tract features. *European Journal of Neurology*:no–no.

9. Evans K et al. (2006) Interaction of two hereditary spastic paraplegia gene products, spastin and atlastin, suggests a common pathway for axonal maintenance. *Proc Natl Acad Sci USA* 103:10666–10671.

10. Sanderson CM et al. (2006) Spastin and atlastin, two proteins mutated in autosomal-dominant hereditary spastic paraplegia, are binding partners. *Hum Mol Genet* 15:307–318.

11. Hu J et al. (2009) A Class of Dynamin-like GTPases Involved in the Generation of the Tubular ER Network. *Cell* 138:549–561.

12. Park SH, Zhu P-P, Parker RL, Blackstone C (2010) Hereditary spastic paraplegia proteins REEP1, spastin, and atlastin-1 coordinate microtubule interactions with the tubular ER network. *The Journal of clinical investigation*.

13. Namekawa M et al. (2007) Mutations in the SPG3A gene encoding the GTPase atlastin interfere with vesicle trafficking in the ER/Golgi interface and Golgi morphogenesis. *Mol Cell Neurosci* 35:1–13.

14. Rismanchi N, Soderblom C, Stadler J, Zhu P-P, Blackstone C (2008) Atlastin GTPases are required for Golgi apparatus and ER morphogenesis. *Hum Mol Genet* 17:1591–1604.

15. Orso G et al. (2009) Homotypic fusion of ER membranes requires the dynamin-like GTPase Atlastin. *Nature*.

16. Praefcke GJK et al. (2004) Identification of residues in the human guanylate-binding protein 1 critical for nucleotide binding and cooperative GTP hydrolysis. *J Mol Biol* 344:257–269.

17. Prakash B, Praefcke GJ, Renault L, Wittinghofer A, Herrmann C (2000) Structure of human guanylate-binding protein 1 representing a unique class of GTP-binding proteins. *Nature* 403:567–571.

18. Ghosh A, Praefcke GJK, Renault L, Wittinghofer A, Herrmann C (2006) How guanylate-binding proteins achieve assembly-stimulated processive cleavage of GTP to GMP. *Nature* 440:101–104.

19. Chappie JS, Acharya S, Leonard M, Schmid SL, Dyda F (2010) G domain dimerization controls dynamin's assembly-stimulated GTPase activity. *Nature*.

20. Bian X et al. (2011) Structures of the atlastin GTPase provide insight into homotypic fusion of endoplasmic reticulum membranes. *Proc Natl Acad Sci USA* 108:3976–3981.

21. Byrnes LJ, Sondermann H (2011) Structural basis for the nucleotide-dependent dimerization of the large G protein atlastin-1/SPG3A. *Proc Natl Acad Sci USA* 108:2216–2221.

22. Chappie JS et al. (2011) A Pseudoatomic Model of the Dynamin Polymer Identifies a Hydrolysis-Dependent Powerstroke. *Cell* 147:209–222.

23. Faelber K et al. (2011) Crystal structure of nucleotide-free dynamin. *Nature*:1–7.

24. Ford MGJ, Jenni S, Nunnari J (2011) The crystal structure of dynamin. *Nature*:1–6.

25. Gao S et al. (2011) Structure of Myxovirus Resistance Protein A Reveals Intra- and Intermolecular Domain Interactions Required for the Antiviral Function. *Immunity*:1–12.

26. Warnock DE, Hinshaw JE, Schmid SL (1996) Dynamin self-assembly stimulates its GTPase activity. *J Biol Chem* 271:22310–22314.

27. Stowell MH, Marks B, Wigge P, McMahon HT (1999) Nucleotide-dependent

conformational changes in dynamin: evidence for a mechanochemical molecular spring. *Nat Cell Biol* 1:27–32.

28. Zhang P, Hinshaw J (2001) Three-dimensional reconstruction of dynamin in the constricted state. *Nat Cell Biol* 3:922–926.

29. Bashkirov PV et al. (2008) GTPase Cycle of Dynamin Is Coupled to Membrane Squeeze and Release, Leading to Spontaneous Fission. *Cell* 135:1276–1286.

30. Pucadyil TJ, Schmid SL (2008) Real-time visualization of dynamin-catalyzed membrane fission and vesicle release. *Cell* 135:1263–1275.

31. Kenniston JA, Lemmon MA (2010) Dynamin GTPase regulation is altered by PH domain mutations found in centronuclear myopathy patients. *EMBO J*.

32. Liu Y-W et al. (2011) Differential curvature sensing and generating activities of dynamin isoforms provide opportunities for tissue-specific regulation. *Proc Natl Acad Sci USA*.

33. Song BD, Leonard M, Schmid SL (2004) Dynamin GTPase domain mutants that differentially affect GTP binding, GTP hydrolysis, and clathrin-mediated endocytosis. *J Biol Chem* 279:40431–40436.

34. Low H, Löwe J (2006) A bacterial dynamin-like protein. *Nature* 444:766–769.

35. Gasper R, Meyer S, Gotthardt K, Sirajuddin M, Wittinghofer A (2009) It takes two to tango: regulation of G proteins by dimerization. *Nat Rev Mol Cell Biol* 10:423–429.

36. Hu J, Prinz WA, Rapoport TA (2011) Weaving the Web of ER Tubules. *Cell* 147:1226–1231.

37. Morin-Leisk J et al. (2011) An intramolecular salt bridge drives the soluble domain of GTP-bound atlastin into the postfusion conformation. *J Cell Biol*.

38. Moss TJ, Andreazza C, Verma A, Daga A, Mcnew JA (2011) Membrane fusion by the GTPase atlastin requires a conserved C-terminal cytoplasmic tail and dimerization through the middle domain. *Proc Natl Acad Sci USA*.

39. Pendin D et al. (2011) GTP-dependent packing of a three-helix bundle is required for atlastin-mediated fusion. *Proc Natl Acad Sci USA* 108:16283–16288.

40. Otwinowski Z, Minor W (1997) Processing of X-ray diffraction data. *Meth Enzymol* 276:307–326.

41. Adams PD et al. (2002) PHENIX: building new software for automated

crystallographic structure determination. *Acta Cryst (2002) D58, 1948-1954 [doi:101107/S0907444902016657]*:1–7.

42. Emsley P, Cowtan K (2004) Coot: model-building tools for molecular graphics. *Acta Cryst (2004) D60, 2126-2132 [doi:101107/S0907444904019158]*:1–7.

43. Schrödinger GF (2010) The PyMOL Molecular Graphics System, Version~1.3r1.

44. Stefano G, Renna L, Moss T, Mcnew JA, Brandizzi F (2011) In Arabidopsis, the spatial and dynamic organization of the endoplasmic reticulum and Golgi apparatus is influenced by the integrity of the C-terminal domain of RHD3, a non-essential GTPase. *The Plant Journal* 69:957–966.

45. Liu TY et al. (2012) Lipid interaction of the C terminus and association of the transmembrane segments facilitate atlastin-mediated homotypic endoplasmic reticulum fusion. *Proc Natl Acad Sci USA* 109:E2146–54.

CHAPTER 4

STRUCTUAL SUPPORT OF AN INTRINSIC GTP LOADING MECHANISM IN HUMAN ATLASTIN-1

ABSTRACT

Atlastin related proteins belong to the superfamily of large, dynamin-related G proteins, which are involved in membrane fusion and fission events. Recent data identified atlastin as a fusion protein in the endoplasmic reticulum (ER), where it facilitates the formation of three-way junctions. Subsequent crystallographic studies yielded several high-resolution structures of human atlastin-1 in different nucleotide-bound states, revealing numerous conformations that the protein may sample during its nucleotide hydrolysis cycle. These, along with biochemical and biophysical evidence have begun to elucidate the molecular mechanisms of how atlastin proteins mediate homotypic membrane fusion. However, several aspects of atlastin regulation remain poorly understood. Here, we focus on the requirements for nucleotide binding and hydrolysis by using both reported and new structures as a guide. The crystal structure of wild-type atlastin-1's GTPase domain confirms the reliance of GTP binding on a previously discovered interaction between the GTPase and middle domains. A second structure of a mutated catalytic core fragment comprising the GTPase and middle domains of atlastin-1 bound to GDP shows atlastin in a monomeric form, revealing a more biologically relevant structural model for this state. Lastly, a mutational analysis gives insight into nucleotide loading and hydrolysis, as well as the importance of dimerization in the molecular mechanism of atlastin-1.

INTRODUCTION

In just over a decade, the family of atlastin GTPases has gone from a simple genetic locus identified in patients with a hereditary axonopathy, to having numerous high-resolution structures solved and cellular functions described (1-6). The human atlastin-1 gene was first found in patients suffering from a subtype of autosomal dominant Hereditary Spastic Paraplegia (HSP, subtype SPG3A) and was classified as a member of the dynamin superfamily of large GTPases (7). Subsequently, *in vivo* studies of atlastin-1 found that it was expressed predominantly in neurons of the central nervous system, where it localizes to the cis-Golgi, growth cones, and the endoplasmic reticulum (ER) (8-11). Two other mammalian isoforms (atlastin-2 and 3) were also identified, with more ubiquitous expression patterns (11). Like other dynamin family members, the atlastins exhibited GTPase activity and were found to self-associate (8, 9). Recent studies revealed atlastin's function as a membrane fusogen similar to mitofusins (also in the dynamin superfamily) as opposed to a membrane scission molecule, a reaction catalyzed by several other dynamin-related proteins (11-14). As major evidence, a knockdown of atlastin in *Drosophila melanogaster* caused ER fragmentation, while atlastin reconstitution into liposomes catalyzed fusion of proteoliposomes in the presence of GTP and magnesium (12). A loss of atlastin isoforms or expression of dominant-negative alleles in mammalian cells results in the loss of three-way junction in the reticular ER (11, 12, 14). A functional ortholog in *Saccharomyces cerevisiae*, Sey1p, is thought to have a similar role in yeast, a conjecture that was recently verified with both *in vivo* and *in vitro* experiments (14-18).

Structures of atlastin have since emerged, and provided a more detailed picture of its internal molecular mechanism (19-21). All structures solved to-date have been comprised of the N-terminal catalytic core fragment of atlastin, which consists of the GTPase and middle (helical) domains, ending just before the two transmembrane domains of the protein. The first structures revealed two intriguing conformations (19, 21), which we call form 1 and form 2. Both structures were bound to the nucleotide GDP, and their respective GTPase and middle domains have nearly identical conformations. Strikingly though, the position of the middle domain, which forms a three-helix bundle, differs by nearly a ninety-degree rigid-body rotation relative to the GTPase domain. In the case of the form 1 structure the middle domain does not interact with the GTPase domain, but in the form 2 structure it bends back onto the GTPase domain in a docked conformation. The crystal lattice symmetry also revealed a weak dimerization interface between two atlastin GTPase domains. This hinted at pre- and post-fusion conformations when the position of the middle domains was considered as membrane proximal points. Subsequently determined structures (collectively called form 3) bound to GTP or transition state analogs uncovered the molecular mechanism of GTP hydrolysis in atlastin's catalytic core fragment and revealed a much tighter, biologically relevant dimer interface that is also observed in solution (20). Furthermore, this study indicated an unanticipated dependence for nucleotide loading on an interaction between the GTPase and middle domains. Additionally, the dynamics of domain interactions during nucleotide binding and hydrolysis were monitored using Förster Resonance Energy Transfer (FRET). Together, a working model emerged where GTP binding to the G domain occurs

within an atlastin monomer, facilitated by the middle domain. GTP hydrolysis would introduce a coordinated conformational change allowing the G and middle domain to dimerize.

Despite these significant advances in the understanding of atlastin proteins, many of the details have yet to be uncovered and many questions remain. In particular, the available crystal structures rely on G domain dimers, even when the protein is bound to GDP, a nucleotide which does not support dimerization in solution (22, 23). To shed light on the conformation(s) of atlastin prior to dimerization, we obtained a crystal form in which the switch regions are not involved in crystal packing contacts, as is the case in all other structures determined to date. The resulting structural model and the biochemical characterization of structure-guided mutants provide additional insight into the nucleotide loading mechanism and the role of oligomerization in atlastin's GTPase activity, an essential part of its function as a membrane fusogen.

MATERIALS AND METHODS

Protein expression and purification

The catalytic core fragment (residues 1-446) and G domain (1-339) of human atlastin-1 were amplified by standard PCR and cloned into a modified pET28a expression plasmid (Novagen) yielding N-terminally hexahistidine-tagged SUMO fusion proteins. The hexahistidine-tagged SUMO-moiety was cleavable using the protease Ulp-1 from *S. cerevisiae*. Proteins were overexpressed in *E. coli* BL21 (DE3) cells (Novagen), which were grown in Terrific Broth (TB) media supplemented with 50 μg/ml kanamycin at 37°C. At an optical density corresponding to an absorbance of

0.8-1.0 at 600 nm (OD_{600}), the temperature was reduced to 18°C, and protein production was induced with 0.5 mM IPTG. After 16 hours, cells were harvested by centrifugation, resuspended in NiNTA buffer A (25 mM Tris-HCl, pH 8.5, 500 mM NaCl and 20 mM imidazole), and flash-frozen in liquid nitrogen.

After cell lysis by sonication and removal of cell debris by centrifugation, clear lysates were loaded onto NiNTA Superflow (Qiagen) equilibrated in NiNTA buffer A. The resin was washed with 20 column volumes of NiNTA buffer A, and proteins were eluted three times with 2 column volumes of NiNTA buffer A supplemented with 500 mM imidazole. Proteins were buffer exchanged into desalting buffer (25 mM Tris-HCl, pH 7.5, 400 mM NaCl, 5mM β-mercaptoethanol). Affinity tags were removed by incubation with the yeast protease Ulp-1 at 4°C overnight. Cleaved proteins were collected in the flow-through during NiNTA affinity chromatography, and were subjected to size exclusion chromatography on a Superdex 200 column (GE Healthcare) equilibrated in gel filtration buffer (25 mM Tris-HCl, pH 7.5, 100 mM NaCl). Proteins were concentrated on a Centricon ultrafiltration device (10 kDa cutoff; Millipore) to a final concentration of approximately 0.5-1 mM. Protein aliquots were flash frozen in liquid nitrogen and stored at -80°C.

Site-directed mutagenesis was carried out using Quikchange (Agilent) following the manufacturer's instructions, followed by validation through DNA sequencing.

Crystallization, data collection, and structure solution

Crystals were obtained by sitting drop vapor diffusion mixing equal volumes of protein (10–30mg/ml) and reservoir solution followed by incubation at 20°C. Initial crystals were obtained using atlastin-1 protein in gel filtration buffer in the presence of 2 mM GDP (Sigma) and 4 mM $MgCl_2$. Rectangular-shaped crystals belonging to space group $F2_3$ (atlastin-$1^{1–339}$) grew in reservoir solution containing 0.1M ammonium citrate tribasic pH7.0 and 12% PEG-3350. For cryo-protection, crystals were soaked in reservoir solution supplemented with 25% glycerol. For proteins crystallizing in space group P1 (atlastin-$1^{1–446}$-$R^{77}A$), the reservoir solution contained 0.2 M sodium malonate pH6.0, 20% PEG-3350. Crystals were cryo-protected by soaking in the crystallization solutions supplemented with 25% glycerol. Cryo-preserved crystals were flash-frozen and stored in liquid nitrogen. Data were collected on frozen crystals at 100 K.

Data reduction was carried out with the software package HKL2000 (24). Phases were obtained by Molecular Replacement (MR) methods by using the software package PHENIX (25) with the isolated G and middle domains of atlastin-1 as separate search models for MR. Refinement in PHENIX (25) and COOT (26) yielded the final models. Data collection and refinement statistics are summarized in Table 4.1. Illustrations were made in Pymol (27).

Size-exclusion chromatography-coupled multi-angle light scattering (SEC-MALS)

Purified protein (<2 mg/ml or 40 mM, injected concentration) was subjected to size-exclusion chromatography using a BioSep-SEC-S3000 column (Phenomenex)

equilibrated in SEC-MALS buffer (25 mM Tris-HCl, pH 7.5, 100 mM NaCl, 4 mM $MgCl_2$, and 2 mM EGTA). Where specified, wild-type or mutant atlastin-1 was incubated with GDP, GppNHp, or GDP•AlF_x (2 mM) for 30 min at room temperature prior to injection. The column was coupled to a static 18-angle light scattering detector (DAWN HELEOS-II) and a refractive index detector (Optilab T-rEX) (Wyatt Technology). Data were collected every second at a flow rate of 1 ml/min. Data analysis was carried out using the program ASTRA V, yielding the molar mass and mass distribution (polydispersity) of the sample. For normalization of the light scattering detectors and data quality control, monomeric BSA (Sigma) was used. Molecular weight distributions were determined by using the Multipeak Fitting Package in Igor Pro (WaveMetrics).

GTPase assay

GTPase activity was measured using the Enzchek Phosphate Assay kit (Molecular Probes) following the manufacturer's instructions. Measurements were carried out in a 96-well plate (Nunc) in a total volume of 250 µl. Recombinant wild-type or mutant atlastin-1 (at concentrations 0, 0.25, 0.5, 1, 2, and 4 µM) was combined with 1 U/ml purine nucleoside phosphorylase (PNP), 200 µM 2-amino-6- mercapto-7-methylpurine riboside (MESG), and provided buffer (20mM Tris–HCl, pH 7.5, 1mM $MgCl_2$, 0.1mM sodium azide). The plate was incubated at room temperature for 10 min, after which reactions were started by addition of 400 µM GTP (or alternatively, 50 mM Tris–HCl pH 7.5 for controls). Plates were assayed at 37°C in a Powerwave XS microplate reader (BioTek). Absorbance at 360 nm was monitored in 30 s intervals

for 30 min. Data were normalized to a phosphate standard curve, and initial velocities were calculated using the portion of the curve corresponding to the first 5% of consumed product. Data reported are means ± s.e.m. of three independent experiments.

N-Methylanthraniloyl (Mant)-nucleotide binding

On and off rates of mant nucleotides (mant-GppNHp, mant-GDP, or mant-GTP) were determined by measuring the change in fluorescence of the mant nucleotide over time upon mixing with atlastin-1 constructs. Using a Kintek stopped-flow apparatus (Kintek SF-2004), a final concentration of 2.5 μM mant-GDP, mant-GTP, or mant-GppNHp (Invitrogen) was mixed with increasing concentrations of atlastin-1 (10–50 μM). Mant fluorescence (λ_{exc} = 366 nm, emission filter HQ460/40M; Chroma) was measured and the first 500 ms of data were fit to a single-exponential decay curve. Observed rate constants from exponential fits were plotted versus protein concentration, with the resulting slope of the linear fit corresponding to k_{on}, and the y intercept to k_{off}. In parallel experiments, the off rate (k_{off} diss.) was also directly measured by preloading atlastin-1 proteins with mant nucleotide and chasing with a high concentration (2.5 mM) of unlabeled nucleotide (GDP). The first 500 ms of the resulting fluorescence decay curve was fit to a single-exponential decay, whose observed rate constant corresponds directly to the off rate (k_{off} diss.). All fits were performed using Prism 5 (GraphPad Software Inc.).

RESULTS AND DISCUSSION

Crystallization of the isolated GTPase domain bound to GDP

The purified GTPase domain of atlastin-1 (residues 1-339, Figure 4.1.) crystallized in a single crystal form bound to GDP (spacegroup $F2_3$). The structure, solved by molecular replacement, diffracted X-rays to a maximal resolution of 3.15Å with four protomers in the asymmetric unit (Table 4.1.). Crystals were grown in the presence of GDP and magnesium, and electron density for both of these moieties are present in each of the four protomers, though density was weaker for magnesium (Figure 4.1.A). The structure is generally well ordered, except for the surface exposed loop containing residues 114 through 117 for which electron density was not apparent, most likely due to disorder or multiple conformations. This loop comprises the switch 1 GTP-binding motif. Overall, the structure takes on a conformation most similar to that seen in the form 1, undocked middle domain crystal structure of the catalytic core fragment of atlastin (19), with significant overlaps in secondary structure (Figure 4.1.B, RMSD of 0.435Å).

The isolated GTPase domains of *Drosophila* atlastin and human atlastin-1 were shown in previous studies to have lost the ability to bind and therefore hydrolyze GTP (20, 23). The GTPase domain of human atlastin-1 is able to bind to GDP independently, but depends on the middle domain interaction observed in crystal form 2 to allow it to bind to GTP, and can catalyze its hydrolysis once bound (20). The crystal structure presented here of the GTPase domain of atlastin-1 in isolation presents some evidence as to why this occurs. Without the middle domain present and docked onto the GTPase domain, all helices involved in the interaction remain in the

positions observed in the form 1 structure suggesting this may be the "default" conformation of the GTPase domain when the middle domain is undocked. Similar to the form 1 structure, the nucleotide binding motifs take on a more closed conformation, in which F^{76} is positioned towards and above the nucleotide, effectively blocking the position that would be occupied by the gamma phosphate of GTP. In the form 2 structure (in which the middle domain is docked onto the GTPase domain) this residue swings into a more open conformation, though it still needs to move further to fully accommodate the gamma phosphate, as observed in the form 3 catalytically competent structure (Figure 4.1.C). The function of F^{76} will be further discussed in a later section, where we analyze the effect of mutating this residue.

Within the crystal, a dimer interface is apparent and resembles that of the form 1 structure. Towards the bottom of the dimer (where the middle domains would cross over in form 1) the dimer interface is looser (Figure 4.1.D) most likely due to the fact that the interactions between adjacent middle domains and linker regions are absent. Within the interface, a number of specific contacts between the molecules are preserved as in the form 1 structure, including that between R^{77} and E^{224}. However, like the first structures of atlastin-1 this dimer interface is most likely the result of a relatively high protein concentration within the crystal as well as preferred crystal packing interactions, since dimers are not observed in solution when the protein is bound to GDP.

Table 4.1. X-ray data collection and refinement statistics.

	Human atlastin-1 1-339, GDP	**Human atlastin-1 1-446, $R^{77}A$, GDP**
Data collection		
X-ray source	CHESS A1	CHESS A1
Wavelength (Å)	0.9771	0.9771
Space group	$F2_3$	P1
Unit cell parameters		
a, b, c, (Å)	307.95, 307.95, 307.95	51.1, 68.5, 75.7
α, β, γ (°)	90, 90, 90	63.3, 82.0, 80.9
Resolution range (Å)[a]	50-3.15 (3.26-3.15)	50-1.95 (2.02-1.95)
No. of reflections		
Total	1,037,464	149,932
Unique	41,762 (4,116)	62,895 (6,137)
Completeness (%)	99.95 (100)	95.93 (88.35)
Redundancy	24.8 (23.7)	2.4 (2.3)
I/σ (I)	27.13 (4.97)	7.12 (2.19)
R_{meas} (%)	14.1 (74.2)	8.1 (36.1)
Refinement		
R_{work}/R_{free} (%)	15.7/19.7	21.0/27.4
r.m.s. deviations		
Bond length (Å)	0.009	0.009
Bond angles (°)	1.21	1.27
No. of atoms	9,925	6,485
Protein	9,809	5,899
Ligands	116	58
Water	0	528
Ave. B-factors (Å^2)		
Protein	50.1	34.4
Water	31.1	38.3
Ramachandran (%)		
Favored	96	97
Outliers	0.5	0.41

[a]Values in brackets are for the highest resolution bin.

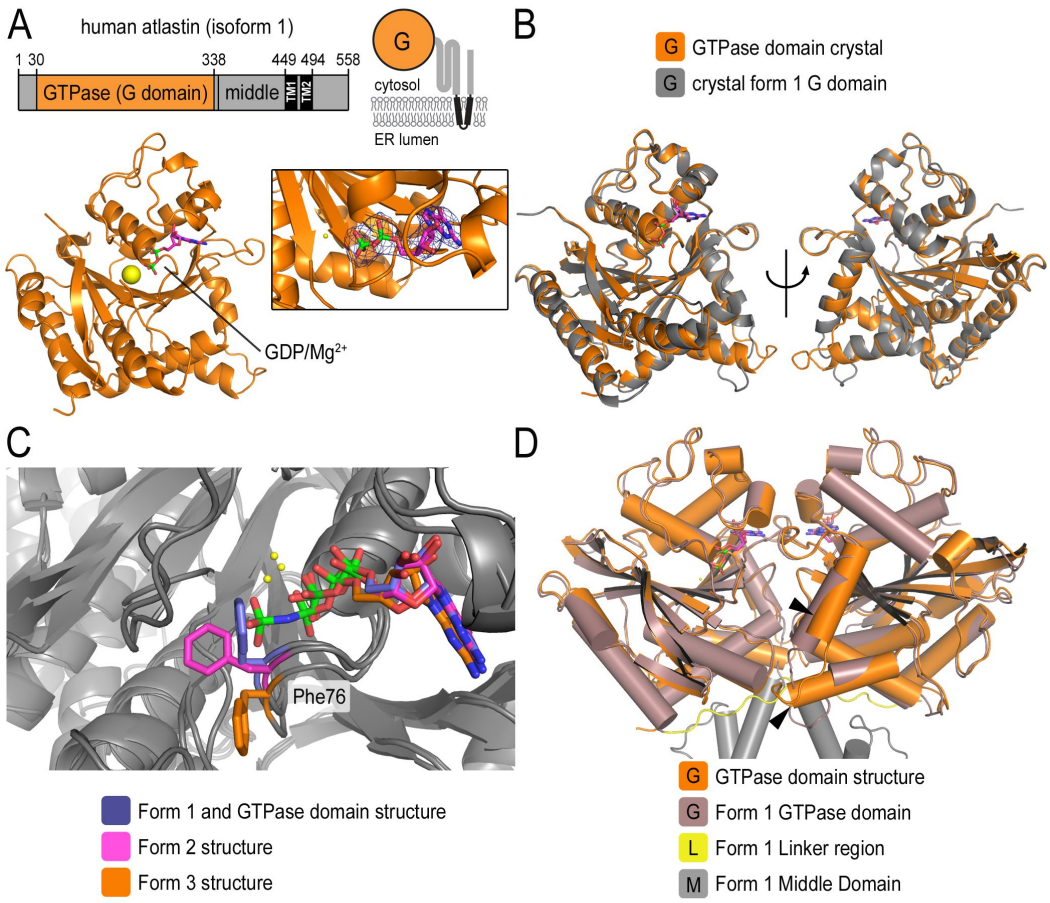

Figure 4.1. GTPase domain structure. (A) Domain organization of atlastin-1. The large G domain (orange) is connected to the middle domain by a short flexible linker and is followed by two transmembrane helices that span the membrane and a C-terminal domain. A topological model is shown (right panel). The fragment crystallized consists of residues 1–339 of human atlastin-1 (orange, lower panel). An inset displays a larger view of the binding pocket with GDP and magnesium, with an F_o–F_c omit map contoured at 4.0σ (B) Protomer overlay of the GTPase domain structure (orange) with crystal form 1 (grey) from (19). (C) Differing orientations of F^{76} (sticks, various colors) from atlastin-1 structures solved to-date. (D) Overlay of atlastin-1 GTPase dimer onto form 1 dimer structure (shown as cartoon cylinders). Black arrows indicate a region of secondary structure that shifts in the new structure due to lack of linker and middle domain interactions found in the form 1 structure.

Crystal structure of the arginine finger mutant bound to GDP

The catalytic core fragment containing the mutation $R^{77}A$ was purified and crystallized, resulting in a single crystal form bound to GDP and magnesium (spacegroup P1, two molecules/asymmetric unit; Table 4.1. and Figure 4.2.). Mutant

crystals diffracted X-rays to 1.95Å and the structure was solved using molecular replacement with the GTPase domain and middle domains from the form 2 structure (PDB ID code 3Q5E) as separate search models (19). Despite the high resolution of the acquired data, many surface exposed loops of the structure are disordered and remain absent from the model. These include residues 102-106, 112-117 (switch 1), 149-156 (switch 2), 338-339 (flexible, inter-domain linker), and 376-379 (loop connecting the first and second helices of the middle domain). The loop containing the $R^{77}A$ mutation is well ordered, and appears to take on the same conformation as it does in the form 2 crystal structure (Figure 4.2.B).

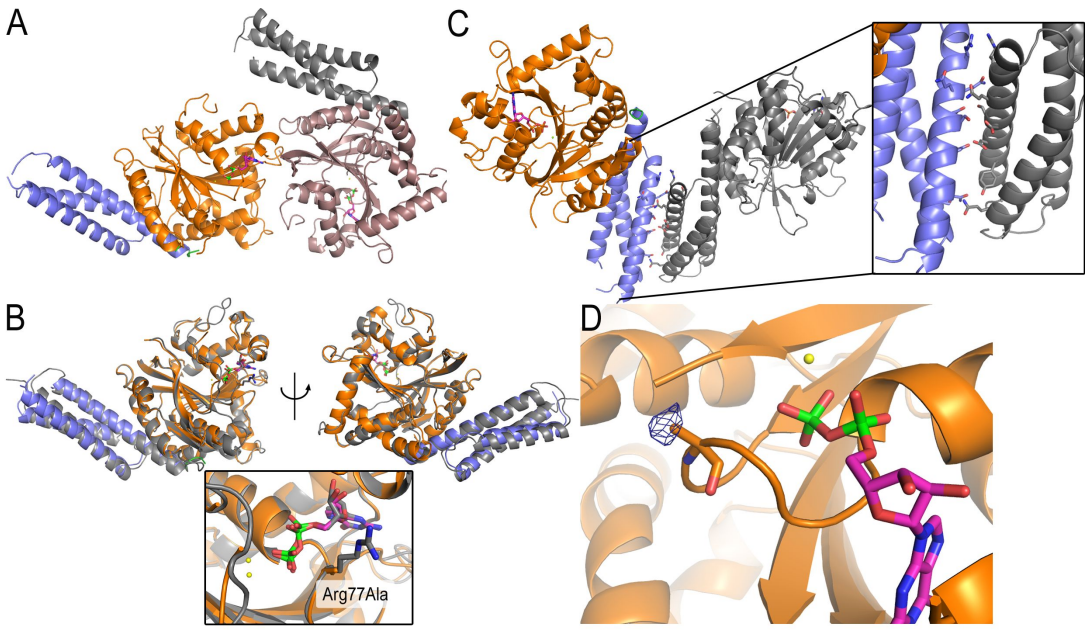

Figure 4.2. $R^{77}A$ structure. (A) Asymetric unit cell contents. (B) Protomer overlay of the $R^{77}A$ structure (orange and blue) with crystal form 2 (grey) from (19). Two views are shown (top and bottom). Inset shows an expanded view of binding pocket of the two aligned with the mutation and nucleotide displayed as sticks. (C) Middle domain interactions between unit cells. A protomer from one unit cell (colored orange and blue) and that of its neighboring unit cell (grey), with an inset to show the details of the interactions between residues in their middle domains. (D) Detailed view of F^{76}. Residue (shown as sticks) is modeled as an alanine with GDP and magnesium; an F_o–F_c omit map around the residue is contoured at 3.0σ.

One of the most noteworthy features of the structure is that it shows atlastin-1 in a monomeric state. There are no molecules in the asymmetric unit that form biologically relevant interfaces (28), and adjacent unit cells do not present any additional interactions with the protein's GTPase domain. In particular, the switch regions of the G domain, which are the elements that presumably change conformation in a nucleotide-dependent manner, are not involved in any interactions. Despite this, the overall conformation is very similar to that of the form 2 atlastin-1 structure (RMSD 0.819Å, Figure 4.2.). Like the form 2 structure, the middle domain docks against the GTPase domain, interacting with the same surfaces and residues. Interestingly, the middle domain three-helix bundle packs together in a slightly different way, with the third helix of the middle domain kinking at residue 415, which presumably causes the remaining two helices to adjust their positions. This minor change in angle is most likely a result of crystal packing interactions, as there are several significant points of contact between molecules in adjacent unit cells along the middle domain's third helix (Figure 4.2.) but could have some biological relevance. Other areas of the structure that vary between the $R^{77}A$ mutant and the form 2 structure include loops close to the dimer interface, several of which are disordered in the new structure. Considering the relatively large number of disordered regions (many of which are conserved and crucial parts of the protein) this structure would suggest that most of these loops are flexible in solution where the protein is monomeric and with the middle domain docked at the G domain. This would allow the protein to sample many conformations in solution. Notably, the F^{76} residue in the P-

loop has little electron density associated with it (difference density is limited to a small area around Cβ) suggesting multiple conformations (Figure 4.2.D).

Mutations in the P-loop and dimer interface perturb nucleotide binding, hydrolysis, and dimerization

Both the structures discussed above and those that have already been published have allowed us to design mutations in atlastin-1 that shed light onto the more detailed mechanisms of nucleotide binding as well as the role of dimerization in hydrolysis. Specifically, we targeted two residues in the GTPase domain of human atlastin-1 within the construct of the catalytic core fragment (amino acids 1-446). Mutants included F^{76} (located in the P-loop) mutated to either alanine or glycine, and E^{224} (located at the G domain dimer interface) mutated to either alanine or histadine (Figure 4.3.A). The first, F^{76} of the P-loop, is in close proximity to the nucleotide beta and gamma phosphate groups in the binding pocket. In the GDP bound structures it is positioned such that the gamma phosphate cannot be accommodated, suggesting it could play a role in gating this area of the binding pocket. Residue E^{224} forms cross-dimer interactions in all dimeric atlastin structures, including a salt bridge with R^{77} in those bound to GDP and hydrogen bonds in those bound to GTP and transition state analogs. All mutants expressed and purified with similar purity and stability as the wild-type. These four mutants were all tested for GTPase activity, oligomerization, and nucleotide binding.

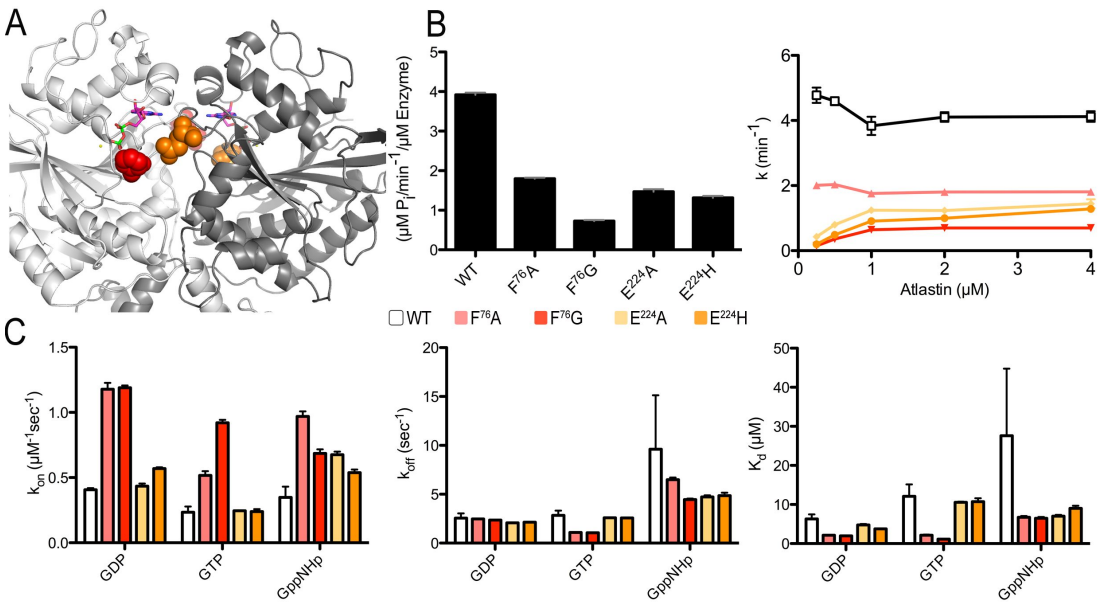

Figure 4.3. GTPase activity and nucleotide binding properties of atlastin mutants. (A) Position of mutants probing for nucleotide binding and dimerization properties of atlastin-1. The form 1 atlastin-1 dimer is shown. Mutant residues are shown as spheres, with those on the left protomer in red and the right protomer in orange (B) GTPase activity. GTPase activity was determined by measuring the production of inorganic phosphate upon GTP hydrolysis at various protein concentrations. (C) Nucleotide on rates (left), off rates (middle), and K_d (right) of mant-GDP, mant-GTP, and mant-GppNHp.

All four mutants exhibited a decrease in activity as tested in a velocity vs. enzyme concentration assay (Figure 4.3.B). The most severely affected mutant was $F^{76}G$, retaining less than a quarter of the wild-type activity. The remaining three mutants retained approximately one third of wild-type activity. Interestingly, the mutants located at residue E^{224} showed some non-linearity in the plot of activity vs. enzyme concentration, suggesting some degree of cooperativity may be present (Figure 4.3.B).

Next, oligomerization propensity in the presence of various nucleotides was tested using multi-angle light scattering coupled to a size exclusion column (SEC-MALS). All mutants tested were monomeric in their apo and GDP-bound forms

(Figure 4.4., red and purple traces, respectively). In the presence of the GTP analog GppNHp (green traces), all of the mutants exhibited a dominant, shifted peak that corresponded to the molecular weight of a dimer. The wild-type atlastin-1 catalytic core in the presence of GppNHp was also predominantly a dimer, with a very small (<5%) portion of the population running as a monomer. In both E^{224}A/H mutants, this monomeric species was slightly more populated. Lastly, in the transition state analog GDP•AlF_x, all mutants showed a single, monodisperse peak at the molecular weight corresponding to a dimer (Figure 4.4., orange traces). These results suggest that while the F^{76}A/G mutants do not perturb the dimer interface, both E^{224}A/H mutants seem to have some (if only a weak) effect on dimerization over a longer, near equilibrium timescale after nucleotide binding.

Finally, we assessed the binding kinetics of the different mutants for several nucleotides, in particular mant-GDP, mant-GTP, and mant-GppNHp. All four mutants were able to bind the three nucleotides tested, with both k_{on} and k_{off} measured directly and K_d calculated from these experimental values. Both F^{76}A/G mutants showed a higher affinity for all three nucleotides, especially GTP and GDP as a result of faster on-rates for these nucleotides and slower off-rates. Interestingly, differences in GTP on-rates correlated with the side chain length of residue 76, with phenylalanine showing the slowest on-rates, alanine showing an intermediated level and glycine showing the fasted on-rates of the three. The E^{224}A/H mutants in contrast, showed very little difference from wild-type values except for in mant-GppNHp, where the K_d was lower than wild-type due to a lower average k_{off} (Figure 4.3.C).

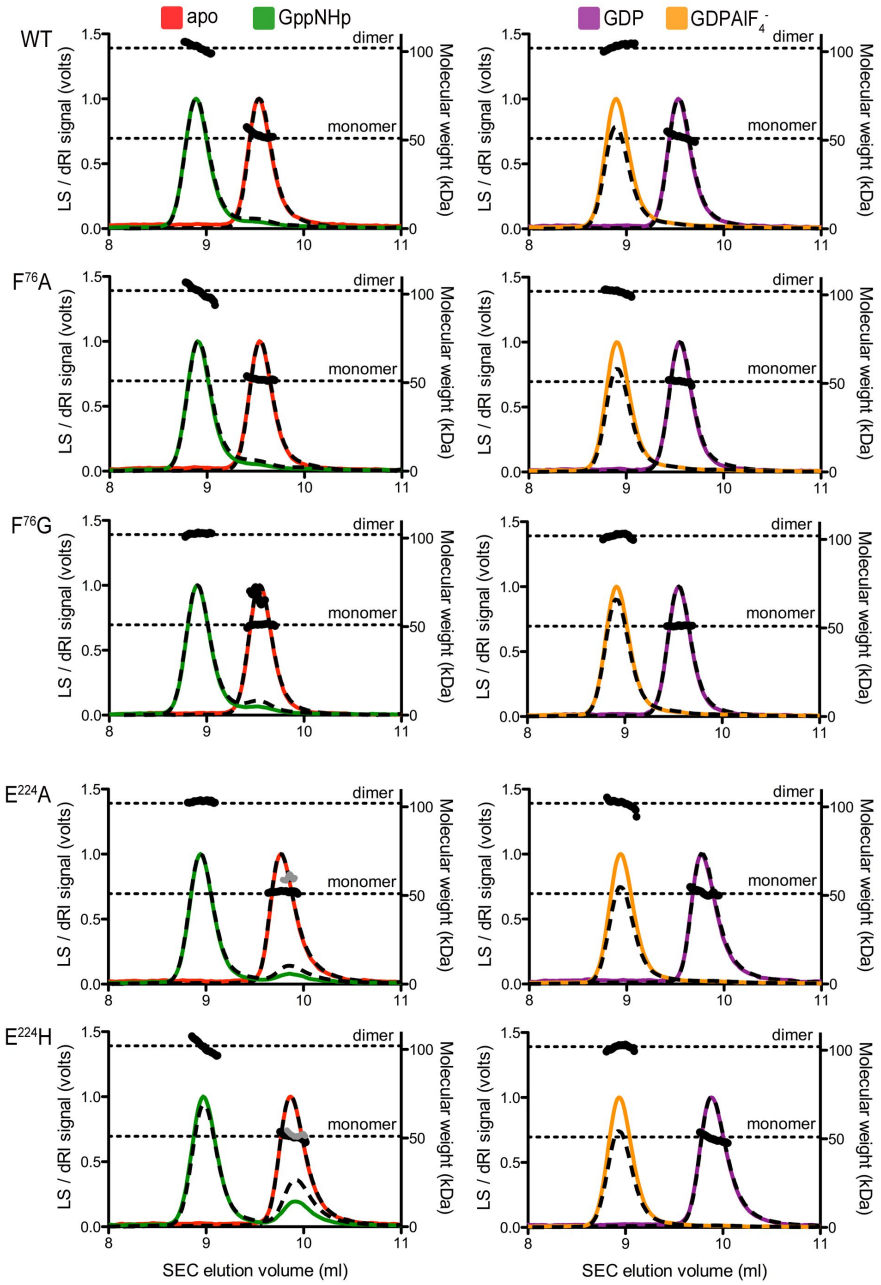

Figure 4.4. SEC-MALS for function-probing mutants. SEC-MALS of atlastin-1 WT, $F^{76}A$, $F^{76}G$, $E^{224}A$, or $E^{224}H$ nucleotide free (Left, red) or bound to GppNHp (Left, green), GDP (Right, purple), or GDP•AlF_x (Right, orange). Plotted on the left Y axis, the signal from the 90°-scattering detector and refractive index detector is shown in a solid colored line and a black dashed line, respectively. On the right Y axis, average molecular weight as calculated every second across the protein elution peak is shown as black circles for the major peak and grey circles for the second, minor peak (if present). Theoretical molecular weights based on primary sequence for the monomer and dimer are indicated as horizontal, dashed lines. Proteins (40 μM) were incubated with nucleotides (2 mM) prior to SEC-MALS analysis in a mobile phase lacking nucleotides.

All four mutants showed at least a two-fold decrease in GTPase activity, indicating they have some significant effect on hydrolysis. The first mutants, located at F^{76}, do not have any effect on the protein's ability to dimerize but both mutations of this residue drastically increased the binding affinity of mant-GDP and mant-GTP, with a more muted effect on the affinity for mant-GppNHp. In previously solved structures as well as the GTPase domain structure presented here, this phenylalanine takes on an important position within the enzyme. Along with F^{151} and two conserved glycines G^{74} (in the P-loop) and G^{149} (in the switch 2 motif), these two aromatic side chains form a "glycine brace", like those described for Ras-like GTPases (29), when the protein is in its form 2 conformation (Figure 4.5.). This interaction involves C–H-π interactions between F^{76}-G^{149} and F^{151}-G^{74}, which are both 4-4.5Å apart in the form 2 structure (consistent with this type of interaction (30)), but they are ~7-8Å apart in both the form 1 and new isolated GTPase domain structures. This form of structural stabilization would be lost upon mutation of F^{76} to alanine or glycine, and would allow the P-loop a greater degree of flexibility that could result in a faster nucleotide-binding on-rate, but also slow down hydrolysis by altering the kinetics of how the nucleotide binding motifs rearrange around GTP to form a tight and efficient binding pocket.

While it also shows a significant decrease in activity, the E^{224} mutant displays little change in nucleotide affinity and a minor defect in dimerization. More interesting is the potential cooperativity exhibited by these mutants, which would suggest they affect the K_d of dimerization in atlastin-1, and that dimerization is indeed important for its catalytic activity like other dynamin superfamily members. In the past, we have

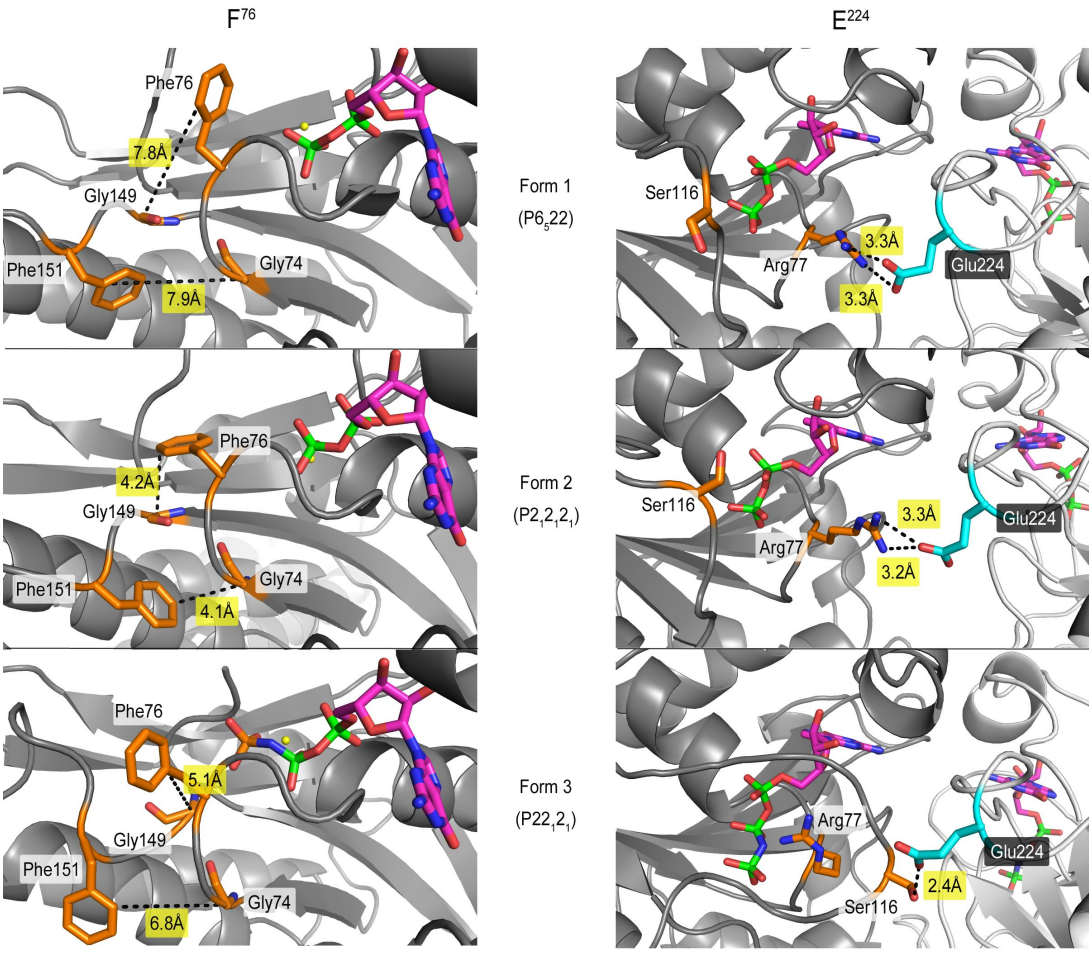

Figure 4.5. Intra- and intermolecular contacts of mutations. Structure-guided mutant positions and environments are shown for all three published crystal forms, including form 1 (top panels), form 2 (middle panels), and form 3 (bottom panels). Nucleotide, residues selected for mutation, and important residues in their vicinity are shown as sticks, with F^{76} illustrated on the left and E^{224} on the right. Displayed residues that are located on the main protomer (dark grey) are colored orange, and those on the opposing protomer (light grey) are colored in cyan. Residue names are labeled proximally, and residue distances (black, dashed lines) are displayed.

never observed cooperativity in the wild-type atlastin-1 catalytic core fragment, although it is possible that the K_d for dimerization is much lower than the concentrations that can be measured in our current assay (the lowest being 250 nM) making cooperativity difficult to detect. This residue (conserved in atlastins) makes cross-dimer contacts in both GDP-bound and GTP-bound structures. In form 1 and 2

structures, as well as our newest GTPase domain structure, E^{224} makes a salt bridge with R^{77} in the opposing dimer. Alternatively, in the form 3 structures (bound to either GppNHp or GDP•AlF_4^-) this residue instead contacts S^{116} in the opposing dimer with a hydrogen bond, pulling switch 1 into a position that covers the nucleotide-binding pocket. Disruption of this interaction and subsequent destabilization of nucleotide binding motif arrangement could lead to the reduction in hydrolysis efficiency observed for this mutant, although we did not see evidence for dimerization prior to hydrolysis in our previous FRET and GTPase activity results (20). Altogether, we have reported two novel atlastin-1 structures as well as mutagenesis data that enhance the working model of how the G domain may be activated by the middle domain and a potential role for cooperativity in hydrolysis.

CONCLUSIONS

The superfamily of dynamin-related GTPases has become an area of intense study, not only because of their involvement in diverse and important cellular functions, but also because many are implicated in human disease. Although they do share some commonalities in domain architecture and sequence, new evidence continues to show that they each have many unique characteristics as well. Atlastins are relatively new to this group and most of their molecular details only started being worked out in the last five years. As the furthest related member of the dynamin family, atlastins have proved themselves to be unique and interesting in their own right.

The two structures and mutagenesis experiments presented here provide more insight into these differences and add to our understanding of atlastin's function as a GTPase, which will help uncover the mechanism of its fusogenic activity in future studies. The GTPase domain takes on a form 1-like conformation, which could

represent the conformation found in solution of this domain alone. We have shown in the past that the interaction between the GTPase and middle domain observed in the form 2 crystal structure is indispensible for GTP loading and subsequent hydrolysis (20). This mode of regulation is unique in the atlastin subfamily. The second structure, that of the $R^{77}A$ mutant in the catalytic core of atlastin-1, presents a monomeric atlastin bound to GDP. This oligomeric state coincides with experiments done in solution, and could represent a better picture of how atlastin behaves in its monomeric, middle domain docked state. The numerous exposed, disordered loops in this structure are common in other structures of small GTPases, as well as some dynamin family protein structures especially in the absence of a gamma phosphate (31-33). This flexibility and dynamic movement of critical binding motifs is important for these proteins' overall function as nucleotide binding and hydrolysis machines.

In addition to these structures, our mutant data provide interesting clues for the role of two residues, F^{76} in the P-loop and E^{224} at the dimer interface. All four residues involved in the "glycine brace" discussed above (G^{74}, F^{76}, G^{149}, and F^{151}) are completely conserved in atlastins. Moreover, F^{151} is a known disease locus in patients with the neurodegenerative disorder Hereditary Spastic Paraplegia (HSP), highlighting the importance of this structural motif. E^{224} serves as a contact in all dimeric structures of atlastin-1 solved to-date. In GDP bound structures it pairs with R^{77} from the P-loop, while in GTP analog and transition state analog structures it forms a hydrogen bond with S^{116} from the opposite monomer's switch 1 (G2) motif that caps the nucleotide binding pocket after GTP is bound. The disruption of this contact results in the destabilization of the dimer itself, and lowered efficiency for hydrolysis possibly due to improper positioning of this important loop. While it still may be possible that atlastin-1 can hydrolyze GTP in its monomeric state, the efficiency of this event could be lowered dramatically without this and other cross-dimer contacts forcing the

binding pocket into the optimal position. Our current model shows atlastin first binding to GTP in a form 2-like state, and proceeding with hydrolysis just before dimerization of both GTPase and middle domains simultaneously. Minor alterations to accommodate these results, perhaps by bringing dimerization and hydrolysis into the same, simultaneous step could help reconcile our data with the current model. In data published recently by our lab, FRET based analysis showed that simultaneous dimerization by the GTPase and middle domains happens on a fast timescale only in conditions where GTP hydrolysis can occur. When a catalytically dead mutant or GTP analogs are used, dimerization does take place but on a much slower timescale (over the course of 10 minutes vs. 5 seconds). It's important to note that all other dynamin superfamily members rely on oligomerization to accelerate hydrolysis (34-40), though the possibility that atlastin could possess this and other unique molecular features should not be discounted.

REFERENCES

1. Park SH, Blackstone C (2010) Further assembly required: construction and dynamics of the endoplasmic reticulum network. *EMBO Rep*.

2. Renvoisé B, Blackstone C (2010) Emerging themes of ER organization in the development and maintenance of axons. *Current Opinion in Neurobiology* 20:531–537.

3. Blackstone C, O'kane CJ, Reid E (2011) Hereditary spastic paraplegias: membrane traffic and the motor pathway. *Nat Rev Neurosci* 12:31–42.

4. Moss TJ, Daga A, Mcnew JA (2011) Fusing a lasting relationship between ER tubules. *Trends Cell Biol*.

5. Hu J, Prinz WA, Rapoport TA (2011) Weaving the Web of ER Tubules. *Cell* 147:1226–1231.

6. Chen S, Novick P, Ferro-Novick S (2013) ER structure and function. *Curr Opin Cell Biol*:1–6.

7. Zhao X et al. (2001) Mutations in a newly identified GTPase gene cause autosomal dominant hereditary spastic paraplegia. *Nat Genet* 29:326–331.

8. Zhu P-P et al. (2003) Cellular Localization, Oligomerization, and Membrane Association of the Hereditary Spastic Paraplegia 3A (SPG3A) Protein Atlastin. *Journal of Biological Chemistry* 278:49063–49071.

9. Zhu P-P, Soderblom C, Tao-Cheng J-H, Stadler J, Blackstone C (2006) SPG3A protein atlastin-1 is enriched in growth cones and promotes axon elongation during neuronal development. *Hum Mol Genet* 15:1343–1353.

10. Namekawa M et al. (2007) Mutations in the SPG3A gene encoding the GTPase atlastin interfere with vesicle trafficking in the ER/Golgi interface and Golgi morphogenesis. *Mol Cell Neurosci* 35:1–13.

11. Rismanchi N, Soderblom C, Stadler J, Zhu P-P, Blackstone C (2008) Atlastin GTPases are required for Golgi apparatus and ER morphogenesis. *Hum Mol Genet* 17:1591–1604.

12. Orso G et al. (2009) Homotypic fusion of ER membranes requires the dynamin-like GTPase Atlastin. *Nature*.

13. Ferguson SM, Pietro De Camilli (2012) Dynamin, a membrane-remodelling GTPase. *Nat Rev Mol Cell Biol* 13:75–88.

14. Hu J et al. (2009) A Class of Dynamin-like GTPases Involved in the Generation of the Tubular ER Network. *Cell* 138:549–561.

15. Brands A (2002) Function of a Plant Stress-Induced Gene, HVA22. Synthetic Enhancement Screen with Its Yeast Homolog Reveals Its Role in Vesicular Traffic. *PLANT PHYSIOLOGY* 130:1121–1131.

16. Shibata Y et al. (2010) Mechanisms determining the morphology of the peripheral ER. *Cell* 143:774–788.

17. Anwar K et al. (2012) The dynamin-like GTPase Sey1p mediates homotypic ER fusion in S. cerevisiae. *J Cell Biol* 197:209–217.

18. Chen S, Novick P, Ferro-Novick S (2012) ER network formation requires a balance of the dynamin-like GTPase Sey1p and the Lunapark family member Lnp1p. *Nat Cell Biol* 14:1–11.

19. Byrnes LJ, Sondermann H (2011) Structural basis for the nucleotide-dependent dimerization of the large G protein atlastin-1/SPG3A. *Proc Natl Acad Sci USA* 108:2216–2221.

20. Byrnes LJ et al. (2013) Structural basis for conformational switching and GTP loading of the large G protein atlastin. *EMBO J*:1–16.

21. Bian X et al. (2011) Structures of the atlastin GTPase provide insight into homotypic fusion of endoplasmic reticulum membranes. *Proc Natl Acad Sci USA* 108:3976–3981.

22. Pendin D et al. (2011) GTP-dependent packing of a three-helix bundle is required for atlastin-mediated fusion. *Proc Natl Acad Sci USA* 108:16283–16288.

23. Moss TJ, Andreazza C, Verma A, Daga A, Mcnew JA (2011) Membrane fusion by the GTPase atlastin requires a conserved C-terminal cytoplasmic tail and dimerization through the middle domain. *Proc Natl Acad Sci USA*.

24. Otwinowski Z, Minor W (1997) Processing of X-ray diffraction data. *Meth Enzymol* 276:307–326.

25. Adams PD et al. (2002) PHENIX: building new software for automated crystallographic structure determination. *Acta Cryst (2002) D58, 1948-1954 [doi:101107/S0907444902016657]*:1–7.

26. Emsley P, Cowtan K (2004) Coot: model-building tools for molecular graphics. *Acta Cryst (2004) D60, 2126-2132 [doi:101107/S0907444904019158]*:1–7.

27. Schrödinger GF (2010) The PyMOL Molecular Graphics System,

Version~1.3r1.

28. Krissinel E, Henrick K (2007) Inference of macromolecular assemblies from crystalline state. *J Mol Biol* 372:774–797. Available at: http://www.ebi.ac.uk/pdbe/prot_int/pistart.html.

29. Neuwald AF (2009) The glycine brace: a component of Rab, Rho, and Ran GTPases associated with hinge regions of guanine- and phosphate-binding loops. *BMC Struct Biol* 9:11.

30. Weiss MS, Brandl M, Sühnel J, Pal D, Hilgenfeld R (2001) More hydrogen bonds for the (structural) biologist. *Trends Biochem Sci* 26:521–523.

31. Gabe Lee M-T, Mishra A, Lambright DG (2009) Structural Mechanisms for Regulation of Membrane Traffic by Rab GTPases. *Traffic* 10:1377–1389.

32. Hutagalung AH, Novick PJ (2011) Role of Rab GTPases in Membrane Traffic and Cell Physiology. *Physiological Reviews* 91:119–149.

33. Niemann HH, Knetsch ML, Scherer A, Manstein DJ, Kull FJ (2001) Crystal structure of a dynamin GTPase domain in both nucleotide-free and GDP-bound forms. *EMBO J* 20:5813–5821.

34. Gao S et al. (2011) Structure of Myxovirus Resistance Protein A Reveals Intra- and Intermolecular Domain Interactions Required for the Antiviral Function. *Immunity* 35:514–525.

35. Ghosh A, Praefcke GJK, Renault L, Wittinghofer A, Herrmann C (2006) How guanylate-binding proteins achieve assembly-stimulated processive cleavage of GTP to GMP. *Nature* 440:101–104.

36. Praefcke GJK et al. (2004) Identification of residues in the human guanylate-binding protein 1 critical for nucleotide binding and cooperative GTP hydrolysis. *J Mol Biol* 344:257–269.

37. Praefcke GJ, Geyer M, Schwemmle M, Robert Kalbitzer H, Herrmann C (1999) Nucleotide-binding characteristics of human guanylate-binding protein 1 (hGBP1) and identification of the third GTP-binding motif. *J Mol Biol* 292:321–332.

38. Kunzelmann S, Praefcke GJK, Herrmann C (2005) Nucleotide binding and self-stimulated GTPase activity of human guanylate-binding protein 1 (hGBP1). *Meth Enzymol* 404:512–527.

39. Gasper R, Meyer S, Gotthardt K, Sirajuddin M, Wittinghofer A (2009) It takes two to tango: regulation of G proteins by dimerization. *Nat Rev Mol Cell Biol* 10:423–429.

40. Gao S et al. (2010) Structural basis of oligomerization in the stalk region of dynamin-like MxA. *Nature* 465:502–506.

CHAPTER 5

CONCLUSIONS AND FUTURE DIRECTIONS

STRUCTURAL AND BIOCHEMICAL STUDIES OF ATLASTIN-1

Summary of findings

Membrane fusion is a complex but necessary function in every eukaryotic cell for tasks ranging from mitochondrial and ER fusion to exocytosis and endosomal trafficking. This biophysical phenomenon serves many vital purposes for maintaining cellular health with its importance epitomized in the diseases that result when these processes go wrong. SNAREs and viral fusion proteins were some of the first fusogens discovered and intensively studied, resulting in huge leaps in our understanding of how membrane fusion and dynamics work in general (1, 2). The atlastin proteins are relative newcomers to this field, with work on their molecular details beginning only about five years ago.

Studying the catalytic core of atlastin has resulted in numerous high-resolution crystal structures, revealing novel modes of regulation and intriguing conformational changes. Eight crystal structures in total have resulted in models for states bound to different forms of guanine nucleotide including GDP, GppNHp (a GTP analog), and GDP•AlF_4^- (a transition state analog). The first two structures were the first solved for atlastin, and were both bound to GDP (3, 4). However, there was a striking difference between the two structures that suggested they could represent pre- and post-fusion conformations. While this finding is still somewhat puzzling, the current hypothesis remains that the first structure (called form 1) is the post-hydrolysis, GDP-bound state, while the second (form 2) structure is an inhibited GDP-bound form. In the same study, we showed for the first time *in vitro* that the catalytic core of atlastin could dimerize upon binding to GTP and transition state analogs. This is somewhat at odds with previous findings of cellular extracts that suggested atlastin is a tetramer in the membrane (5-7),

however since our studies only use the N-terminal soluble portion of the protein, there is a possibility that oligomerization of atlastin could be different in the context of the full-length protein in the membrane. Additionally, GTPase activity was confirmed for the human isoform 1 of atlastin, having only been observed once before (8). Along with these biochemical characterizations of wild-type atlastin-1, we tested numerous HSP mutant forms of the protein and found several with deficiencies in their ability to dimerize or hydrolyze GTP, sheading some light onto disease pathogenesis.

These two initial structures, while informative, contained only a few clues about the catalytic mechanism of these proteins. We subsequently solved four nearly identical structures, two bound to the GTP analog GppNHp and two bound to the transition state analog GDP•AlF_4^-, that demonstrated how the conserved nucleotide binding motifs position themselves for GTP hydrolysis (9). The dimeric structures observed in all four crystals also proved to be biologically relevant, showing that an interaction between the GTPase and the middle domains contributes to a robust dimer interface. These structures added a new conformation (which we call form 3) to the two previously mentioned GDP-bound structures. From these, we designed a FRET-based assay system to detect the movements of the GTPase and the middle domains when they came into close proximity to another protomer. The results of these experiments forced us to reconsider the current model of atlastin-mediated fusion, which was originally based on the two crystal structures bound to GDP. In the original model, atlastin GTPase domains would bind GTP and dimerize, followed by GTP hydrolysis and a subsequent "power stroke" of the middle domain, bringing them and opposing membranes together. However, FRET data have revealed that both the GTPase and middle domains come together on approximately the same timescale. In addition, other groups working on atlastin found that the GTPase domain in isolation could not hydrolyze GTP efficiently and could not interact with itself (i.e. dimerize), which was also inconsistent with the model at the time. When we looked

carefully at all of the structures, the form 2 structure stood out because of an interaction region between the GTPase and middle domain. Separated GTPase and middle domain constructs mixed together rescued the ability of the GTPase domain to bind to GTP, hydrolyze it, and dimerize with itself. Moreover, mutations to the region where the GTPase and middle domain interact in the form 2 structure abolish this ability. From the compilation of this and all available data, we proposed a new model (9). This model (Figure 5.1.) starts with a monomeric atlastin GTPase domain, with the middle domain docked against it, as is observed in the form 2 structure. This conformation allows GTP to bind, and once this occurs the middle domain disengages the GTPase domain and both domains come together to dimerize in a form 3-like conformation. This tight dimer conformation would also bring together opposing membranes and with the help of the transmembrane domains and C-terminal amphipathic helix these membranes would fuse, followed by phosphate release and subsequent relaxation of the dimer (into a more form 1-like conformation, bound to GDP).

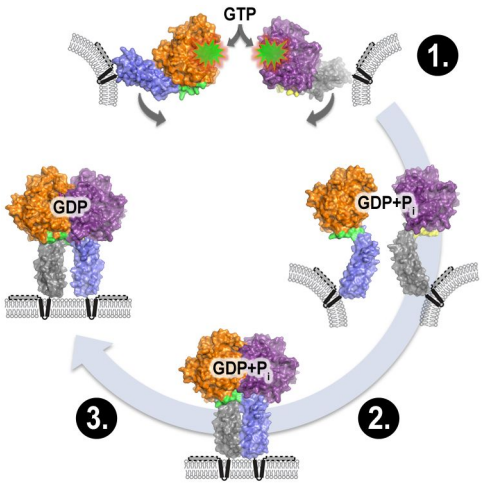

Figure 5.1. Working Model (9)**.** 1.) Atlastin begins in a form 2-like, GTP-loading-competent state with the middle domain engaging the G domain. 2.) GTP binding and hydrolysis drive rapid disengagement of the middle domain from the G domain, immediately followed by G and middle domain dimerization. Once in this tethering complex, membrane curvature and stress caused by atlastin's transmembrane domains and C-terminal amphipathic helix would allow fusion to occur spontaneously. 3.) Phosphate release follows, with relaxation and subsequent disassembly of the dimer.

The aforementioned crystal structures, three unique conformations in total, were novel contributions to the current understanding of atlastin proteins. In the midst of these discoveries, smaller pieces of the puzzle came together including the structures of the isolated GTPase domain and an arginine finger mutant, both bound to GDP. While these two structures did not present new conformations, they have added some details to the atlastin story. The GTPase domain structure resembles the conformation this domain takes on in the form 1 structure, suggesting that the form 2 conformation of the GTPase domain most likely arises only when in contact with the middle domain. The arginine finger mutant ($R^{77}A$) structure of the catalytic core fragment bound to GDP was the first structure not to crystallize in the typical dimerized GTPase domain conformation, a more biologically relevant state since no oligomerization is ever observed with atlastin bound to GDP. This mutation to the catalytic arginine finger is devoid of GTPase activity but retains its ability to dimerize when bound to GTP and transition state analogs, but it requires long incubation times since hydrolysis-driven conformational changes are impaired. Other functional mutants were also designed based on all of the structures solved to-date, including $F^{76}A/G$ (a mutation to the switch 1 GTP binding motif) and $E^{224}A/H$ (a dimer-interface mutant). All mutations reduced the activity of atlastin-1 by at least half, with the strongest mutation ($F^{76}G$) retaining less than 20% of wild-type activity. Despite this, both F^{76} mutants displayed an increase in nucleotide binding affinity, suggesting a type of "gate keeper" role for this bulky residue. The mutations to the dimer interface located at E^{224}, while they decrease the activity of the enzyme did not affect nucleotide binding rates or affinities. However, they did have a subtle effect on dimerization in the GTP analog GppNHp, and showed a small degree of cooperativity in the GTPase activity experiment, suggesting they could affect the affinity for dimerization of the enzyme and that dimerization is indeed important for catalysis.

Future directions

The atlastins represent a new and interesting family of proteins that catalyze membrane fusion in a way that has not yet been studied extensively. While the studies presented here contribute to the overall understanding of atlastin's molecular mechanism and internal regulation, many unanswered questions remain with regard to disease mutations, conformational changes, and full-length atlastin's behavior in the membrane.

The majority of HSP mutations occur on the soluble portion of atlastin-1, suggesting that they may impact the protein's fundamental enzymatic properties. However, many of the mutations tested in Chapter 2 had no effect on either GTPase activity or atlastin's ability to dimerize in response to nucleotide binding. To further investigate the effects of these mutations we can implement our newest experimental approaches such as the FRET assay presented in Chapter 3. The result of this assay will indicate whether or not the mutants allow the protein to perform the same type of conformational switching as the wild type, and whether or not the kinetics of this process are affected. In addition, a new version of the FRET assay that can monitor intramolecular interactions and conformational changes is currently being developed using non-natural amino acid incorporation (10) to introduce two distinct dyes onto the same protein (donor and acceptor) (Figure 5.2.). This assay will reveal which mutations affect the interaction between the GTPase and middle domains, an interaction necessary for GTP binding. In addition to FRET, mant-nucleotide binding experiments and analytical ultracentrifugation could uncover other defects previously undetected by our original methods. Once their effects on the soluble domain are clearer, addressing the outcome on atlastin in the context of the full-length protein will also be important to understanding disease pathogenesis.

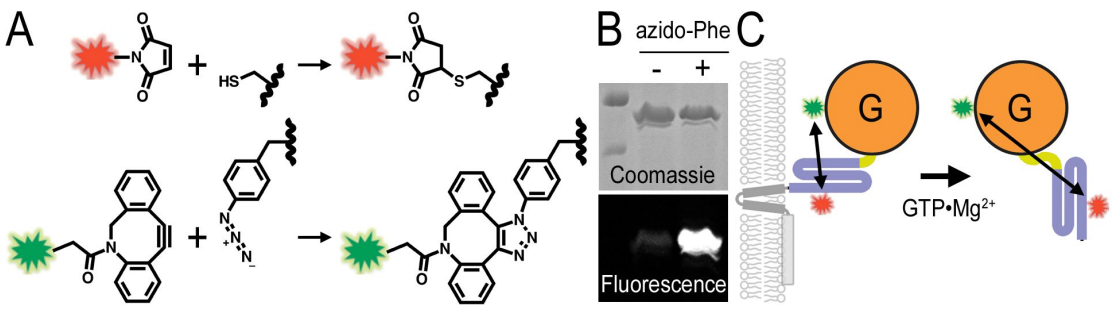

Figure 5.2. Protein labeling. (A) Labeling will proceed through thiol-modification on engineered cysteines (top; (9)) or click chemistry on incorporated azido-phenyl-alanine (bottom). (B) Click chemistry-based labeling of atlastin-1's catalytic core fragment. The wild-type protein without azido-phenylalanine did not label. (C) Strategy for measuring intra-molecular conformational changes.

The major lingering question in the study of atlastin proteins concerns whether or not molecular mechanisms established for the soluble domain apply to the full-length protein. For instance, does atlastin change its oligomeric state when going from a nucleotide-free or GDP-bound to a GTP-bound form? Do conformations observed in our crystal structures and confirmed in solution also take place during fusion? Early studies suggest that atlastin forms constitutive oligomers (tetramers) in the membrane, confounding our data on the soluble domain (5-7). Indeed, our initial purification and characterization efforts for full-length *Drosophila* atlastin revealed constitutive dimers in solution (Figure 5.3.B), and partial tetramerization upon addition of the GTP analog GppNHp. This additional degree of oligomerization has been suggested to occur through the transmembrane domains of atlastin, which would explain the apparent discrepancy with studies of the soluble domain. Regardless, these observations do not negate the possibility that the oligomerization interfaces observed in our structures are valid. Verification of these interactions and determination of participating domains are both necessary to compose a better picture of atlastin in the membrane. In the same way, conformational changes observed in the soluble domains must be confirmed or redefined in the full-length context. To accomplish this, FRET probes can still be used in

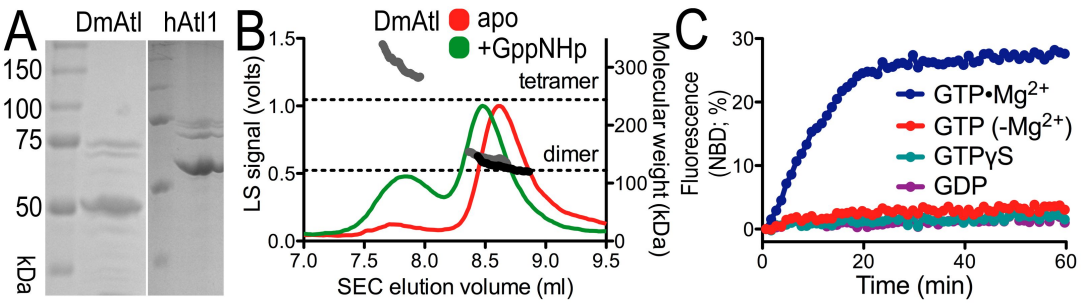

Figure 5.3. Purified, full-length atlastin. (A) SDS-PAGE of *Drosophila* and human atlastin (expressed in *E.coli*) prior to gel filtration. (B) SEC-MALS analysis of *Drosophila* atlastin in detergent micelles with (green) and without (red) GppNHp. A shift in the dimer peak may indicate a conformational change. Grey and black symbols across the protein peaks indicate absolute molecular weights determined by MALS. (C) Reconstituted membrane fusion (assay established by the McNew group (11)).

reconstituted lipid systems to monitor domain motions as was done for the soluble domain. Another approach would be to use electron microscopy (EM) to reconstruct full-length atlastin as has been done for the G-protein coupled receptor, β_2-adrenergic receptor in complex with its heterotrimeric G-protein complex (12). This approach has been shown to work for the soluble domain of atlastin by ours (Figure 5.4.) as well as another group (13), and will uncover important details on the overall structure while efforts for crystallizing the full-length protein continue.

During the time of this thesis, new details have emerged regarding the requirements for fusion activity of full-length atlastin from *Drosophila melanogaster*. Perhaps most obviously, early experiments confirmed a requirement for GTP hydrolysis (11). More interestingly, fusion of membranes *in vitro* was nearly abolished without atlastin's C-terminus, but could be rescued by adding it *in trans* (5, 14). This part of atlastin was thought to be unstructured, but a more detailed analysis suggests that it most likely forms an amphipathic helix that dips into the membrane and causes local membrane curvature and disruption to lipid order. The same study revealed that the specific sequence of atlastin's transmembrane domains was also important for fusion activity. Other studies have also demonstrated a necessity for dimerization through the middle domain to achieve

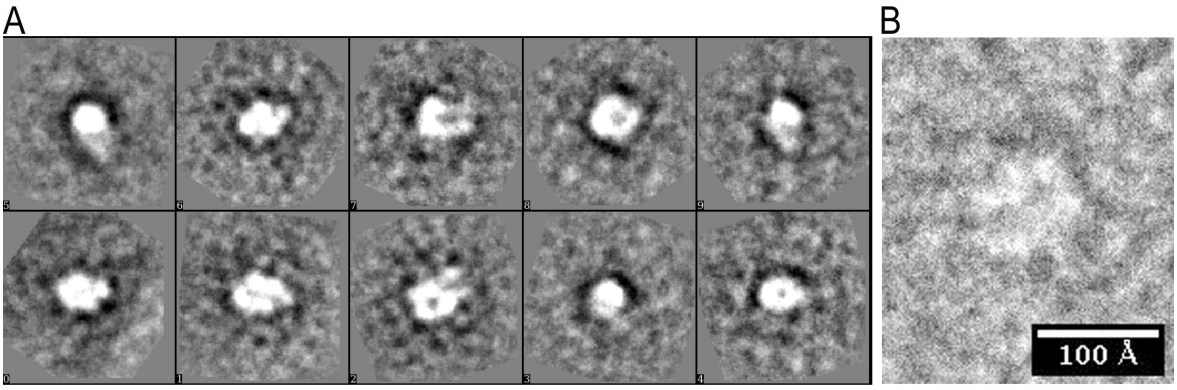

Figure 5.4. Atlastin-1 TEM class averages. (A) Sample class averages (showing various orientations) of atlastin-1 soluble domain bound to GppNHp. Two lobes are visible in most images, consistent with crystal structures of this nucleotide-bound state. Images were compiled from approximately 500 particles, using negative stain TEM on the FEI Tecnai F20 in Cornell's NBTC. (B) Raw particle image showing the scale of the particles is similar to those found in the crystal structures.

fusion (14, 15). To better understand how this family of proteins catalyzes membrane fusion, additional studies to work out the timing of domain interactions and conformational changes during this process must move forward. Several labs (including our own) have successfully purified full-length, recombinant *Drosophila* atlastin protein and have confirmed that it is competent for GTP-dependent membrane fusion when reconstituted into liposomes in an assay established by the McNew lab (11) (Figure 5.3.C). Full-length human atlastin-1 can be purified similarly, but attempts to demonstrate fusion activity have been unsuccessful so far. While the other two isoforms have yet to be tested, the fact that atlastin-1 cannot fuse membranes *in vitro* is puzzling. Though we simply may not have determined the correct environmental requirements for human atlastin-1 to catalyze fusion, another possibility is that it has lost this ability over the course of evolution. Perhaps only one or two of the three human isoforms has retained its ability to fuse membranes, leaving the remaining redundant copy(ies) to perform other, more specific functions. Human atlastin-1 is not expressed ubiquitously like the other two isoforms and is mainly found in neurons, leaving this explanation as a distinct possibility (6, 7). *Drosophila* only have a single atlastin isoform, therefore the essential function of fusing ER tubules must be

retained considering the lack of redundancy in the system. For these reasons it is necessary to expand the techniques used here to other isoforms and homologs to gain a better understanding of what qualities are necessary for fusion-competent atlastins. At the same time, determining atlastin-1's role in the cell via other cell biological and biochemical methods should be pursued. Two hereditary neuropathies caused by atlastin-1 mutations give a not-so-subtle hint of its necessity to these highly specialized and essential cells. Future research combined with the knowledge outlined here may ultimately lead to new treatments and a better understanding of axonopathies in general, carving a path to prevent these devastating diseases.

REFERENCES

1. Martens S, McMahon HT (2008) Mechanisms of membrane fusion: disparate players and common principles. *Nat Rev Mol Cell Biol* 9:543–556.

2. Kozlov MM, McMahon HT, Chernomordik LV (2010) Protein-driven membrane stresses in fusion and fission. *Trends Biochem Sci* 35:699–706.

3. Byrnes LJ, Sondermann H (2011) Structural basis for the nucleotide-dependent dimerization of the large G protein atlastin-1/SPG3A. *Proc Natl Acad Sci USA* 108:2216–2221.

4. Bian X et al. (2011) Structures of the atlastin GTPase provide insight into homotypic fusion of endoplasmic reticulum membranes. *Proc Natl Acad Sci USA* 108:3976–3981.

5. Liu TY et al. (2012) Lipid interaction of the C terminus and association of the transmembrane segments facilitate atlastin-mediated homotypic endoplasmic reticulum fusion. *Proc Natl Acad Sci USA* 109:E2146–54.

6. Rismanchi N, Soderblom C, Stadler J, Zhu P-P, Blackstone C (2008) Atlastin GTPases are required for Golgi apparatus and ER morphogenesis. *Hum Mol Genet* 17:1591–1604.

7. Zhu P-P et al. (2003) Cellular Localization, Oligomerization, and Membrane Association of the Hereditary Spastic Paraplegia 3A (SPG3A) Protein Atlastin. *Journal of Biological Chemistry* 278:49063–49071.

8. Zhu P-P, Soderblom C, Tao-Cheng J-H, Stadler J, Blackstone C (2006) SPG3A protein atlastin-1 is enriched in growth cones and promotes axon elongation during neuronal development. *Hum Mol Genet* 15:1343–1353.

9. Byrnes LJ et al. (2013) Structural basis for conformational switching and GTP loading of the large G protein atlastin. *EMBO J*:1–16.

10. Chin JW et al. (2002) Addition of p-Azido- l-phenylalanine to the Genetic Code of Escherichiacoli. *J Am Chem Soc* 124:9026–9027.

11. Orso G et al. (2009) Homotypic fusion of ER membranes requires the dynamin-like GTPase Atlastin. *Nature*.

12. Westfield GH et al. (2011) Structural flexibility of the G alpha s alpha-helical domain in the beta2-adrenoceptor Gs complex. *Proc Natl Acad Sci USA* 108:16086–16091.

13. Morin-Leisk J et al. (2011) An intramolecular salt bridge drives the soluble domain

of GTP-bound atlastin into the postfusion conformation. *J Cell Biol*.

14. Moss TJ, Andreazza C, Verma A, Daga A, Mcnew JA (2011) Membrane fusion by the GTPase atlastin requires a conserved C-terminal cytoplasmic tail and dimerization through the middle domain. *Proc Natl Acad Sci USA*.

15. Pendin D et al. (2011) GTP-dependent packing of a three-helix bundle is required for atlastin-mediated fusion. *Proc Natl Acad Sci USA* 108:16283–16288.

APPENDIX A

MODELING OF THE TIME-RESOLVED FRET DATA.

Dimerization kinetics

For time-dependent FRET simulations, we propose a simple three-state model based on the available structural information: a monomeric non-FRET state M, an initial dimerization state D_1, and a possible "relaxed" dimer state D_2. We assume that the dynamics of nucleotide binding is sufficiently fast as to not significantly contribute to apparent dimerization and FRET behavior and is therefore ignored. Dimerization is modeled by the 2nd order kinetic equation:

$$\frac{d[D]}{dt} = k_{on}[M]^2 - k_{off}[D]$$

Where [D] is the dimer concentration, [M] is concentration of free monomers, k_{on} is the rate constant for dimerization, and k_{off} is the rate constant for dissociation. The two populations are related by the mass conservation equation:

$$[M_0] = [M] + 2[D]$$

Where $[M_0]$ is the initial monomer concentration at time equals 0 and the initial dimer concentration ($[D_0]$) equals 0. The monomer concentration as a function of time ([M(t)]) can be modeled numerically by discretizing the kinetic equation above:

$$\Delta[D(\Delta t_n)] = \left(k_{on}[M(\Delta t_n)]^2 - k_{off}[D(\Delta t_n)]\right)\Delta t$$

$$[M(\Delta t_{n+1})] = [M(\Delta t_n)] - 2\Delta[D(\Delta t_n)]$$

Where Δt is the discretized time interval, and the subscript n indicates the nth interval such that $t = n\Delta t$. The dimer concentration [D] is modeled similarly.

However, with the incorporation of a second possible "relaxed" dimer state, the populations are determined by:

$$[D_1(\Delta t_{n+1})] = [D_1(\Delta t_n)]\left(1 - k_{off}\Delta t - k_{12}\Delta t\right) + [M(\Delta t_n)]^2 k_{on}\Delta t$$

$$[D_2(\Delta t_{n+1})] = [D_2(\Delta t_n)]\left(1 - k_{off}\Delta t\right) + [D_1(\Delta t_n)]k_{12}\Delta t$$

Where D_1 is the initial dimerization state and hence receives all new dimerization events at each time interval. D_2 is the relaxed dimer state and is acquired through D_1 at the relaxation rate k_{12}. A second, backward rate constant k_{21} could have also been incorporated, but was found to be an unnecessary parameter for simulating the observed FRET signal.

The above equations are sufficient for instantaneous transitions between D_1 and D_2. However, for a finite relaxation time, an additional set of transition states $\mathbf{D_{12}}$ is acquired with a total transition time of $\tau_{12} = m\Delta t$. Here, m is an integer representing the number of concentration elements of the vector [$\mathbf{D_{12}}$]. The final time-dependent equations can be written:

$$[D_1(\Delta t_{n+1})] = [D_1(\Delta t_n)]\left(1 - k_{off}\Delta t - k_{12}\Delta t\right) + [M(\Delta t_n)]^2 k_{on}\Delta t$$

$$[D_{12}(i, \Delta t_{n+1})] = \begin{cases} [D_1(\Delta t_n)]k_{12}\Delta t, & i = 1 \\ [D_{12}(i-1, \Delta t_n)](1 - k_{off}\Delta t), & 2 \le i \le m \end{cases}$$

$$[D_2(\Delta t_{n+1})] = [D_2(\Delta t_n)]\left(1 - k_{off}\Delta t\right) + [D_{12}(m, \Delta t_n)]k_{12}\Delta t$$

Where i indicates the i^{th} element of the set of states $\mathbf{D_{12}}$ and the total time a subpopulation of dimers has spent in transition is $\tau = i\Delta t$.

FRET calculations

FRET can be determined by applying the Förster equation:

$$E = \frac{1}{1 + \left(\frac{r}{R_0}\right)^6}$$

Where E is the FRET efficiency, r is the distance between the donor and the acceptor, and R_0 is the Förster distance at which $E = \frac{1}{2}$. If the fraction of donor molecules is F, and acceptor molecules is (1-F), then the distribution of dimer pairs is given by the binomial distribution:

$$\binom{2}{k} F^k (1-F)^{2-k} \quad for\ k = 0,1,2$$

For any sub-population of dimers, the donor fluorescence (S_{DONOR}) and the FRET signal (S_{FRET}) are proportional to the probability of getting a FRET pair:

$$P_{AD} = 2F(1-F)$$

$$S_{FRET} \propto P_{AD} E(r)[D(r)]$$

$$S_{DONOR} \propto P_{AD}\big(1 - E(r)\big)[D(r)]$$

By assigning a value for r for each state D_1, D_2, and a set of r-values for the vector of states $\mathbf{D_{12}}$, we can determine the FRET efficiency at each state (E_1, E_2, $\mathbf{E_{12}}$). The total signal is given by:

$$S_{FRET}(\Delta t_n) = 2F(1-F)\left\{E_1[D_1(\Delta t_n)] + E_2[D_2(\Delta t_n)] + \sum_{i=1}^{m} E_{12}(i)[D_{12}(i, \Delta t_n)]\right\}$$

$$S_{DONOR}(\Delta t_n) = F[M(\Delta t_n)] + 2F^2[D(\Delta t_n)]$$

$$+ 2F(1-F)\left\{(1-E_1)[D_1(\Delta t_n)] + (1-E_2)[D_2(\Delta t_n)]\right.$$

$$\left. + \sum_{i=1}^{m}\big(1 - E_{12}(i)\big)[D_{12}(i, \Delta t_n)]\right\}$$

Simulation parameters

For the GTP-binding dimer simulations, the Förster distance R_0 we used was the calculated value of 47 Å. The value of r for D_1 and D_2 were 30 Å and 50 Å as determined from structural data. We estimate that the equilibrium dissociation constant for dimerization to be better than 1μM, therefore we assumed a dissociation constant $K_D = \frac{k_{off}}{k_{on}}$ of 500 nM. Assuming a k_{on} of about 0.32 $\mu M^{-1}s^{-1}$ k_{off} was calculated to be 0.16 s^{-1}. The relaxation rate k_{12} was taken to be 0.50 s^{-1} with a transition time τ_{12} of 0.10 s. The time interval Δt was 0.01 s, which matches the time resolution of the relevant instrumentation. Finally the transition states $\mathbf{D_{12}}$ were calculated by assuming a uniform transition speed:

$$\frac{\Delta r}{\Delta \tau} = \frac{D_2 - D_1}{\tau_{12}}$$

$$D_{12}(r_i) = \frac{D_2 - D_1}{\tau_{12}} i\Delta t \quad for\ i = 1 \dots m$$

For the GppNHp-binding dimer simulations, only the kinetic parameters are assumed to change. Since this system cannot undergo hydrolysis, it is assumed that the relaxation rate constant k_{12} is zero and hence does not undergo any transition (i.e. $\mathbf{D_{12}}$ and D_2 are always zero). We also observed a significantly longer time scale for equilibration of over an order of magnitude. Assuming the equilibrium dissociation constant for dimerization is unchanged, we chose to use a lower k_{on} of 0.006 $\mu M^{-1}s^{-1}$ and thus a calculated k_{off} of 0.003 s^{-1}.